ROYAUME DU MAROC
Université Mohammed V - RABAT -
جامعة محمد الخامس – الرباط –
Faculté des sciences
كلية العلوم

CENTRE D'ÉTUDES DOCTORALES - SCIENCES ET ECHNOLOGIES

Thesis to obtain the degree of **PhD** of science

Spéciality: Particle physics

Defended by: **Zainab SOUMAIMI**

Search for new scalar decays to Beyond Standard Model Dark-Z Bosons in Four-Lepton Final States with the ATLAS detector at the LHC

Supervisors:
Prof. Farida FASSI
Dr. Kétévi Adikle ASSAMAGAN

Thesis committee:

Prof. Mohamed CHABAB	Faculté des sciences Semlalia, Marrakech	Président
Prof. Hamid EZ-ZAHRAOUY	Faculté des sciences, Rabat	Rapporteur
Prof. Abdesslam ARHRIB	Université Abdelmalek Essaadi, Faculté des Sciences et Techniques, Tanger	Rapporteur
Prof. Yassine Hassouni	Faculté des sciences, Rabat	Rapporteur
Dr. Kétévi Adikle ASSAMAGAN	Brookhaven National Laboratory, USA	Co-director
Prof. Farida FASSI	Faculté des sciences, Rabat	Director

2023/2024

Faculté des Sciences, avenue Ibn Battouta, BP. 1014 RP, Rabat–Maroc
+00212(05) 37 77 18 76, Fax: +00212(05) 37 77 42 61; http://www. fsr.um5.ac.ma

Dedication

To my family, who have been my unwavering source of love, support, and inspiration throughout this journey. Your belief in me has fueled my determination every step of the way.

Acknowledgements

Primarily, I extend my genuine appreciation to **Hamid EZ-ZAHRAOUY**, an esteemed university education Professor at the Faculty of Sciences in Rabat and the director of the "Laboratory of Condensed Matter and Interdisciplinary Sciences: Unit of Research Labeled CNSRT." His steadfast accessibility, both through his office and mobile communication, proved invaluable whenever I encountered challenges or sought guidance.

It is a great privilege and honour for me to have worked under the supervision of **Farida FASSI**, a university education Professor, and I am extremely grateful to my co-supervisor, **Kétévi A. ASSAMAGAN**, a physicist at the Brookhaven National Laboratory, for their unwavering commitment to academic excellence, insightful guidance, and continuous encouragement throughout the intricate stages of this doctoral endeavour. Their intellectual rigour and unwavering commitment to scholarly pursuit have been the bedrock upon which this thesis is constructed.

I wish to express my profound gratitude to **Mohamed CHABAB**, a distinguished university education professor at the Faculty of Sciences Semlalia Marrakesh, who graciously assumed the role of the jury president. His insightful comments and engaging discussions pertaining to this thesis work are sincerely appreciated.

I extend my heartfelt appreciation to **Hamid EZ-ZAHRAOUY**, a distinguished university education professor at the Faculty of Sciences in Rabat, who served as the reporter and examiner for my thesis work. I am truly thankful for his meticulous comments and engaging discussions that have enriched the depth of my research.

Moreover, I wish to convey special gratitude to **Abdeslam ARHRIB**, a university education professor at the Faculty of Sciences and Technology in Tangier, who assumed the roles of both reporter and examiner for my thesis. I am deeply appreciative of the valuable insights he provided through his constructive comments.

Furthermore, I express my profound gratitude to **Yassine Hassouni**, an esteemed academician affiliated with the Faculty of Sciences in Rabat, who served as the examiner and reporter for my thesis. His extensive expertise and discerning evaluation significantly contributed to the scholarly rigor of my work.

I owe a debt of gratitude to my family for their support and understanding during the demanding phases of doctoral studies. Their steadfast encouragement has been a source of inspiration, providing the necessary fortitude to navigate the challenges inherent in the pursuit of academic excellence.

Last but not least, my heartfelt thanks to my colleagues and the research team within the ATLAS collaboration for their camaraderie, intellectual exchange, and collaborative spirit. The collective effort of the research community has created an intellectually vibrant and stimulating atmosphere.

Résumé

Cette thèse examine la désintégration des processus impliquant une particule scalaire supplémentaire, S, conduisant à la production de quatre leptons via deux bosons sombres Z_d au-delà du Modèle Standard (Z_d: $S \rightarrow Z_d Z_d \rightarrow 4\ell$ (où $l = e, \mu$). Les données du LHC (2015-2018) sont utilisées, avec une luminosité de 139 fb^{-1} à une énergie de centre de masse de 13 TeV. Dans le contexte des extensions au Modèle Standard pour la matière noire, le Modèle Abélien caché de Higgs (HAHM) est exploré, introduisant un secteur sombre et une particule scalaire S. Des limites sont établies sur $\sigma \times \mathcal{B}r(S \rightarrow Z_d Z_d \rightarrow 4\ell)$ pour différentes masses de S, révélant une déviation significative par rapport au Modèle Standard, en particulier à (m_S , m_{Z_d}) = (110 GeV, 30 GeV). La deuxième partie se concentre sur la Performance Thermique des modules à bandes ATLAS ITk à BNL. Les résultats du cyclage thermique confirment la résilience de la lamelle ITk, capable de résister à des températures de 23°C à -45°C sans dommages importants ni dégradation des performances.

Mots-clefs: Modèle Standard, matière noire, Au-delà du Modèle Standard, section efficace, ATLAS, détecteur ITk.

Abstract

This thesis investigates the decay processes involving an additional scalar particle, S, leading to the production of four leptons through two dark vector bosons beyond the Standard Model (Z_d: $S \rightarrow Z_d Z_d \rightarrow 4\ell$ (où $l = e, \mu$). The analysis uses data from the ATLAS detector at the LHC (2015-2018) with an integrated luminosity of 139 fb^{-1} at a center-of-mass energy of 13 TeV and explores extensions to the Standard Model, particularly the Hidden Abelian Higgs Model. Limits are set on the cross-section and branching ratio, $\sigma \times \mathcal{B}r(S \rightarrow Z_d Z_d \rightarrow 4\ell)$ for different masses of S, revealing a significant deviation from the Standard Model, notably at $(m_S\ , m_{Z_d}) =$ (110 GeV, 30 GeV). The second part focuses on the Thermal Performance of ATLAS ITk strip modules at BNL, confirming the resilience of the module across a temperature range from 23°C to -45°C.

Keywords: Standard Model, Dark matter, Beyond Standard Model, cross section, ATLAS, ITk detector.

Résumé détaillé

Dans le cadre théorique de la physique des particules, le Modèle Standard (MS) sert de pierre angulaire, décrivant avec succès les interactions fondamentales entre les particules subatomiques et fournissant une compréhension approfondie de la matière et des forces qui la gouvernent. Cependant, malgré ses triomphes, le SM présente des lacunes notables, dont l'une des plus intrigantes est sa capacité limitée à expliquer la nature de la matière noire (DM).
La matière noire constitue environ 27% de l'univers, mais sa composition demeure énigmatique. Les observations astrophysiques, allant des mouvements galactiques aux fluctuations du rayonnement cosmique, confirment l'existence de la matière noire. Cependant, sa nature demeure insaisissable dans le cadre du Modèle Standard, laissant place à des spéculations et à des extensions théoriques.
Diverses propositions d'extensions du MS ont émergé pour incorporer la matière noire dans le tissu même de la physique des particules. Ces extensions explorent un domaine connu sous le nom de "secteur caché", comprenant des particules supplémentaires agissant comme des médiateurs pour les interactions de la matière noire.
Le Grand Collisionneur de Hadrons (LHC) s'est imposé comme un outil essentiel dans la quête de nouvelles particules et interactions au-delà du MS. Les découvertes, notamment celle du boson de Higgs en 2012, ont élargi notre compréhension du mécanisme de Brisure de Symétrie Électrofaible, mais ont également suscité un intérêt renouvelé pour la recherche de signes de particules liées à la matière noire.

Cette thèse se consacre à l'investigation des processus de désintégration impliquant une particule scalaire supplémentaire, désignée par S, aboutissant à la production de quatre leptons dans l'état final par le biais de deux bosons vecteurs sombres au-delà du Modèle Standard, nommément Z_d: $S \to Z_d Z_d \to 4\ell$ (où $l = e, \mu$). L'analyse repose sur des données de collisions proton-proton acquises par le détecteur ATLAS au Grand Collisionneur de Hadrons (LHC) sur la période de 2015 à 2018. Ces données, caractérisées par une luminosité intégrée de 139 fb^{-1} à une énergie de centre de masse de 13 TeV, constituent la base de cette étude.

Dans la quête de comprendre les phénomènes au-delà du Modèle Standard (MS), plusieurs propositions d'extensions ont émergé, suggérant l'existence d'un secteur caché abritant des particules agissant en tant que médiateurs des interactions de la matière noire. Un cadre théorique particulièrement captivant pour étendre le Modèle Standard à la matière noire est le Modèle Abélien Caché de Higgs (Hidden Abelian Higgs Model - HAHM). Ce modèle introduit un secteur sombre composé de particules et de champs, dont l'un possède une symétrie de jauge sombre $U(1)_d$. Cette symétrie interagit cinétiquement avec le champ de jauge d'hypercharge $U(1)_Y$ du Modèle Standard, caractérisé par une force de couplage ϵ. Cette interaction engendre l'émergence d'une particule scalaire supplémentaire, S, accompagnée d'un nouveau boson de jauge Z_d, fréquemment désigné comme 'photon sombre'. La particule scalaire S subit un mélange avec le boson de Higgs, la force de ce mélange étant indiquée par le paramètre de couplage κ. Des limites sont établies sur le produit de la section efficace et du rapport de branchement, représenté par $\sigma \times \mathcal{B}r(S \to Z_d Z_d \to 4\ell)$, où la particule scalaire S a une masse comprise entre 30 et 115 GeV (Région de signal 1) ou entre 130 et 800 GeV (Région de Signal 2). Les résultats de cette enquête mettent en lumière une déviation par rapport aux attentes du Modèle Standard. Cette surabondance, en concordance avec le processus $pp \to 4\ell + X$, est particulièrement prononcée autour de (m_S , m_{Z_d})=(110 GeV,30 GeV), présentant une signification globale (locale) de 3.4σ $(4, 4\sigma)$. Pour une compréhension approfondie de l'origine de cette surabondance, des données supplémentaires se révèlent impératives.

La seconde partie de la thèse se concentre sur l'étude de la Performance Thermique des modules à bandes ATLAS ITk réalisée à BNL. Les résultats de l'expérience de cyclage thermique attestent sans équivoque de la robustesse de la lamelle ITk examinée. Cette étude démontre la capacité du composant à résister à une plage de températures allant de 23°C à -45°C sans subir de dommages significatifs ni de dégradation des performances.

List of publications

- ATLAS Collaboration. "Search for short- and long-lived axion-like particles in $H \to aa \to 4\gamma$ decays with the ATLAS experiment at the LHC". arXiv: 2312.03306 [hep-ex] (Dec. 2023) [1].
- ATLAS Collaboration. "Measurement of ZZ production cross-sections in the four-lepton final state in pp collisions at $\sqrt{s} = 13.6$ TeV with the ATLAS experiment". arXiv: 2311.09715 [hep-ex] (Nov. 2023) [2].
- ATLAS Collaboration. "Measurement of the Higgs boson mass in the $H \to ZZ* \to 4\ell$ decay channel using 139 fb^{-1} of $\sqrt{s}$=13 TeV pp collisions recorded by the ATLAS detector at the LHC". Physics Letters B 843, 137880. issn: 0370-2693. (Aug. 2023) [3].
- ATLAS Collaboration. "Combination and summary of ATLAS dark matter searches interpreted in a 2HDM with a pseudo-scalar mediator using 139 fb^{-1} of $\sqrt{s} = 13$ TeV pp collision data". arXiv: 2306.00641 [hep-ex] (June 2023) [4].
- ATLAS Collaboration. "Search for Higgs bosons decaying into new spin-0 or spin-1 particles in four-lepton final states with the ATLAS detector with 139 fb^{-1} of pp collision data at $\sqrt{s}$= 13 TeV". Journal of High Energy Physics 2022. 41. issn: 1029-8479 (Mar. 2022) [5].
- Soumaimi, Zainab and Boye, Diallo and Fassi, Farida and Assamagan, Ketevi and Connell, Simon and Weber, Christian. "Search for Higgs boson Decays to Beyond-the-Standard-Model Light Bosons in Four-Lepton Final States with the ATLAS Detector at the LHC". (Apr. 2021) [6].
- ATLAS Collaboration. "Search for new phenomena in events with an energetic jet and missing transverse momentum in pp collisions at $\sqrt{s} = 13$ TeV with the ATLAS detector". Physical Review D 103. issn: 2470-0029 (June 2021) [7].

- Scopus author ID: 57222151221
- ORCID: 0000-0002-8120-478X
- INSPIRE ID: 1885123

List of contributions

Throughout my thesis, I actively participated in the following tasks:

- ATLAS E^{T}_{miss} Subgroup Task: Headed the development of a specialized tool enhancing MET source identification, improving efficiency and accuracy in analyses for ATLAS collaboration research.

  → Bug Fix in the METPerfAnalysis Package: Implemented a solution to streamline access to truth particles when utilizing truth maps.

- Analysis of the search for a new scalar particle decaying into Beyond Standard Model Z_d bosons: This study delves into the exploration of the decay processes of a novel scalar particle, with a focus on its interactions leading to the emergence of Beyond Standard Model Z_d bosons.
- Extrapolating the Branching Ratio for $Z_d \rightarrow 2\ell$: This analysis extends beyond the 60 GeV mass threshold, exploring new scalar decays with Beyond Standard Model Z_d bosons. The extrapolation is conducted using the Mathematica computational platform, ensuring enhanced precision and efficiency.
- Establishing limits on the branching ratio for the $S \rightarrow Z_d Z_d$ process in two signal regions, this study investigates new scalar decays with Beyond Standard Model Z_d bosons, utilizing the StandardHypoTestInv workspace.
- Development of Slow Control System for ITk Strip Stave Thermal Cycling:

  → Created a Python script to gather data from a USB temperature logger and two humidity sensors, capturing eight temperature measurements and two humidity values. The instrumentation interfaces with two parallel boxes designed for two ITk strip staves.

  → Explored the effects of thermal cycling on the operational efficiency of the Inner Tracker stave within a coldbox. Implemented a USB logger for comprehensive measurements of four temperature points and two humidity sensors.

List of abbreviations

Name	**Symbol**
Standard Model	SM
Large Hadron Collider	LHC
High Luminosity operation of the LHC	HL-LHC
Quantum Field Theory	QFT
Quantum Electrodynamics	QED
Electroweak	EW
Electroweak Symmetry Breaking	EWSB
Brookhaven National Laboratory	BNL
Grand Unified Theory	GUT
Dark matter	DM
SuperSymmetry	SUSY
Weekly Interacting Massive Particles	WIMPs
Beyond the Standard Model	BSM
Hidden Abelian Higgs Model	HAHM
Two Higgs Doublet Model+scalar	2HDM+s
High Mass	HM
Low Mass	LM
Additional Scalar	AS
European Organisation for Nuclear Research	CERN
A Toroidal LHC Apparatus	ATLAS
Inner Detector	ID
Electromagnetic Calorimeter	ECal
Liquid Argon Calorimeter	LAr
Hadronic Calorimeter	HCal
Muon Spectrometer	MS
Inner Tracker	ITk
Short Strip	SS
Long Strip	LS
General Purpose Input/Output	GPIO
Parton Distribution Functions	PDFs
Next-to-Leading Order	NLO
Next-to-Next-to-Leading Order	NNLO
Missing Transverse Energy	MET(E^T_{miss})
Track Soft Term	TST
Signal Region 1	SR1
Signal Region 2	SR2

Contents

Figures

Tables

Chapter 1

Introduction

Thousands of physics theories and discoveries have provided an interesting and deep comprehension of the fundamental structure of matter. The Standard Model (SM), developed in the early 1970's, is the best understanding that we have to date of this structure made of the fundamental particles and the fundamental interactions governing the relations between them. Its experimental predictions, confirmed by experimental observations performed all these years, have proved the existence of new particles such as the W, Z and *Higgs* bosons that have been precisely tested a wide variety of phenomena. The discovery of the Higgs boson by the ATLAS and CMS experiments at the Large Hadron Collider (LHC) in 2012 was a breakthrough in physics research, and precise studies and measurements have been performed on the Higgs boson's mass, couplings and cross section with collected data-sets with ATLAS and CMS detectors.

However, the Standard Model remains a deficient theory for its inability to explain the presence of *dark matter* in our universe, the strong CP problem, neutrino oscillations, matter-antimatter asymmetry, etc. All these unexplained phenomena are a strong motivation to adopt theories beyond the SM and consider various *extensions*.

One extension of the Standard model is where the SM Higgs boson interacts with a dark sector, also known as *Hidden* sector, where it decays to a couple of dark sector particles each called Z_d. This model could have rich and interesting phenomenology like the SM.

The present thesis is conducted for the search for a new dark scalar; S; decaying to four SM leptons in the final state through two dark sector mediators; $S \rightarrow Z_d Z_d \rightarrow 4l$; with data collected by the ATLAS detector at LHC between 2015 and 2018 (full Run2 data-set) at a centre-of-mass energy of $\sqrt{s} = 13$ TeV and where the amount of data corresponds to an integrated luminosity of 139 fb^{-1}.

This search is an extension of a previous analysis that have been initiated in the Run1 period [8] of LHC between 2015-2016 using 36 fb^{-1} data at 13 TeV and following the search where using 139 fb^{-1} data at 13 TeV [9] considering the decay of the SM Higgs boson to two Z_d giving 4l at the final state; $H \to Z_d Z_d \to 4l$.

The current thesis is following the below structure:
In Chapter 2, an overview of the SM is given, its particles and interactions, Higgs potential and electroweak symmetry breaking, its successes and limitations are elaborated, as well as a review on the Beyond SM models motivating this study. The Large Hadron Collider and the ATLAS detector are described in Chapter 3, followed by Chapter 5 presenting the description of physics objects reconstruction and identification. Section 5.2.6 describes the study that I have been involved in, in my Qualification Task, regarding the comparison between the reconstructed and the truth missing energy, E_T^{miss}, in $Z \to \mu\mu$ events. Chapter 6 focuses on the analysis study where the results performed with the ATLAS detector using p-p collision data, are presented. And finally, an interpretation and discussion of the results are in Chapter 7.
Chapter 4 presents my contribution in developing an algorithm for measuring the temperature and the humidity to control the thermal cycle of the ITk Strip staves to cope with the radiation damages during High Luminosity operation of the LHC (HL-LHC).

Chapter 2

Theoretical context

2.1 Introduction

In the late 1970s, the Standard Model started to be the basic theory explaining matter in elementary particle physics and the accurate model describing the composition of our universe. It is based on two types of elementary particles: the fundamental spin$\frac{1}{2}$ particles called "Fermions" and the quanta of fields, with spin 1, named "Bosons" which are exchanged during fermions interactions. It is an ontological basis for understanding the matter in all its forms. There are no well-established results in particle physics that haven't been in good agreement with the theory.

In this chapter, an overview is provided of the Standard Model's main axes.

2.2 The Standard Model (SM) of particles physics

In our universe, four fundamental interactions describe the behaviour and the phenomenology of matter and the Standard Model can only, at the microscopic scale, explain three of them: electromagnetic, weak, and strong forces, since the gravitational interaction has only an effective influence at the macroscopic scale. Molecular physics, atomic, nuclear, and sub-nuclear physics are all interpreted under those three interactions; such interactions are described as an exchange of bosons between fermions within a local relativistic *Quantum Field Theory (QFT)* based on the principal gauge invariance of $SU(3)_C \otimes SU(2)_L \otimes U(1)_Y$.

2.2.1 The Fundamental particles and interactions of SM

There are two kinds of elementary particles: matter particles, which, are combined to produce the world around us and are called fermions, and the force particles, named bosons, are the ones carrying the elementary interactions. Due to the spin-statistics theorem, the spin of those particles indicates whether they should obey the Fermi-Dirac or Bose-Einstein statistics, with half-integer spins following the former and integer spins following the latter as shown in Figure 2.1.

The two types of fermions along with the force carriers; bosons; are listed below:

- **Leptons**
  Leptons are divided into three generations of increasing mass, each formed by a negatively charged lepton and its associated neutral partner: $\{e, \nu_e\}$, $\{\mu, \nu_\mu\}$ and $\{\tau, \nu_\tau\}$. A quantum number is associated with each lepton named *Leptonic* charge (L) representing the difference between the number of leptons and the number of anti-leptons ($\{e^+, \overline{\nu}_e\}$, $\{\mu^+, \overline{\nu}_\mu\}$, $\{\tau^+, \overline{\nu}_\tau\}$) in an elementary particle reaction. The muon is 200 heavier than the electron while the tau lepton is 3477 heavier than the electron.

- **Quarks**
  As shown in Figure 2.2a, the quarks, same as the leptons, are divided into three generations ({up, down}, {charm, strange} and {top, bottom}) and gathered in two categories: up-type and down-type quarks. The former type quarks possess a $+\frac{2}{3}e$ charge and the latter type quarks have $-\frac{1}{3}e$ charge (Figure 2.2b).

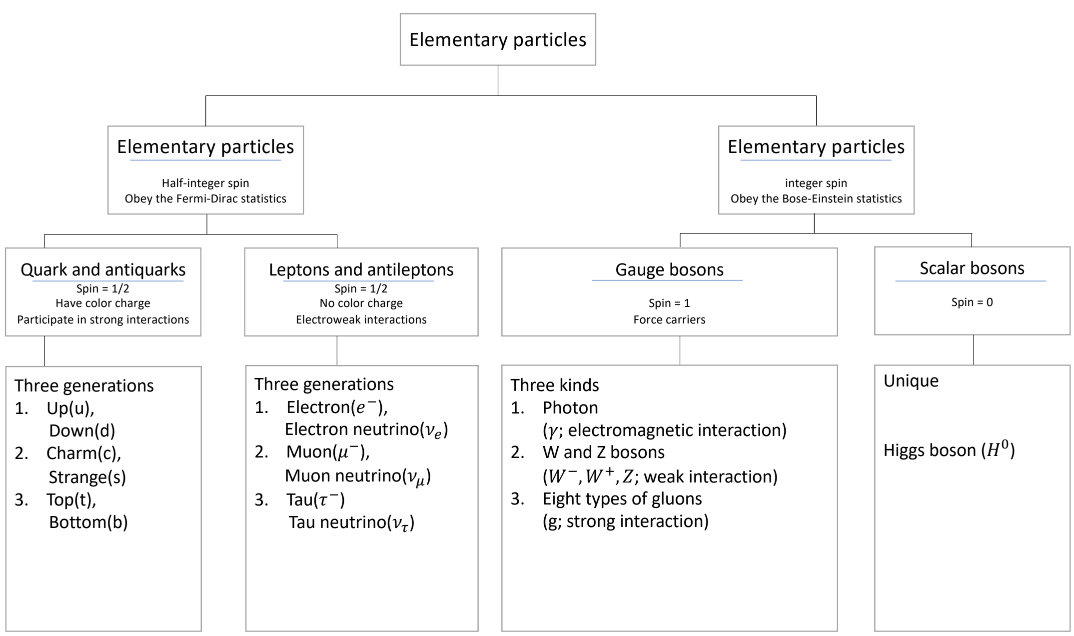

Figure 2.1: Standard Model elementary particles.

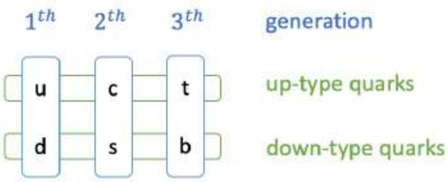

(a)

	Quarks	Leptons
1^{th} generation	$u^{+\frac{2}{3}}_{2.16MeV}$ [1] $d^{-\frac{1}{3}}_{4.67MeV}$	$e^{-}_{0.511MeV}$ [2] $\nu^{0}_{e\,0}$
2^{th} generation	$c^{+\frac{2}{3}}_{1.27GeV}$ $s^{-\frac{1}{3}}_{93MeV}$	$\mu^{-}_{105.7MeV}$ $\nu^{0}_{\mu 0}$
3^{th} generation	$t^{+\frac{2}{3}}_{172.4GeV}$ $b^{-\frac{1}{3}}_{4.18GeV}$	$\tau^{-}_{1.8GeV}$ $\nu^{0}_{\tau 0}$

(b)

Figure 2.2: Fermions families along with their electric charges and masses.

- **Bosons**

  The bosons are either the mediators of the elementary interactions between the fermions or give rise to the phenomenon of mass.

  The Four *vector* bosons (spin=1) are:

  – The photon (γ) is the electromagnetic force mediator with no mass and charge.

  – The two weak interaction carriers are the neutral boson Z^0 and the charged boson $W^{\pm}$, their masses are measured to be 80.3 GeV and 91.18 GeV respectively and they were discovered at CERN in 1983 by the UA1 and UA2 (Underground Area 1,2) experiments.

  – The Gluons are charge-less and mass-less bosons responsible for mediating the strong force between quarks; moreover, they bind quarks together to form hadrons.

  and the *scalar* boson (spin=0) is:

  – The Higgs boson is the elementary particle produced by the quantum excitation of the Higgs field and the responsible for giving some particles masses.

The interactions mentioned before, are treated as gauge symmetries where the bosons are the generators of the associated gauge groups.

The gauge theories are more convenient to explain the dynamics of the elementary particles (Lagrangian) which are invariant under local transformations.

The three fundamental nuclear interactions are as follows:

- **Electromagnetic force**

  The electromagnetic interaction includes the force acting between electrically charged particles. These dynamics are described by Quantum Electrodynamics (QED) and

[1] $Fermion^{charge}_{mass}$

[2] The fermions mass is expressed in terms of energy where $E = mc^2$ and c is the light velocity.

presented by a Lagrangian density.

The Lagrangian of the electromagnetic interaction is formulated by:

$$\mathcal{L}_{QED} = \overline{\psi} i\gamma^{\mu}\partial_{\mu}\psi - m\psi\overline{\psi} \tag{2.1}$$

where $\psi(x,t)$ is the fermion field, m is the particle mass, γ^{μ} are the Dirac matrices, and μ is the Einstein convention that represents the components of space and time; $\overrightarrow{x}$ and t.

The gauge group of this interaction is $U(1)$ and to ensure that the Lagrangian is invariant under this group, the local phase transformation of the fermion field should verify:

$$\psi \rightarrow e^{i\alpha(x)}\psi. \tag{2.2}$$

Taking also into consideration the kinetic propagation of the field described by the field tensor $F^{\mu\nu} = -F^{\nu\mu} = \partial^{\mu}A^{\nu} - \partial^{\nu}A^{\mu}$, the Lagrangian density becomes:

$$\begin{aligned}\mathcal{L} &= \overline{\psi} i\gamma^{\mu}\partial_{\mu}\psi - m\psi\overline{\psi} + q\overline{\psi}\gamma^{\mu}A_{\mu}\psi - \frac{1}{4}F^{\mu\nu}F_{\mu\nu} \\ \mathcal{L} &= \overline{\psi}(i\gamma^{\mu}(\partial_{\mu} - iqA_{\mu}) - m)\psi \\ \mathcal{L} &= \overline{\psi}(i\gamma^{\mu}(\partial_{\mu} + ieA_{\mu}) - m)\psi\end{aligned} \tag{2.3}$$

where the newly introduced field A_{μ} represents the photon and the $q = -e$ is the electromagnetic interaction charge. It should be noted that in the $U(1)$ abelian gauge group, the photons are not self-interacting and the electromagnetic tensor does not include the term of the photon's self-interactions as well.

- **Electroweak force**
  The electroweak interaction is a combination of the electromagnetic and the weak interactions that is described by the unified gauge symmetry $SU(2)_L \times U(1)_Y$. It was first proposed by the Weinberg-Salam-Glashow model to understand how the two interactions behave in a unified way. The $SU(2)_L$ part corresponds to a weak isospin triplet of the gauge bosons $W^{\pm}_{\mu}$ and W^3_{μ}, where $W^{\pm}_{\mu} = \frac{1}{\sqrt{2}}(W^1_{\mu} \mp (W^2_{\mu})$, and the $U(1)_Y$ part corresponds to a singlet; B_{μ}.
  The two neutral gauge bosons; B_{μ} and W^3_{μ}; form the quantum-mechanical mixture which produces the two physically observable gauge bosons; A_{μ} and Z_{μ}; as shown in Equation 2.4:

$$\begin{aligned}A_{\mu} &= B_{\mu}cos(\theta_W) + W^3_{\mu}sin(\theta_W) \\ Z_{\mu} &= W^3_{\mu}cos(\theta_W) - B_{\mu}sin(\theta_W)\end{aligned} \tag{2.4}$$

where θ_W is the weak mixing angle, the A_{μ} field corresponds to the photon, and the Z_{μ} field to the Z boson.

Fermions	Field	Weak Isospin T_3	Hypercharge Y[3]
Quarks	$\mathcal{Q}_L = \begin{pmatrix} u_L \\ d_L \end{pmatrix}$	$\frac{1}{2}$ -$\frac{1}{2}$	$\frac{1}{6}$ $\frac{1}{6}$
	u_R	0	$\frac{2}{3}$
	d_R	0	-$\frac{1}{3}$
Leptons	$\mathcal{L}_L = \begin{pmatrix} \nu_L \\ e_L \end{pmatrix}$	$\frac{1}{2}$ -$\frac{1}{2}$	$\frac{1}{6}$ $\frac{1}{6}$
	e_R	0	-1

Table 2.1: The weak isospin and the hypercharge of the Standard Model fermions with their doublet paring and singlets.

The Lagrangian density of the EW interaction is:

$$\mathcal{L}_{EW} = \overline{\psi} i\gamma^\mu \partial_\mu \psi - eY\overline{\psi}\gamma^\mu B_\mu \psi - g_W \overline{\psi}\gamma^\mu \mathbf{T}.\mathbf{W}_\mu \psi - \frac{1}{4}B^{\mu\nu}B_{\mu\nu} - \frac{1}{4}W^{i\mu\nu}W^i_{\mu\nu}, \quad (2.5)$$

where g_W is the weak coupling to the fermionic fields and defined as:

$$W^i_{\mu\nu} = \partial_\mu W^i_\nu - \partial_\nu W^i_\mu - g_W \epsilon_{ijk} W^j_\mu W^k_\nu. \quad (2.6)$$

In the weak interactions, fermions are categorised to *left-handed* and *right-handed* chirality types, the left-handed fermions and right-handed anti-fermions form doublets under $SU(2)_L$ and the right-handed fermions and the left-handed anti-fermions form singlets as shown in Table 2.1.

- **Strong force**
  The strong interaction is described by the Quantum ChromoDynamic theory under the $SU(3)_C$ gauge field theory. The $SU(3)_C$ Lie group has eight generators that correspond to the eight mediators of the strong force; gluons, and are denoted as G^a where a takes the values $a = 1, 2, 3, ..., 8$. The field strength tensor of the gluon field is:

$$G^a_{\mu\nu} = \partial_\mu G^a_\nu - \partial_\nu G^a_\mu - g_s f_{abc} G^b_\mu G^c_\nu, \quad (2.7)$$

where g_s is the strong coupling constant responsible for precising the strength of the quarks-gluons interactions (colored particles) and f_{abc} is the structure constant of the $SU(3)$ group.
The Lagrangian of the QCD is:

$$\mathcal{L}_{QCD} = -\frac{1}{4}G^a_{\mu\nu}G^{\mu\nu}_a + i\overline{q}^j_r \gamma^\mu (D_\mu)_{jk} q^k_r, \quad (2.8)$$

considering j and k running over the three colors and where D_μ si the corresponding gauge covariant derivative:

$$D_\mu = \partial_\mu + ig_s T_a G^a_\mu, \quad (2.9)$$

where $T_a \equiv \lambda_a/2$, with λ_a are the Gell-Mann matrices.

[3]The weak isospin and the hypercharge are both obtained from the charge by: $q = T_3 + \frac{Y}{2}$.

2.2.2 Electroweak symmetry breaking

In the electroweak Lagrangian $\mathcal{L}_{EW}$ (Equation 2.5), the W/Z bosons have no mass term appearing and the fermions mass term in $\mathcal{L}_{QED}$ (Equation 2.1) is also absent, while in the observations they have masses. Since a mass term for the W and B gauge bosons in Equation 2.5 would break the $SU(2)_L \times U(1)_Y$ gauge symmetry, an introduction of an additional mechanism is required to explain the origin of W/Z masses. This is handled through the Electroweak Symmetry Breaking (EWSB) process and the Higgs boson mechanism

This mechanism consists of a spontaneous symmetry breaking by introducing a complex scalar $SU(2)_L$ doublet; ϕ:

$$\boldsymbol{\phi} = \frac{1}{\sqrt{2}} \begin{pmatrix} \phi_+ \\ \phi_0 \end{pmatrix} \tag{2.10}$$

Then, the Higgs Lagrangian is:

$$\mathcal{L}_{Higgs} = (D^\mu \phi)^\dagger (D_\mu \phi) - V(\phi), \tag{2.11}$$

and:

$$D_\mu = (\partial_\mu + igT^i W^i_\mu + \frac{i}{2} g' B_\mu), \tag{2.12}$$

$$V(\phi) = \frac{1}{2}\mu^2 \phi^+ \phi + \frac{1}{4}\lambda(\phi^+\phi)^2, \tag{2.13}$$

are the covariant derivative and the Higgs potential. As shown in Figure 5.4, the param-

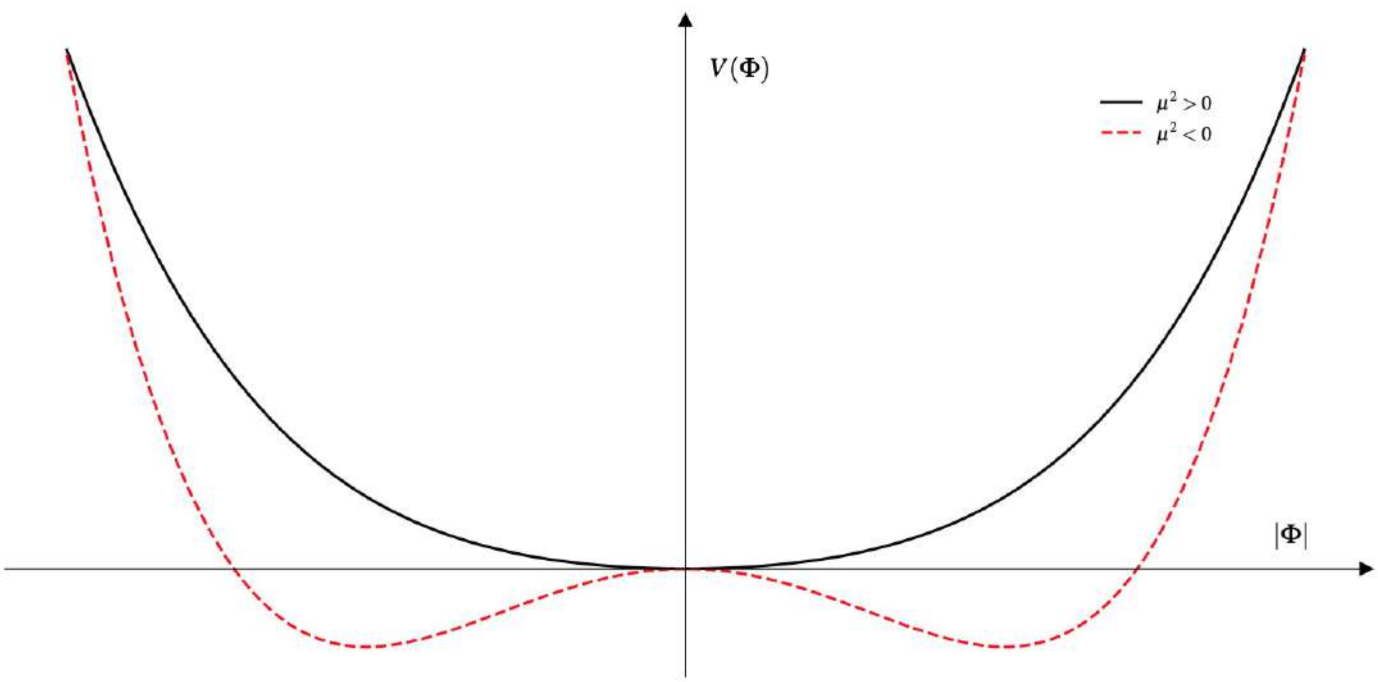

Figure 2.3: Shape of the scalar potential for $\mu^2 < 0$ (red dashed line) and $\mu^2 > 0$ (black line) [10].

eter μ^2 has two possibilities:

1. $\mu^2 > 0$, $\lambda > 0$: The potential has only the trivial minimum $\phi = 0$.
2. $\mu^2 < 0$, $\lambda > 0$: The potential has an infinite set of minima v called the vacuum expectation value(vev):

$$\phi_0 =< \phi^+\phi >= \frac{v^2}{2} = -\frac{\mu^2}{2\lambda} \tag{2.14}$$

In unitary gauge, the scalar doublet can be written in terms of the physical scalar Higgs field; h:

$$\boldsymbol{\phi} = \frac{1}{\sqrt{2}}\begin{pmatrix} 0 \\ v+h \end{pmatrix} \tag{2.15}$$

The scalar potential becomes:

$$V(\phi) = -\frac{\lambda v^4}{4} + \lambda v^2 h^2 + \lambda v h^3 + \frac{\lambda}{4}h^4, \tag{2.16}$$

where the mass of the Higgs boson is $m_h = v\sqrt{2\lambda}$. By choosing a particular solution, the symmetry gets spontaneously broken which yields the masses through the Higgs mechanism:

$$M_W = \frac{1}{2}gv \tag{2.17}$$

$$M_Z = \frac{M_W}{cos\theta_W} \tag{2.18}$$

$$M_A = 0, \tag{2.19}$$

where: $e = gsin\theta_W$ and $e = g^{'}cos\theta_W$.

2.2.3 State-of-the-art Standard Model measurements at LHC

The Standard Model is a remarkably simple and very powerful theory that explains what's happening in nature around us in a mathematical way expressed by several complex equations to make precise predictions. But when getting more close to higher levels of energy that existed shortly after the Big Bang, these equations and predictions get shaky and deficient. Moreover, the fourth fundamental force; gravity; is not included nor explained in the SM.

Before mentioning the problems and the limitations facing the SM, its successes and achievements are referred to below.

- **Successes**

  → The biggest achievement fulfilled by the SM is the observation of the predicted Higgs boson in 2012 by both ATLAS and CMS experiments at LHC. Figure 2.4

illustrates the distribution of the 4 leptons invariant mass m_{4l} in $H \to ZZ^* \to 4l$ process where the bump at 125 GeV indicates the Higgs boson by both ATLAS (Figure 2.4a) and CMS (Figure 2.4b) detectors.

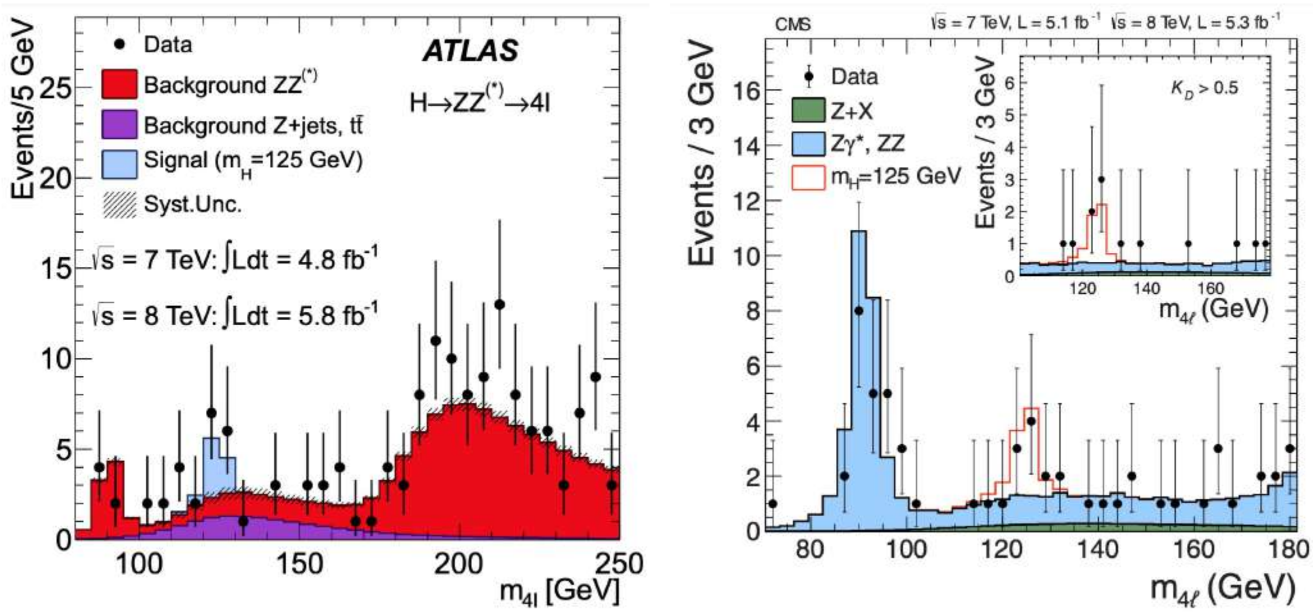

(a) [11] (b) [12]

Figure 2.4: The distribution of 4-leptons invariant mass with combined $\sqrt{s} = 7$ TeV and $\sqrt{s} = 8$ TeV data, in comparison to the background expectation in both ATLAS (a) and CMS (b) detectors. At $m_{4l} = 125$ GeV, the SM Higgs expectation is also displayed.

→ Sheldon Glashow, Steven Weinberg, and Abdus Salam announced, in 1968, the theory of electromagnetism and weak interaction unification where the prediction of the $W^{\pm}$ and Z bosons was introduced. In 1983, the observation of the three bosons was announced (January 1983, The W boson was discovered at the Super Proton Synchrotron, and after a few months in May 1983, the Z was found by the UA1 and UA2 experiments). Early measurements were performed on the W and Z bosons' properties [13, 14] and more recent publications show the accuracy of the Standard Model [15].

→ In 1974, a meson[4] called the J/ψ particle was discovered by both Burton Richter and Samuel Ting at SLAC (Stanford Linear Accelerator Center) and BNL (Brookhaven National Laboratory) respectively. It was discovered with a mass three times over that of the proton ($m_c = 3100$ MeV) and made up of a charm and an anti-charm quarks. After about 20 years, the top quark observation was reported by Fermilab's Tevatron in 1995 with a mass of $m_t = 176.3 \pm 18$ GeV then completing by that the third family of the quarks. The top quark mass is now considered to be $172.69 \pm 0.25 \pm 0.41$ GeV.
In 1975 and 2000, at SLAC and Fermilab, the τ and ν_τ were discovered respec-

tively to complete the third generation of leptons.

→ The agreement between years of experimental research and the SM's theoretical predictions is an illustration of its success as it's demonstrated in Figure 2.5, where it summarizes ATLAS measurements of cross sections for various production processes which agree with theoretical predictions over ten orders of magnitude [16].

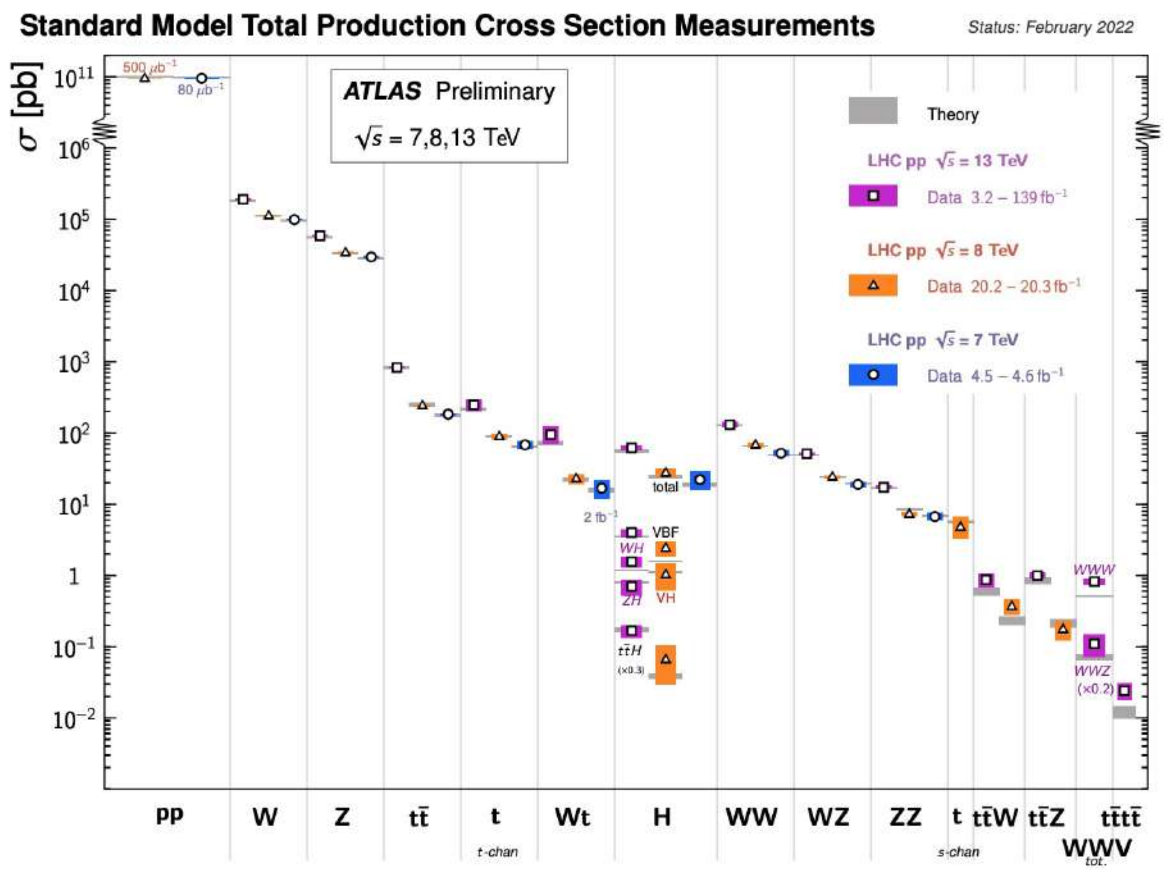

Figure 2.5: Summary of SM cross section measurements at the ATLAS detector as of February 2022. The measurements are corrected for branching fractions, compared to the corresponding theoretical expectations [16].

- Limitations

  - One of the major problems that the Standard Model couldn't solve is the Neutrino's mass. The latest experiments on neutrinos imply that they oscillate, which means that they acquire masses (tiny mass). The SM couldn't exactly precise nor explain the masses and the mechanism behind them.

  - Gravity is one of the four fundamental forces that is not explained within the Standard Model. The gravity force carrier; the graviton; is yet still not observed by experiments and needs a new model to understand its properties.

[4]Mesons are particles made up of a quark and an anti-quark. They are bosons.

– In addition to the mentioned challenges above, the Standard Model cannot give reasons for the matter-antimatter asymmetry, the CP violation, large differences in the coupling constants of forces at low energy scales, having a simple group framework for unifying all the particles interactions, or so-called Grand Unified Theory (GUT).

– The Standard Model can only account for the observable matter, which makes up approximately 5% of the universe's total composition. The rest of the universe is filled with mysterious substances that are invisible to us, known as "dark matter".

2.2.4 Dark matter (DM)

Since we cannot directly detect the dark matter, we rely on indirect methods to study its properties. The strongest evidence of its existence arises from the examination of galactic rotation curves, which reveal a stark contrast between the observed luminous matter and the expected mass distribution based on stellar velocity profiles. Additional convincing evidences are derived from gravitational lensing measurements, cosmic microwave background (CMB) radiation observations, and various other sources as detailed in reference [17].

2.2.4.1 Dark matter detection methods

Before talking about the dark matter models and their candidate particles from a particle physics view, let's shed light on the possible detection modes of the dark matter (Figure 2.6):

- Annihilation (Indirect Detection):

  In this detection mode, since the dark matter is not detected, it is produced when its particles are annihilated with their anti-particles. The Fermi Gamma-Ray Space Telescope [18] is one of the experiments charged to search for the odd signals that may be resulting from the dark matter annihilation.

- Scattering (Direct Detection):

  In many modern physics devices, dark matter is directly detected through the scattering process of the Standard Model particles. For example, the LZ detector [19] utilizes 7 tonnes of active liquid xenon to search for dark matter particles that are scattered from the xenon nuclei, and scintillate when colliding with other particles.

- Production:

  At extremely high energies, the Standard Model particles collide in the production experiments such as the LHC (Chapter 3). The resulting particles from the collision

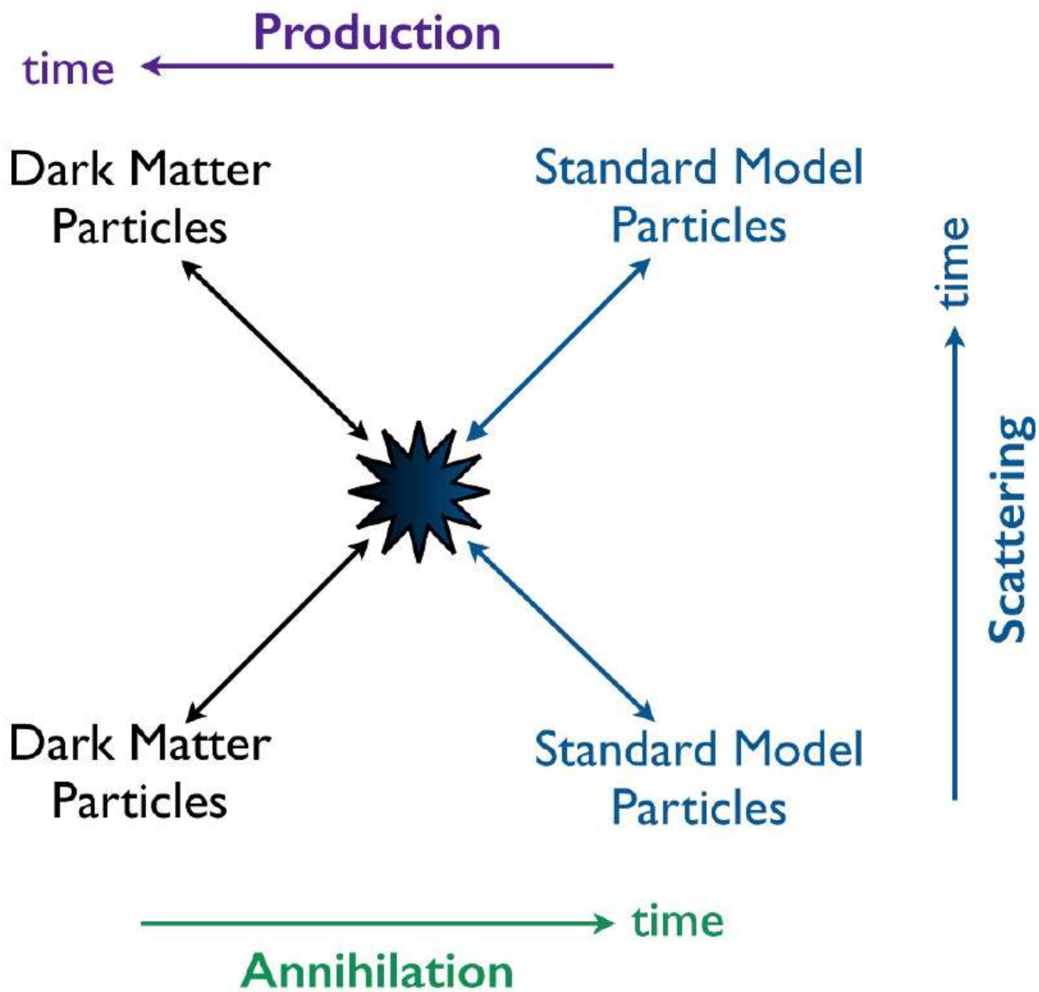

Figure 2.6: Possible dark matter detection methods.

may produce dark matter candidate particles along with huge showers of the SM particles.

2.2.4.2 Dark matter candidate particles

Numerous dark matter candidates have been suggested, as seen in Figure 2.7, to solve the earlier-mentioned problems in particle physics. In the present section, three most popular candidates for the role of DM will be discussed:

- WIMPs:

  WIMPs constitute a hypothetical class of exotic particles encompassing various proposed entities such as massive Dirac neutrinos, cosmions, and SuperSymmetry (SUSY) relics. These particles are characterized as stable, neutral, "weakly interactin" and do not exert any effects on baryonic matter. The predicted mass of WIMPs is approximately 100 GeV, a value comparable to that of the Higgs boson, leading to their sluggish movement and categorization as cold dark matter.

  According to Big Bang cosmology, many WIMP candidates are believed to have been created thermally in the early Universe, comparable to the particles of the Standard

Figure 2.7: Visualization of the possible solutions to the dark-matter problem in the form of a mind-map diagram [20]. The different colours indicate the different types of dark matter models classified on the basis of their characteristics.

Model, and will typically compose cold dark matter. To obtain the correct quantity of dark matter today, a self-annihilation cross-section of $< \sigma\nu > \simeq 3 \times 10^{-26} cm^3 s^{-1}$ is required, which is roughly expected for a new particle in the 100 GeV mass range that interacts via the electroweak force.

WIMPs are predicted by many extensions to the SM such as the SUSY [21], Universal Extra Dimension (UED) [22] and Little Higgs theories [23].

- Axions:

As a solution for the dark matter existence, the "strong CP" problem and the matter-antimatter imbalance, a hypothetical elementary particle beyond the SM, with spin 0 and electrically neutral, called the axion, was first proposed in 1977, with low mass and energy.

Even though axions are super light, they would have been numerous in the Big Bang. They weakly interact with gamma rays (photons), gluons, and fermions. Photon conversion is theorised to make axions: a photon and a photon from a magnetic field combine their energy to produce an axion.

The axion is introduced by adopting a new anomalous symmetry to the Standard Model along with a new scalar field which spontaneously breaks the symmetry at low energies, which is known as the Peccei–Quinn mechanism [24].

Current searches for axions include laboratory studies employing sensitive equipment such as sensors and antennas, in addition to searches in our Galaxy's halo and the Sun. For example, The CERN Axion Solar Telescope and IAXO are axion helioscopes designed to detect axions generated in the solar interior. ALPS at DESY and OSQAR at CERN use intense magnets to detect axions created during photon conversion.

- Sterile Neutrinos:

The Neutrino Oscillations indicate that the neutrinos we know to date have masses very close to 0, which is not the case in the SM prediction frame. Hypothetical fundamental particles were proposed to explain these oscillations and are called Sterile Neutrinos [25]. In this case, it is required to have more than the known three active neutrinos (ν_e, ν_μ and ν_τ).

The sterile neutrinos are expected to be right-handed neutrinos, and they are well motivated as an extension to the SM to explain the origin of the neutrinos' masses. Since they own a non-zero mass and have no electromagnetic charge, they don't interact with ordinary matter through weak force but only with gravitational one, which makes them possible DM candidates. With this and the fact that they have small masses, they are too difficult to detect, thus called "sterile".

Many experiments are dedicated to performing studies and research on sterile neutrinos, for example, the MINOS experiment, the IceCube experiment, the Daya Bay Reactor Neutrino Experiment, and the MiniBooNE experiment at FermiLab.

2.3 Beyond the Standard Model (BSM)

Many deficiencies of the SM need to be explained and understood, and that is the purpose behind adopting theoretical developments beyond the Standard Model, such as supersymmetry, string theory, and M-theory, etc. Among the extended theories, two are used in this analysis: The Hidden Abelian Higgs Model (HAHM) and the Two Higgs Doublet Model+scalar (2HDM+s) [26].

2.3.1 HAHM model: High Mass channel (HM)

The HAHM is an extension of the SM based on the gauge group $G \equiv SU(3)_C \otimes SU(2)_L \otimes U(1)_Y \otimes U(1)_d$. A $U(1)_d$ gauge symmetry is introduced and mediated by a relatively light Z_d boson (Z dark boson), which couples the SM to hidden sectors. In this model, the SM Higgs decays to two light Z_d bosons where their mass is considered to be in the range of [∼MeV-60GeV]. The mixing between the SM and the hidden sector is performed via kinetic mixing as formulated in the interaction Lagrangian [27]:

$$\mathcal{L}_{gauge} = -\frac{1}{4}B_{\mu\nu}B^{\mu\nu} + \frac{1}{2}\frac{\epsilon}{cos\theta_W}B_{\mu\nu}Z_d^{\mu\nu} - \frac{1}{4}Z_{d\mu\nu}Z_d^{\mu\nu}, \tag{2.20}$$

where ϵ is a small gauge kinetic mixing parameter that can take values in the range of $[\sim 10^{-17} - 10^{-2}]$,
$B_{\mu\nu} = \partial_\mu B_\nu - \partial_\nu B_\mu$, $Z_{d\mu\nu} = \partial_\mu Z_{d\nu} - \partial_\nu Z_{d\mu}$ are the $U(1)_Y$ and $U(1)_d$ boson fields respectively, and $cos\theta_W$ is the Weinberg mixing angle. The kinetic parameter in this case controls the coupling strength of the dark vector boson and the SM particles.

Another way the Standard Model couples to the hidden sector is via the Higgs mixing. In the Higgs potential V_0:

$$V_0 = -\mu^2|H|^2 + \lambda|H|^4 - \mu_d^2|S|^2 + \lambda_d|S|^4 + \kappa|H|^2|S|^2, \tag{2.21}$$

κ is the Higgs mixing parameter that controls the mixing between the dark Higgs boson S and the SM Higgs boson H.
Figure 2.8 shows the interaction between the SM and the dark sector via the **hypercharge portal** controlled by the ϵ parameter allowing the decays $H \to ZZ_d$ (Figure 2.8a), and via the **Higgs portal** allowing the $H \to Z_dZ_d$ and $S \to Z_dZ_d$ (Figure 2.8b) decays controlled by κ.

The decay of $Z_d \to f\bar{f}$ is governed by the ϵ parameter (in this study, only the decay

[5] $\mathcal{M}$ is the mass matrix element of the process.

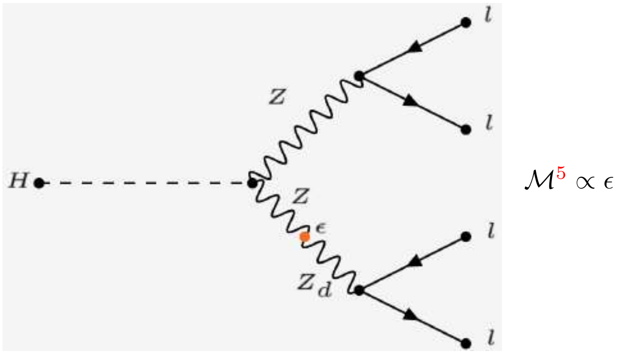

(a) Hypercharge portal

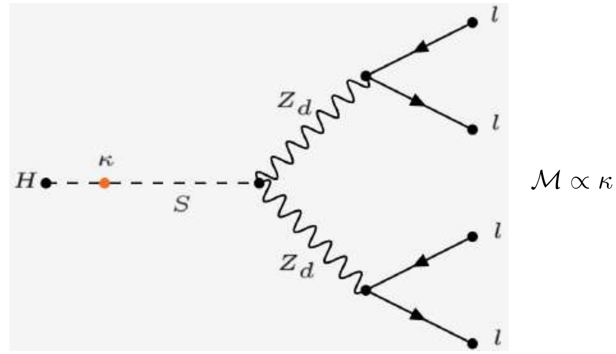

(b) Higgs portal

Figure 2.8: Feynman diagrams of $H \to ZZ_d \to 4l$ and $H \to Z_dZ_d \to 4l$ processes through the hypercharge and Higgs portals.

$Z_d \to l\bar{l}$ is considered with $l = e, \mu$).

We will assume that Z_d will promptly decay and that requires m_{Z_d} to be greater than ∼10 MeV [26] as Figure 2.9 is illustrating: In the regime where ϵ dominates ($\epsilon >> \kappa$),

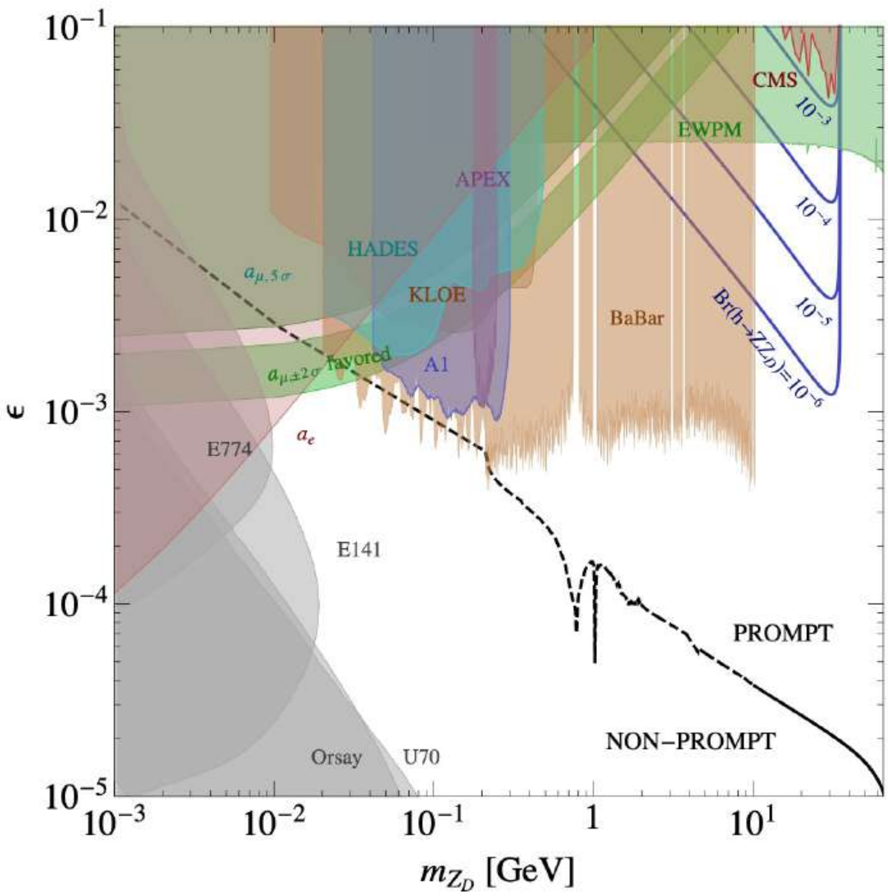

Figure 2.9: Constraints on ϵ for pure kinetic mixing for m_{Zd} ∼MeV-60 GeV. The black dashed line separates prompt ($c\tau < 1\mu m$) from non-prompt Z_d decays. The three blue lines are contours of $\mathcal{B}r(H \to ZZ_d)$ of 10^{-4}, 10^{-5}, 10^{-6} respectively [26].

the partial width for the $H \to ZZ_d$ decay mode to leading order in $m^2_{Z_d}/m^2_Z$ is:

$$\Gamma(H \to ZZ_d) = \frac{\epsilon^2 tan^2\theta_W}{16\pi} \frac{m^2_{Z_d}(m^2_H - m^2_Z)^3}{m^3_H m^2_Z v^2}, \quad (2.22)$$

where v is the vacuum expectation value of the SM Higgs ($v \approx 246$ GeV). Note that $\Gamma(H \to ZZ_d) \propto \epsilon^2$ and the existence of the kinetic mixing alone leads to $H \to ZZ_d$ as the dominant Higgs decay to Z_d. In addition, the decay to two Z_d is still possible by the presence of that kinetic mixing but it is highly suppressed by a factor of ϵ^4 since both Z bosons would need to mix with Z_d.

The second scenario that we have is when the Higgs mixing is dominating ($\kappa >> \epsilon$), then the Higgs decay $H \to Z_d Z_d$ is possible and its partial width to leading order in κ is [28]:

$$\Gamma(H \to Z_d Z_d) = \frac{\kappa^{'2}}{32\pi} \frac{v^2}{m_H} \sqrt{1 - \frac{4m^2_{Z_d}}{m^2_H}} \frac{(m^2_H + 2m^2_{Z_d})^2 - 8(m^2_H - m^2_{Z_d})m^2_{Z_d}}{m^4_H}, \quad (2.23)$$

where $\kappa^{'}$ is the effective Higgs mixing:

$$\kappa^{'} = \kappa \frac{m^2_H}{|m^2_H - m^2_S|} \quad (2.24)$$

with the m_S is the dark Higgs boson mass.
Equation 2.25 shows the interaction between the Z_d boson and the SM fermions, $Z_d \bar{f} f$, as:

$$\mathcal{L}_{Z_d \bar{f} f} = g_{Z_d \bar{f} f} Z_{d,\mu} \bar{f} \gamma^\mu f, \quad (2.25)$$

where $g_{Z_d \bar{f} f}$ is the coupling constant and it is given by:

$$g_{Z_d \bar{f} f} = \frac{g}{cos\theta_W}(-sin\alpha \ (t^3 cos^2\theta_W - Y sin^2\theta_W) + \eta \ cos\alpha \ sin\theta_W \ Y), \quad (2.26)$$

with α is the mixing angle [28], t^3 and Y are the weak isospin and hypercharge values respectively, and
η is defined as:

$$\eta = \frac{\epsilon}{cos\theta_W \sqrt{1 - \frac{\epsilon^2}{cos^2\theta_W}}} \quad (2.27)$$

The lowest order dark boson decay width to a pair of SM fermions is:

$$\Gamma(Z_d \to \bar{f} f) = \frac{N_c}{24\pi m_{Z_d}} \sqrt{1 - \frac{4m^2_f}{m^2_{Z_d}}} \left[m^2_{Z_d}(g^2_L + g^2_R) - m^2_f(-6g_L g_R + g^2_L + g^2_R)\right], \quad (2.28)$$

where $g_{R,L} = g_{Z_d \bar{f}_{R,L} f_{R,L}}$ as given in Equation 2.26, N_c takes 1 for leptons and 3 for quarks and m_f is the fermion's mass.
The branching ratio $\mathcal{B}r(Z_d \to \bar{f} f)$ vs. the Z_d mass is shown in Figure 2.10.

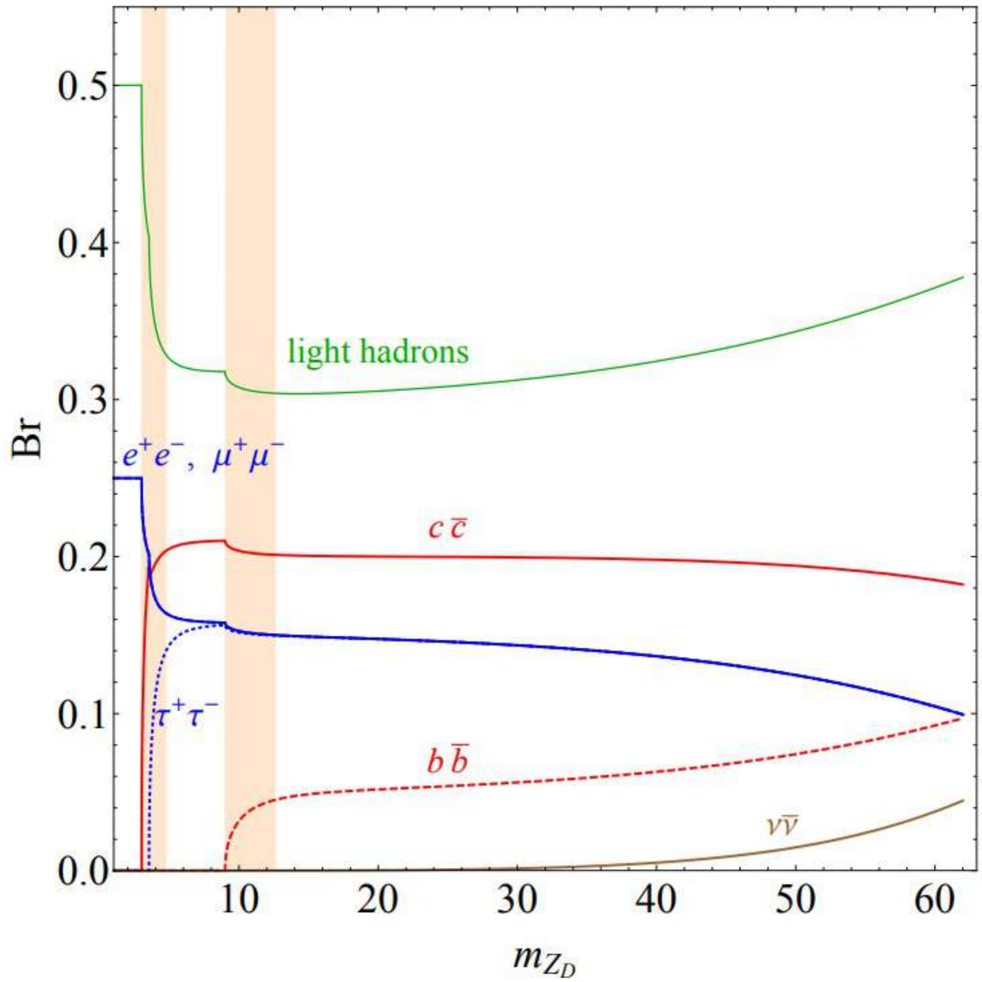

Figure 2.10: Branching ratio of the Z_d decay to SM fermions at lowest order assuming the decays to dark sector are kinematically forbidden [26].

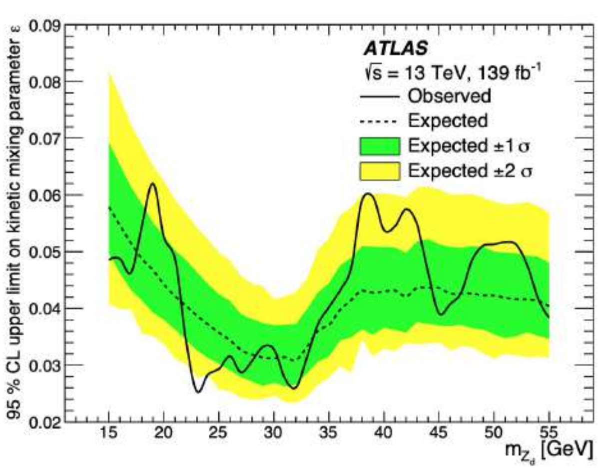

(a)

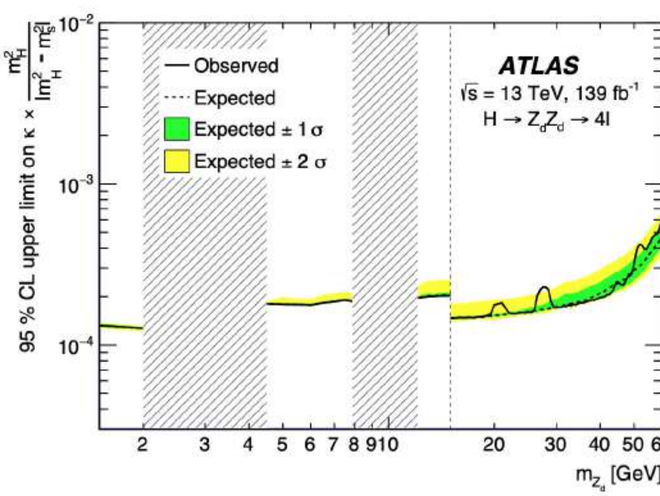

(b)

Figure 2.11: 95% upper limits set by the ATLAS experiments on the kinetic mixing parameter (a) and on the Higgs mixing parameter (b) with full Run2 data at $\sqrt{s} = 13$ TeV.

In Figure 2.11, upper limits at 95% CL have been set on ϵ and κ' with the 2015-2018 data-set [9] for an integrated luminosity of $139 fb^{-1}$ by the ATLAS detector.

2.3.2 Two Higgs Doublet Model+scalar (2HDM+S): Low Mass channel (LM)

As mentioned before, the 2HDM+S model is another simple extension to the SM and one of the natural choices for BSM models containing two Higgs doublets instead of just one. It is well motivated by several theories like electroweak baryogenesis, supersymmetry, Grand unification theory, and CP violation, etc.

The Higgs sector of the 2HDMs consists of two $SU(2)_L$ scalar doublet $\Phi_i (i = 1, 2)$ with hypercharge $Y = \frac{1}{2}$:

$$\Phi_i = \begin{pmatrix} \phi_i^+ \\ (v_i + \phi_i^0 + iG_i^0)/\sqrt{2} \end{pmatrix}, \tag{2.29}$$

where $v_i (i = 1, 2)$ are the vacuum expectation values (vev) of the doublets after the electroweak symmetry breaking, given as $v = \sqrt{v_1^2 + v_2^2} = 246$ GeV.

The general 2HDM Higgs potential is given by:

$$\begin{aligned} V(\Phi_1, \Phi_2) = {} & m_{11}^2 \Phi_1^\dagger \Phi_1 + m_{22}^2 \Phi_2^\dagger \Phi_2 - m_{12}^2 (\Phi_1^\dagger \Phi_2 + \Phi_2^\dagger \Phi_1) + \frac{\lambda_1}{2} (\Phi_1^\dagger \Phi_1)^2 + \frac{\lambda_2}{2} (\Phi_2^\dagger \Phi_2)^2 \\ & + \lambda_3 \Phi_1^\dagger \Phi_1 \Phi_2^\dagger \Phi_2 + \lambda_4 \Phi_1^\dagger \Phi_2 \Phi_2^\dagger \Phi_1 + \frac{\lambda_5}{2} \left[\left(\Phi_1^\dagger \Phi_2 \right)^2 + \left(\Phi_2^\dagger \Phi_1 \right)^2 \right], \end{aligned} \tag{2.30}$$

To avoid the tree-level flavour-changing-neutral-currents (FCNCs) caused by the Yukawa couplings to fermions, a discrete Z_2 symmetry is imposed to ensure that fermions with the same quantum numbers all couple to only one Higgs field, which results in four possible choices of fermion couplings as summarized in Table 2.2:

- Type I: All fermions couple to just one of the Higgs doublets(conventionally chosen to be Φ_2).
- Type II: The $Q = 2/3$ right-handed (RH) quarks couple to one Higgs doublet(Φ_2) and the $Q = -1/3$ right-handed quarks with RH leptons couple to the other doublet (Φ_1).
- Type III: The Lepton-specific model is where the RH quarks all couple to the Φ_2 and the RH leptons couple to Φ_1.
- Type IV: The flipped model where the $Q = 2/3$ RH quarks couple to Φ_2 and the $Q = -1/3$ RH quarks couple to Φ_1 and the RH leptons couple to Φ_2.

Types	Φ_1	Φ_2
Type I	–	u_R^i, d_R^i, l_R^i
Type II	d_R^i, l_R^i	u_R^i
Type III(Type L)	l_R^i	u_R^i, d_R^i
Type IV (Type F)	d_R^i	u_R^i, l_R^i

Table 2.2: The four type leading to natural flavour conservation, where i is a generation index. The u_R^i is, by convention, always coupling to Φ_2.

After the Electroweak Symmetry Breaking (EWBS), the scalars mix with each other to form the mass eigenstates:

$$\begin{pmatrix} H^\pm \\ G^\pm \end{pmatrix} = \begin{pmatrix} cos\beta & -sin\beta \\ sin\beta & cos\beta \end{pmatrix} \begin{pmatrix} \phi_2^\pm \\ \phi_1^\pm \end{pmatrix}, \tag{2.31}$$

$$\begin{pmatrix} A^0 \\ G^0 \end{pmatrix} = \begin{pmatrix} cos\beta & -sin\beta \\ sin\beta & cos\beta \end{pmatrix} \begin{pmatrix} G_2^0 \\ G_1^0 \end{pmatrix}, \tag{2.32}$$

$$\begin{pmatrix} h \\ H \end{pmatrix} = \begin{pmatrix} cos\alpha & -sin\alpha \\ sin\alpha & cos\alpha \end{pmatrix} \begin{pmatrix} \phi_2^0 \\ \phi_1^0 \end{pmatrix}, \tag{2.33}$$

where α and β are the mixing angles, and $tan\beta = v_2/v_1$.

In general, 2HDM could allow for exotic decays of the 125 GeV state of the form $h \to AA$, $H^0 \to hh, AA$ or $h \to ZA$ decaying to gauge bosons or SM fermions. However, the 2HDM models are constrained from existing data [29, 30]to allow for various exotic Higgs decays.

To avoid these restrictions [26]:

- we assume that 2HDM model is near or in the decoupling limit, $\alpha \to \beta - \pi/2$, and with considering the lightest state h, identical to the SM Higgs.
- we add one complex scalar singlet to the 2HDM:

$$S = \frac{1}{\sqrt{2}}(S_R + iS_I) \tag{2.34}$$

Under these two assumptions, the following exotic Higgs decay are possible in the 2HDM+S:

$$h \to ss \to X\bar{X}Y\bar{Y}\ ,\ h \to aa \to X\bar{X}Y\bar{Y} \text{ and } h \to aZ \to X\bar{X}Y\bar{Y}, \tag{2.35}$$

where $s(a)$ is a (pseudo)scalar mass eigenstates composed of $S_R(S_I)$ and X, Y are SM fermions or gauge bosons.

The branching ratios of $a \to SM$ according to different types, and depending on $tan\beta$, that can be considered in the 2HDM+S model are:

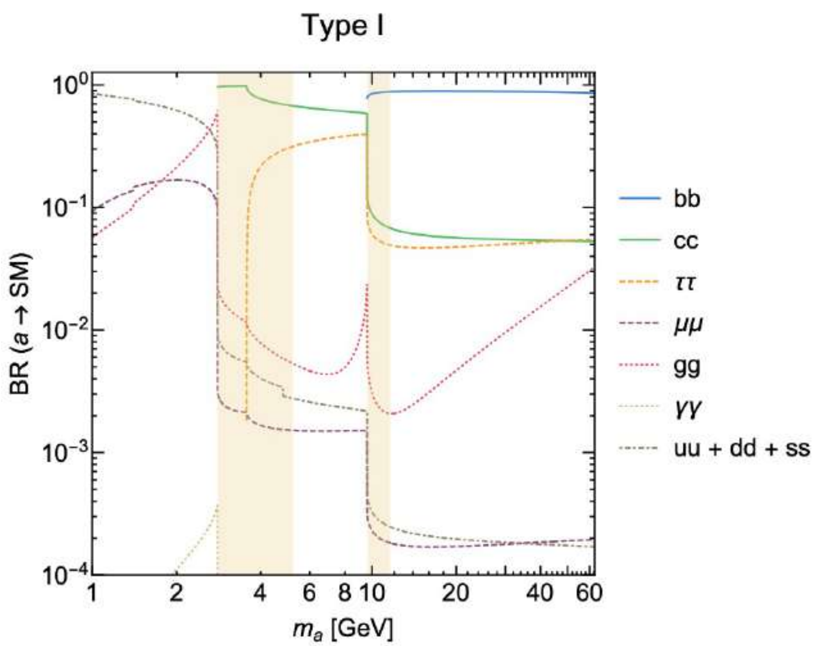

Figure 2.12: Branching ratios of $a \to \bar{f}f$ in the 2HDM+S model for type I Yukawa coupling. Decays to quarkonia likely invalidate our simple calculations in the shade regions [26].

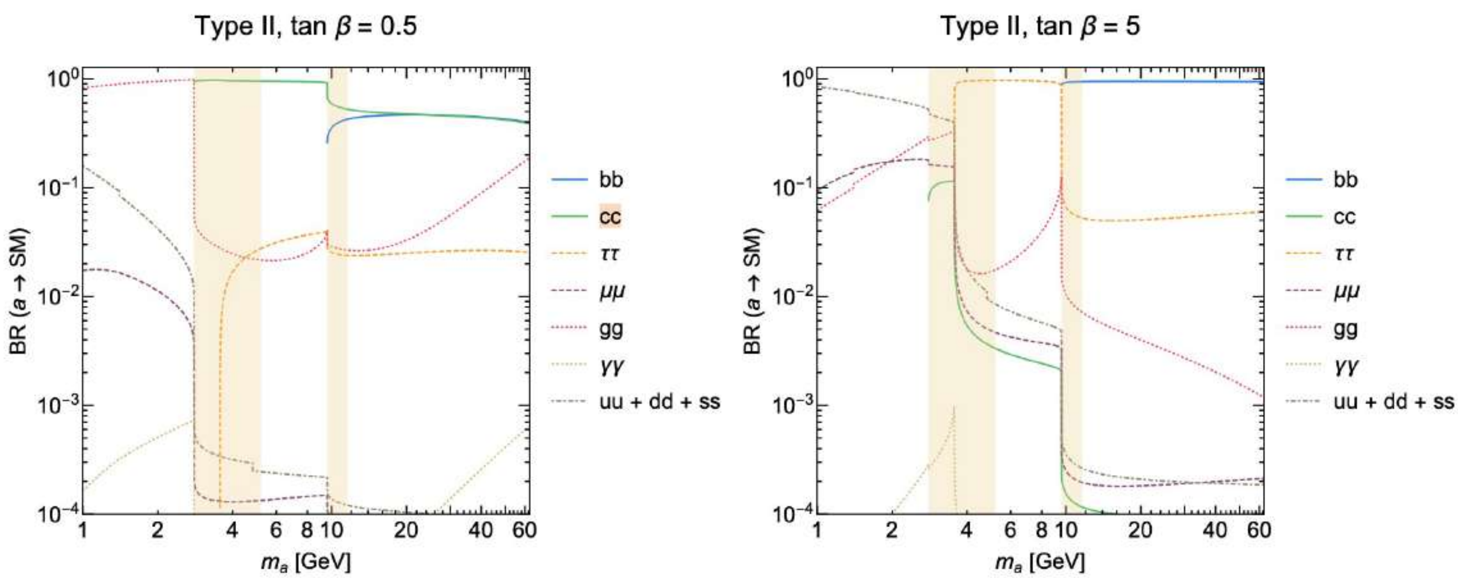

Figure 2.13: Branching ratios of $a \to \bar{f}f$ in the 2HDM+S model for type II Yukawa coupling. Decays to quarkonia likely invalidate our simple calculations in the shade regions [26].

→ Type I (Figure 2.12): the branching ratios in this type are independent of $tan\beta$ since all fermions couple to Φ_2.

→ Type II (Figure 2.13): the branching ratios are dependent of $tan\beta$ considering the decay to down-type fermions is suppressed for $tan\beta < 1$ and enhanced for $tan\beta > 1$.

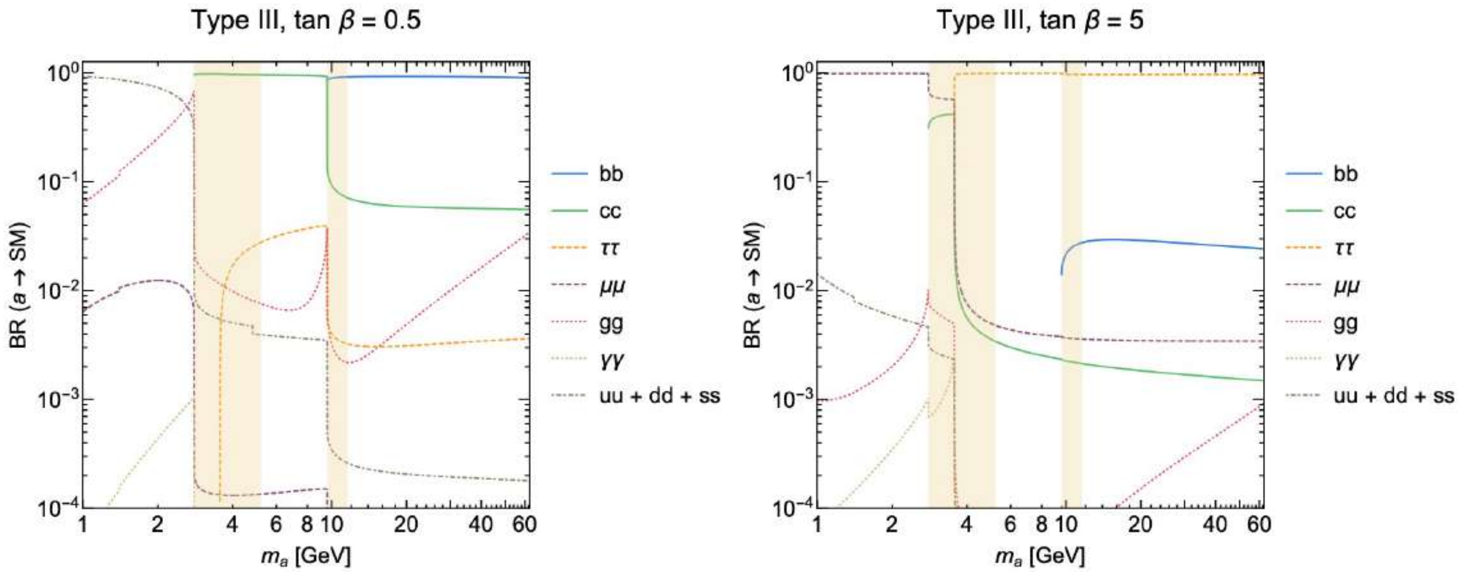

Figure 2.14: Branching ratios of $a \to \bar{f}f$ in the 2HDM+S model for type III Yukawa coupling. Decays to quarkonia likely invalidate our simple calculations in the shade regions [26].

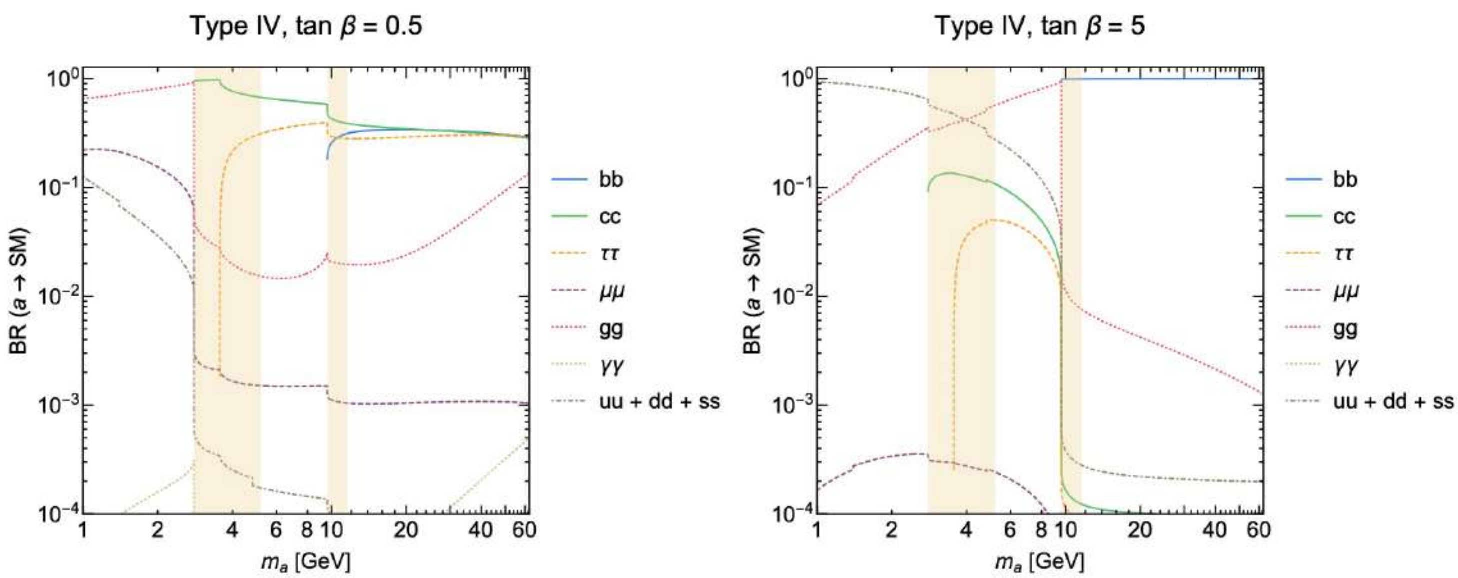

Figure 2.15: Branching ratios of $a \to \bar{f}f$ in the 2HDM+S model for type IV Yukawa coupling. Decays to quarkonia likely invalidate our simple calculations in the shade regions [26].

→ Type III (Figure 2.14): the branching ratios are dependent of $tan\beta$. For the case where $tan\beta > 1$, pseudo-scalars decays to leptons are reinforced over decays to quarks, while for $tan\beta < 1$ the decays to quarks are enhanced over decays to leptons.

→ Type IV (Figure 2.15): the branching ratios are dependent of $tan\beta$. For $tan\beta < 1$, the pseudo-scalar decays to up-type quarks and leptons can be reinforced concerning down-type quarks.

Figure 2.16 illustrates the branching ratio of $H \to aa$ in the 2HDM+S benchmark considering the Type III Yukawa coupling where the decay to $\mu\mu$ is favored over the decays to quarks ($tan\beta > 1$) in the range $2m_\mu < m_a < 2m_\tau$ for the process $H \to aa \to 4\mu$.

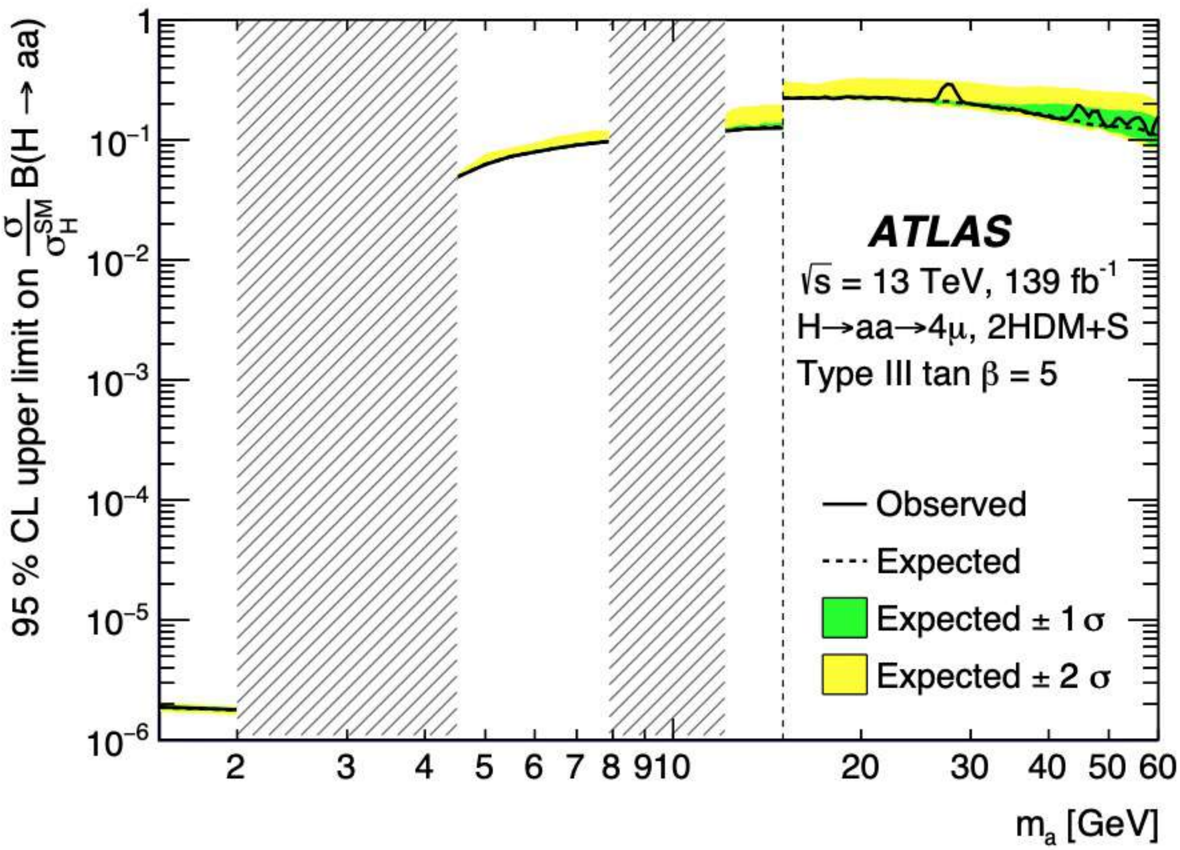

Figure 2.16: the $H \to aa$ process for the benchmark 2HDM+S model. The shaded areas are the quarkonia veto regions. The step changes at m_a=15 GeV are due to the change in selection from the Low Mass (LM) ($1 < m_a < 15$ GeV) to the High Mass (HM) ($15 < m_a < 60$ GeV) analysis [9].

2.3.3 Additional Scalar channel(AS)

The additional scalar channel opens up a wide search field beyond the Standard Model to look for Dark Matter (DM) candidates by mixing the SM and the dark sector Higgses.

A dark Higgs field is introduced to spontaneously break the dark $U(1)$ gauge symmetry. The dark scalar (S) mixes with the SM (H) one via the Higgs mixing portal as represented in the Feynman diagram in Figure 2.8b.

The new scalar's mass is outside the 125 GeV SM Higgs's mass window and will decay to two Z_d bosons, though in this case, there are no constraints on the Z dark boson to be lighter than the SM Z boson. The process is controlled by the Higgs mixing parameter κ, and the ϵ parameter is still considered to ensure the decay of the dark boson to SM fermions.
In the present thesis, the search studies the decay of the dark scalar in a mass range of [30,800] GeV excluding the SM Higgs mass window of $115 < m_{4l} < 130$ GeV, to two dark bosons which their masses are between $15 < m_{2l} < 250$ GeV, giving four leptons in the final states; $S \to Z_d Z_d \to 4l$ $(4e, 4\mu,$ and $2e2\mu)$.

A heavier Z_d would have other decay channels into dark sectors states, thus becoming invisible. To avoid that and to still have the $Z_d \to ll$ decay mode, we would need to assume that the Z_d is the lightest state in the dark sector so that only the SM decays occur.

Chapter 3

LHC and ATLAS detector

The largest and most powerful tool considered to give a chance to dig deeper into the universe's mysteries and answer some open and fundamental physics questions is the Large Hadron Collider (LHC).

The latter produces accelerated protons and collides them at a high centre of mass energy inside four main interaction points and the ATLAS detector is one of them. The reconstruction and the identification of particles produced in the collisions require measuring their momentum, energy deposits, and other properties by multiple ATLAS sub-detectors accurately designed for that purpose.

In this chapter, a detailed description of the LHC and the ATLAS detector is presented along with designs of its sub-detectors.

3.1 The Large Hadron Collider

The Large Hadron Collider was constructed and built by the European Organisation for Nuclear Research (CERN), with international contributions and collaborations, in a 27 km circular tunnel and located 175 meters below ground on the France-Switzerland borders.

The tunnel consists of two parallel adjacent beam pipes, each having oppositely circulating beams of accelerated opposite-sign protons up to 6.8 TeV per beam. To maintain the two counter-rotating beams focused, on their circular paths and maximize the interaction chances, 1232 dipole magnets, and 392 quadrupole magnets, with other stronger quadrupole magnets, are installed.

The beams are circulating as particle groups captured within one radio-frequency bucket, which we call bunches. Each beam is bunched up to 2808 bunches, each containing 115 billion protons. Every 25 *ns*, the bunches are crossed at a collision rate of 40

MHz.

The particles are produced by the *pp* or *heavy ion*[1] collisions, before being injected in the LHC. The production process entails passing by a series of pre-accelerators that successively increase the energy of particles. Table 3.1 briefly summarises these systems and Figure 3.1 shows the whole accelerator complex at CERN [31].

System	Purpose
LINAC4	The linear particle accelerator 4[2] designed to generate negative hydrogen ions with 160 MeV.
PSB	The Proton Synchrotron Booster is designed to strip electrons from the Hydrogen ion and leave the nucleus of one proton. It accelerates then the protons with 2 GeV.
PS	The Proton Synchrotron accelerates the energy of the protons to 26 GeV.
SPS	The Super Proton Synchrotron accelerates the protons to 450 GeV before being lastly injected into the LHC ring.

Table 3.1: The pre-accelerating systems of protons at CERN.

After reaching the LHC accelerator, the particles collide at four main interaction points along the LHC, at each point, an experiment is installed to detect and observe the resulting collisions: ATLAS, CMS (are the large general-purpose particle detectors), LHCb, and ALICE which have more specialized roles.

3.1.1 Luminosity and pile-up

The most significant quantity that the LHC is characterised by is the number of collisions per unit of time, which is expressed as luminosity:

$$N = \sigma \times L = \sigma \int \mathcal{L} dt, \tag{3.1}$$

where σ corresponds to the cross-section of a given interaction process, L is the integrated luminosity that considers the total number of events during a period of data-taking. It is measured in units of $area^{-2}$, specifically in units of inverse femtobarns (fb^{-1}), where $1b = 10^{-24} cm^2$. On the other hand, $\mathcal{L}$ is the instantaneous luminosity that measures how tightly particles are packed into a given space, such as the LHC's proton beam. Maximising the instantaneous luminosity means a greater rate of particles will collide, thus rare processes will be produced. It is given as:

$$\mathcal{L} = \frac{N^2 N_b f}{4\pi \sigma_x \sigma_y} S, \tag{3.2}$$

[1]The LHC can as well accelerate Xenon and Lead nuclei.
[2]replaces the LINAC2 after the long shutdown in 2019-2020.

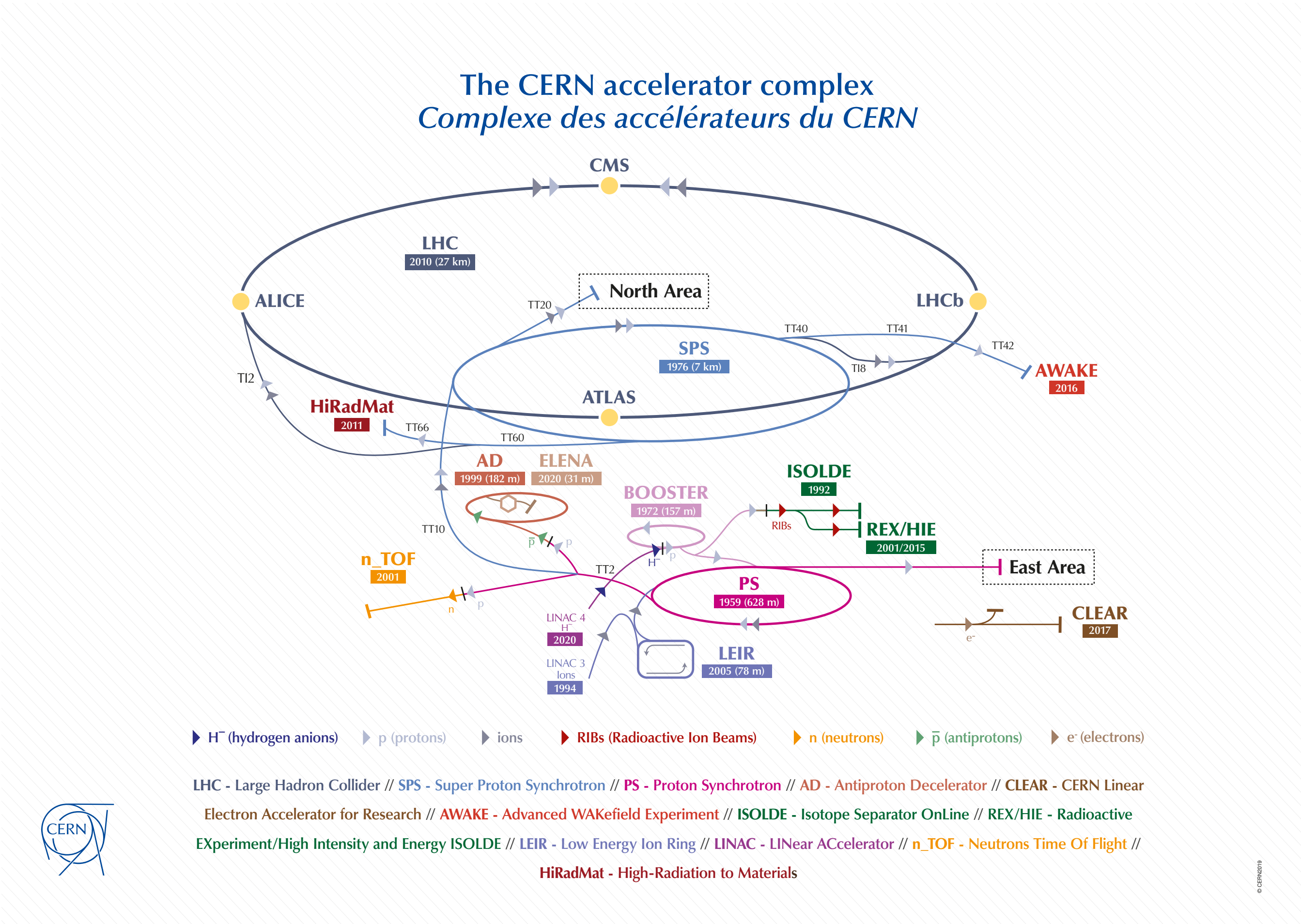

Figure 3.1: The CERN accelerator complex.

considering N the number of particle per bunch, N_b the number of colliding bunches, f bunch frequency, a geometric factor S, and the horizontal and vertical bunch sizes $\sigma_x \sigma_y$, respectively.
The unit used for the instantaneous luminosity is $cm^{-2}s^{-1}$. The design luminosity of the LHC is $\mathcal{L} = 10^{34}cm^{-2}s^{-1}$ and a peak luminosity of $2 \times 10^{34}cm^{-2}s^{-1}$ was reached in Run 2.

Regrettably, achieving a substantial peak luminosity is not without its drawbacks. With the occurrence of a bunch crossing, multiple separate pp interactions come into play. The resulting particles tend to overlap within the detector, introducing the complexity of distinguishing physics entities originating from the desired process.

The average count of inelastic pp interactions is denoted as the pileup parameter μ and its time-averaged value is represented as $< \mu >$, as given in Equation 3.3, often referred to as in-time pileup. As the luminosity increases, so does the level of the pile-up, leading to greater overcrowding of energy depositions within the detector.

$$< \mu > = \frac{\mathcal{L}_{bunch} \sigma_{inelastic}}{f_{rev}}, \tag{3.3}$$

where $\mathcal{L}_{bunch}$ is the instantaneous luminosity per bunch, $\sigma_{inelastic}$ is the inelastic cross section for pp interaction and f_{rev} is the revolution frequency of the accelerator. Figure 3.2 represents the average number of interactions per bunch crossing during Run2 data-taking.

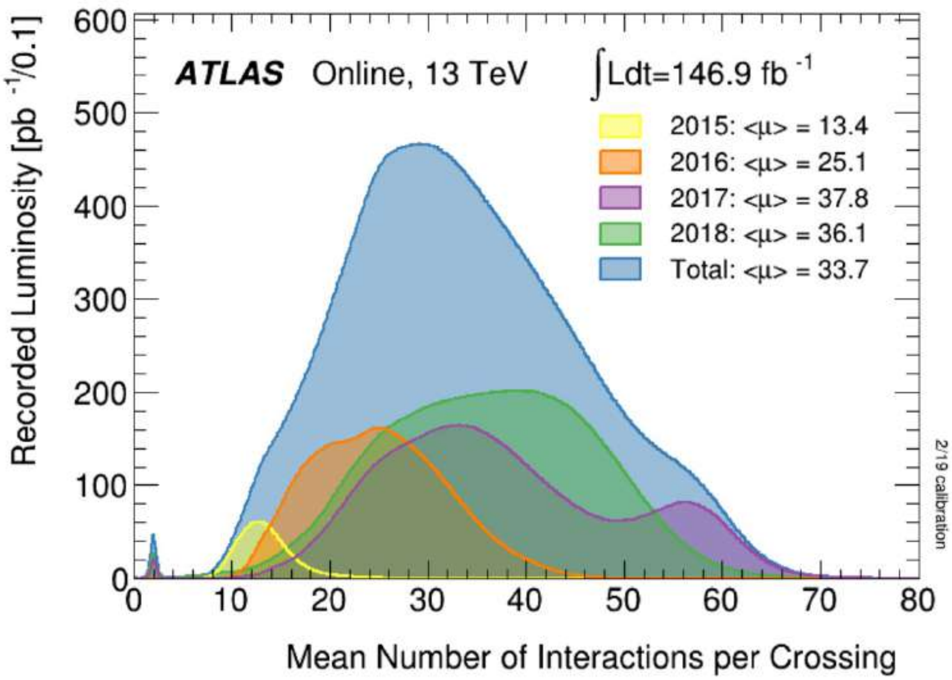

Figure 3.2: The mean number of interactions per crossing during Run2 [32].

3.1.2 Run2 LHC performance

The analyses utilized data gathered during the LHC operations at a centre-of-mass energy of 13 TeV, referred to as Run2 data. Spanning from 2015 to 2018, this time frame saw the LHC generating proton-proton collisions, resulting in an accumulated integrated luminosity of 156 fb^{-1}. Among this total, 139 fb^{-1} of data were recorded under stable beam and detector conditions, constituting a dataset suitable for physics analyses within the ATLAS experiment.

Figure 3.3 illustrates the collected integrated luminosity throughout the duration of Run2. Remarkably, Run2 witnessed exceptional accomplishments from the LHC, surpassing the originally planned instantaneous luminosity and producing a higher integrated luminosity than anticipated. This heightened instantaneous luminosity led to an increased count of interactions per bunch crossing over the years, with an average value of $< \mu >$ $= 33.7$ for the entire Run2 period. This stands in contrast to the value of approximately $< \mu > \approx 20$ observed during Run1.

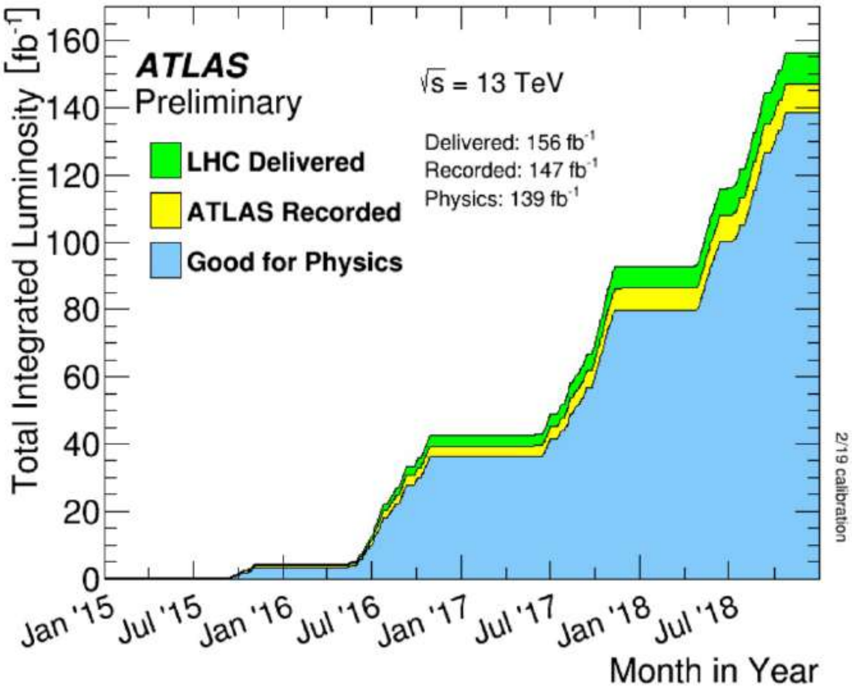

Figure 3.3: Luminosity delivered by the LHC during the Run-2 data taking. ATLAS recorded this data with an efficiency above 90% [32].

3.2 ATLAS detector

ATLAS stands for "A Toroidal LHC Apparatus" and it is the largest, general-purpose particle detector at LHC, designed to explore a wide range of physics by performing precise measurements of known processes and also discovering new physics, and this by utilizing the high energy and luminosity of the LHC.

It consists of five primary systems, concentric cylinders around the interaction point, each unexclusively targeting a different set of particles as shown in Figure 3.4:

- **Inner Detector (ID):** is the closest detector surrounding the beam axis. Its basic role is to identify the charged particles' trajectories when they hit the material at discrete points via energy deposits which leads to knowing the particles' identity and momentum.

- **Calorimeters:** They determine the particles' energy electromagnetically interacting with the **electromagnetic (EM) calorimeter** like electrons and photons, and hadronically interacting with the **hadronic calorimeter** as jets by measuring their energy deposits.

- **Muon Spectrometer (MS):** surrounds the calorimeters and is designed for the identification of the muons and the measurement of their trajectories and momentums.

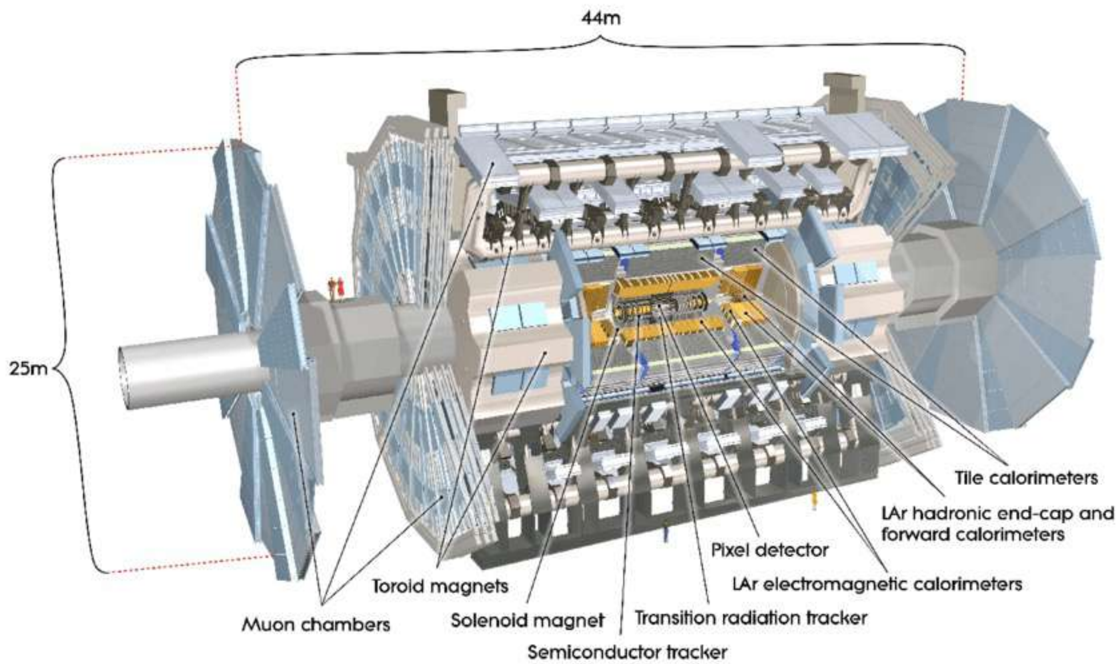

Figure 3.4: Cut-away view of the ATLAS detector [33].

- **Magnets system:** consists of two large magnet systems; a solenoid that surrounds the ID, a barrel toroid, and two end-cap toroids surrounding the calorimeters and within the MS. They are designed in a way to bend the trajectory of the charged particles so that their momentum can be measured using the Lorentz force by quantifying the radius of the curvature of the particles as given in Equation 3.4:

$$r = \frac{p}{q.B}, \tag{3.4}$$

  where p is the relativistic momentum of the particle, q is it's electric charge and B is the magnetic field intensity.

- **Trigger system:** receives the output of the detector and buffers it to select fast pre-reconstructed events and store them to be retained for detailed analyses.

3.2.1 Inner Detector

The Inner Detector is the innermost highly sensitive part of the ATLAS detector due to its prominent role in detecting and observing the decay products of the collision. It is composed of three sub-systems aiming to measure different properties of the charged particles.

The Id is immersed in a $2\,T$ magnetic field generated from the solenoid, and it extends over a length of 6.2 m with a diameter of 2.1 m as it is illustrated in Figure 3.5 and detailed here [33].

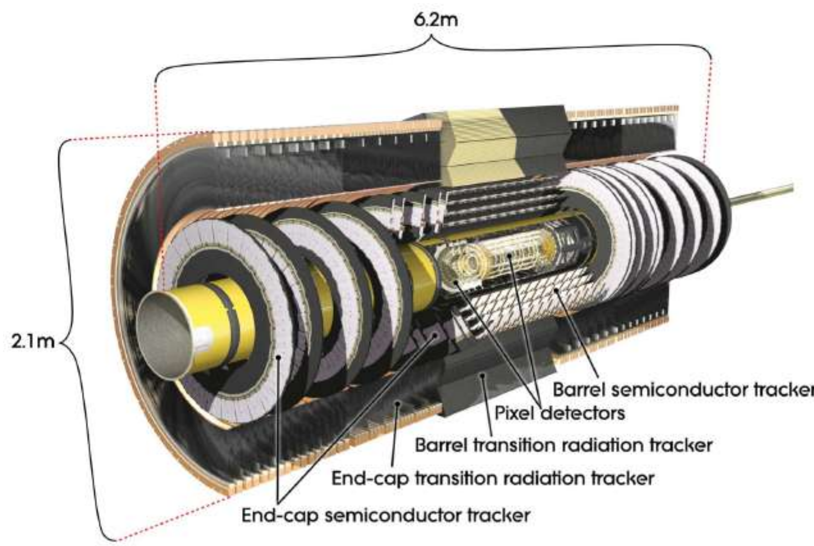

Figure 3.5: Cut-away view of the Inner detector.

3.2.1.1 Pixel Detector

Is the nearest layer of the ID to the interaction point, located 3.3 *cm* from the beam line. It consists of three barrel silicon pixel layers and three layers in each end-cap and an insertable B-Layer (IBL) which is responsible for spanning the whole pseudo-rapidity range of the ID. The Pixel Detector typically provides four measurements per track. The detector is compact with over 92 million read-out channels. The signals of the energy deposits left behind in the Pixel detector by charged particles help measure their origin and momentum.

3.2.1.2 SemiConductor Tracker

Surrounding the Pixel detector, the SemiConductor Tracker (SCT) is used to reconstruct tracks of the charged particles. It has the same concept as the Pixel Detector but uses micro-strips of silicon sensors rather than small pixels. Due to its optimized layout, the SCT is considered to be the most critical part of the ID since it measures particles over a broader range than the Pixel Detector and for tracking in the perpendicular plane to the beam line. It is composed of four layers of silicon strips in the barrel and nine in the end-cap which provide eight measurements per track.

3.2.1.3 Transition Radiation Tracker

The Transition Radiation Tracker (TRT) consists of 4 *mm* diameter thin-walled cylindrical drift tubes called "straws" each is up to 144 *cm* long and filled with mixture of $X_e - CO_2 - O_2$ gas or $Ar_e - CO_2 - O_2$ gas [34]. Once the straw is crossed by a charged particle, the gas inside is ionized to create an electric signal that is used later to reconstruct tracks. Between the tubes, materials with widely varying indices of refraction cause ultra-relativistic charged particles to produce transition radiation and leave much stronger signals in some straws and provide information on the particle type whether it is an electron or a pion.

By gathering information from the three sub-detectors, a transverse momentum resolution is calculated with the following equation and given in GeV:

$$\frac{\sigma_{p_T}}{p_T} = 0.05\% p_T \oplus 1\%. \tag{3.5}$$

$\oplus$ indicates a sum in quadrature.

3.2.2 Calorimeters

They are located outside the solenoid magnet surrounding the ID to measure the energy of particles created in LHC collisions. They are designed in a way to force the particles to leave and deposit their energies to be measured by absorbing them in high-density metals.

The two basic calorimeter systems are:

3.2.2.1 The Electromagnetic Calorimeter (ECal)

Also named the **Liquid Argon (LAr) Calorimeter**, designed to absorb and measure the energy of the electromagnetically interacted particles (charged particles and photons) with high precision of the amount and the location of the deposited energy.

The accordion-shaped Kapton electrodes of the calorimeter ensure that no particles have escaped detection and identification. Once the passing-through particles are absorbed, they are converted by the metal layers into a shower of low-energy particles that ionize the liquid argon situated between the layers producing electric currents to be combined and measured. The Electromagnetic Calorimeter consists of a barrel part covering $|\eta| < 1.475$ and two end-cap components covering up to $|\eta| < 3.2$, each part of the calorimeter is surrounded by its cryostat to keep them sufficiently cool.

The particles' shower early mentioned is distinguished by its radiation length in the longitudinal plane X_0, which is referred to the average distance x that an electron needs to travel in the material to reduce its energy by the factor of $1/e$ of its original energy. This radiation length governs the rate at which electrons lose energy by bremsstrahlung [35].

The energy resolution of the ECal is:

$$\frac{\sigma_E}{E} = \frac{10\%}{\sqrt{E}} \oplus 0.7\%. \tag{3.6}$$

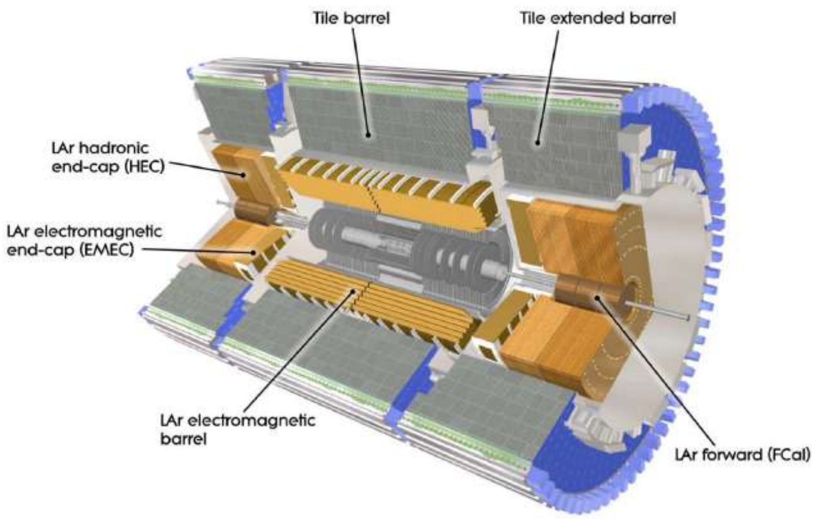

Figure 3.6: Cut-away view of the Calorimeter system in ATLAS [33].

3.2.2.2 The Hadronic Calorimeter (HCal)

The Hadronic Calorimeter consists of the Tile Calorimeter, the Liquid-Argon Hadronic End-Cap calorimeter (HEC) and the Liquid-Argon Forward Calorimeter (FCAL).

The so-called **Tile Calorimeter**, is complementing the measurements done by the EM Calorimeter, by measuring the energy of the hadron particles which interact via the strong force and don't deposit all of their energy in the EM Calorimeter. It is a sampling calorimeter using steel as energy-absorbing material and scintillating tiles as an active material to sample the deposited energy. It is composed of one barrel and two extended barrels covering $|\eta| < 1.0$ and $0.8 < |\eta| < 1.7$ respectively.

Once the hadrons hit the steel layers, a shower of new daughter particles is generated and the scintillating tiles then produce photons to be converted to electrical currents. The parent particle's energy is then proportional to the intensity of the current.

The **LAr Hadronic End-cap Calorimeter (HEC)** [33, 36] is structured in two independent wheels in each end-cap and placed behind the end-cap EM calorimeter and sharing the same cryostats. They have copper as an absorber and LAr as active material.

The **LAr Forward Calorimeter (FCAL)** [33, 37] consists of 3 modules FCAL1, FCAL2 and FCAL3. The first one is made of copper and is closest to the Interaction Point. The other two modules are mainly made of tungsten to optimize the transverse and longitudinal hadronic shower containment.

The targeted energy resolution for the HCal is:

$$\frac{\sigma_E}{E} = \frac{50\%}{\sqrt{E}} \oplus 3\%. \quad (3.7)$$

3.2.3 Muon Spectrometer

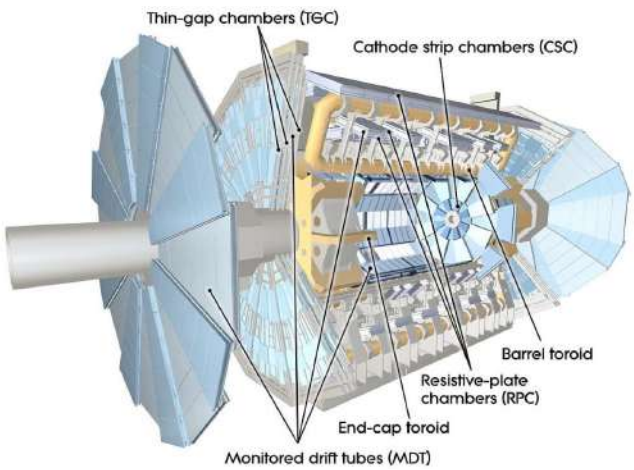

Figure 3.7: Cut-away view of the Muon system in ATLAS [33].

The Muon Spectrometer (MS) is the outer layer of the ATLAS detector dedicated to providing a high-quality stand-alone muon identification and measurement of its momentum along with triggering in high pseudo-rapidity coverage. Since muons are 200 times heavier than electrons, they can cross several thick layers of the detector.
It consists of three main parts:

1. Three toroidal magnets provide a magnetic field.
2. Precision detectors which are a set of chambers measuring and high-precising the outgoing muons' tracks.
3. Fast-response detectors are a set of triggering chambers.

The momentum measurement is meant to be in a range of 3 GeV to 3 TeV in a range of $|\eta| < 2.7$. A magnetic field is produced in the range of $|\eta| < 1.4$ by a barrel toroid providing 1.5 to 5.5 Tm of bending power and in the region $1.6 < |\eta| < 2.7$ covered by two end-cap toroids which approximately provide 1 to 7.5 Tm. The deflected muons in this magnetic field produced by the three superconducting air-core toroids are then measured by a combination of high-precision (Monitored Drift Tubes, Cathode Strip Chambers) and triggering (Resistive Plate Chambers, Thin Gap Chambers) chambers.

The **Monitored Drift Tubes** (MDTs) is one of the precision tracking sub-detectors of MS, they perform mechanical isolation in the drift tubes of each sense wire from its neighbours and provide a robust and reliable operation. Each chamber is composed of a pressurized 29.97 mm diameter drift tube which operates with Ar/CO_2 gas at a high pressure of 3 bar, where a central tungsten-rhenium wire is placed with a diameter of 50 μm at which the electrons resulting from the ionization of the gas are collected inducing an electric signal.

The **Cathode Strip Chambers** (CSCs) are covering $2 < |\eta| < 2.7$ and are the first and most inner layer of the end-cap. They have the same principle as the MDTs of gas ionization but they are using multiple wires instead of one wire per tube. These multi-wires are proportional chambers with the wires oriented in the radial direction. The strips of one cathode are oriented perpendicular to the wires providing the precision coordinate and the other one is parallel to the wires providing the transverse coordinate. The CSC system consists of one large and one small disk each having 8 chambers.

The trigger chambers are the ones responsible for providing the track information of muons traversing the detector. For that purpose, two different technologies have been used:

The **Resistive Plate Chambers** (RPCs) are the chambers in the barrel region covering $|\eta| < 1.05$ located on and between the 8 coils of the superconducting barrel toroid magnet and assembled with the MDTs in a common mechanical support structure. The barrel chambers consist of three concentric stations: two in the Barrel Middle region (BM) to trigger low-p_T muons ($p_T < 10$ GeV), and one Barrel Outer required to provide high-p_T trigger information.

The **Thin Gap Chambers** (TGC) have the same principle as CSCs and are placed in the end-cap region covering $1.05 < |\eta| < 2.4$. As they are multi-wire proportional chambers, they give good time resolution and high rate capability. TGCs consist of four layers; one is located in front of the second MDT wheel (TGC1), two are behind (TGC2 and TGC3) and one is located in front of the innermost tracking layer.

More information on each kind of chamber is more detailed in [33].

The overall momentum resolution $\frac{\sigma_{p_T}}{p_T}$ provided by the muon system is:

$$\frac{\sigma_{p_T}}{p_T} = 10\%, \text{ at } \ p_T = 1\text{TeV}. \tag{3.8}$$

3.2.4 Magnet system

The magnet system in ATLAS is a hybrid system of two different types of superconducting magnets which can provide strong magnetic fields that bend trajectories of charged particles so that their momentum can be measured [33, 38].

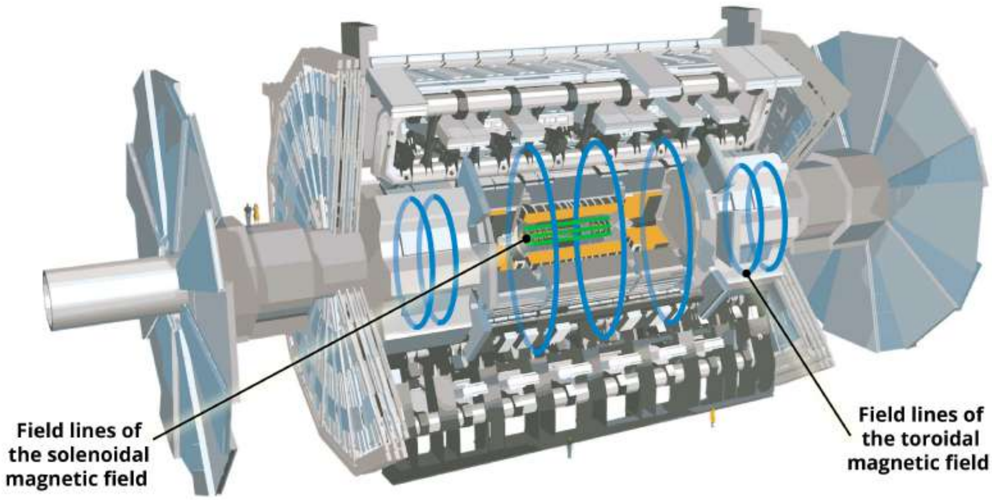

Figure 3.8: Illustration of ATLAS magnetic fields [39].

The central **Solenoid** magnet provides 2 *Tesla* axial magnetic field and surrounds the inner detector. It is 5.6 m long, 2.56 m in diameter and weighs over 5 *tonnes*. Its high magnetic field allows the very energetic particles to be curved and their momentum to be precisely measured due to its uniform direction.

The **Toroidal** magnet system is composed of three toroid magnets. Each is a series of eight coils; one toroid in the barrel region (BT) surrounding the Calorimeters and within the Muon Spectrometer providing 3.9 *Tesla*, and two toroids in the end-cap regions (ECT) designed to provide up to 4.1 *Tesla* used to measure the muons' momentum.

3.2.5 Trigger system

Before handling the permanently stored data that are worth studying in detailed physics analyses, the collision events pass through some steps to ensure the optimal data-taking conditions and select the most interesting data containing important characteristics that might lead to discoveries.

The Trigger system is used for selecting interesting collision events for study.

The ATLAS trigger system performs a fast event reconstruction of physics objects on two levels:

- The first-level hardware trigger (L1), is constructed with custom-made electronics and searches for high transverse momentum physics objects(muons, electrons, photons jets and hadronically decaying τs) along with large missing E_T. It works basically on a subset of information from the Calorimeters like the reduced granularity and from the Muon Spectrometer using the trigger chambers in the barrel and end-cap regions as mentioned in Section 3.2.3. The decision to save or reject an event data is made in less than 2.5 μs and the rate of kept events is reduced in the read-out from 40 MHz to 100 kHz.

- The High-Level Trigger (HLT) is software-based, running on farms built from commodity computing and network technology. It is subdivided into the second-level trigger (L2) and the Event Filter (EF). They reduce the rate of accepted events to around 2 kHz and 200 Hz respectively.

By using complicated algorithms, the HLT makes the final decision regarding the accepted events in just 200 μs. The remaining data are then stored for further offline analyses.

3.3 ATLAS upgrade for HL-LHC

The future trajectory for the instantaneous luminosity delivered by the LHC involves incremental escalations through successive upgrades of the accelerator. These enhancements are aimed at managing the augmented event rate and higher pile-up. In response, the LHC experiments are conducting upgrades across various detector components as well. The primary modifications to the detector setup occur during the extended periods of shutdown (LS), namely in 2019-20 (LS2 encompassing Phase-1 upgrades) and the scheduled time frame of 2025-27 (LS3 with Phase-2 upgrades). Throughout LS2 and LS3, diverse upgrades for both detectors and accelerators are planned for implementation in ATLAS and LHC.

Following LS2, the LHC's Run3 is anticipated to accumulate approximately 300 fb^{-1} of data, potentially operating at an increased centre-of-mass energy ($\sqrt{s}$ = 14 TeV). The beginning of Run3 data collection was originally scheduled for the outset of 2021, but due to the outbreak of the coronavirus (Covid-19) pandemic, the timeline had to be postponed to 2022. Subsequently, the LHC will undergo another upgrade during LS3, designated as the High-Luminosity (HL-LHC) phase. This upgrade is poised to elevate the instantaneous luminosity, resulting in the delivery of 3000 fb^{-1} of data over a decade. An overview of the LHC's operational plan is visually presented in Figure 3.9.

Figure 3.9: The current schedule for the LHC and HL-LHC upgrade [40].

The mean pile-up is expected to reach $< \mu > = 200$ throughout the High-Luminosity LHC (HL-LHC) operations. To effectively manage these challenging circumstances, the proposed upgrades for ATLAS include the replacement of the Inner Detector (ID) during the LS3 by the Inner Tracker (ITk) [42]. The ITk constitutes a silicon-based detector comprised of pixels and strips. Its design aims to maintain tracking and vertex performances that are at least comparable to those exhibited under HL-LHC conditions.

Chapter 4

Thermal Performance study of the ATLAS ITk Strip Modules at BNL

4.1 Introduction

In order to increase the capability of the LHC's detectors and their sensitivity to new physics beyond the SM, the LHC is expected, in the third Long Shutdown, to be upgraded to the High Luminosity phase (HL-LHC) where the integrated luminosity will be up to 3000 fb^{-1}. In this phase, the average number of $p-p$ collisions per bunch crossing will be up to 200, corresponding to a peak instantaneous luminosity of $7.5 \times 10^{34} cm^{-2}s^{-1}$, which will cause higher radiation levels by a factor of 20 and more pileups. All these new features are causing an increase in bandwidth, occupancy, as well as radiation damage, which are considered a strong motivation to upgrade the innermost part of the ATLAS detector to handle these new conditions.

The Inner Tracker referred to as ITk, is an all-silicon tracking system that will supersede the existing ID, and is designed in a way to cover a wider area, to be faster, and to be resistant to the resulting radiations.

4.2 ITk Strip detector

The Inner Tracker will contain silicon pixel and silicon strip sensors in the barrel and the forward regions. The pixel detector contains five barrel layers and four end-cap ring layers, while the strip detector consists of four barrel layers, and in each end-cap region, six disks. The two inner barrel layers of the strip detector are occupied by Short Strip (SS) modules followed by two layers of Long Strip modules (LS).

Figure 4.1a shows the layout of the ATLAS ITk detector with the pixel elements in red and the strip detector in blue. The barrel regions are represented with horizontal lines parallel to the beam line, and the vertical lines are for the end-caps with respect to the

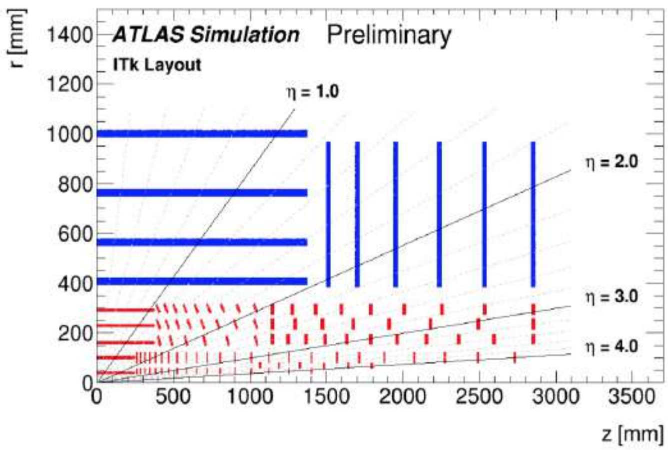

(a) [42]

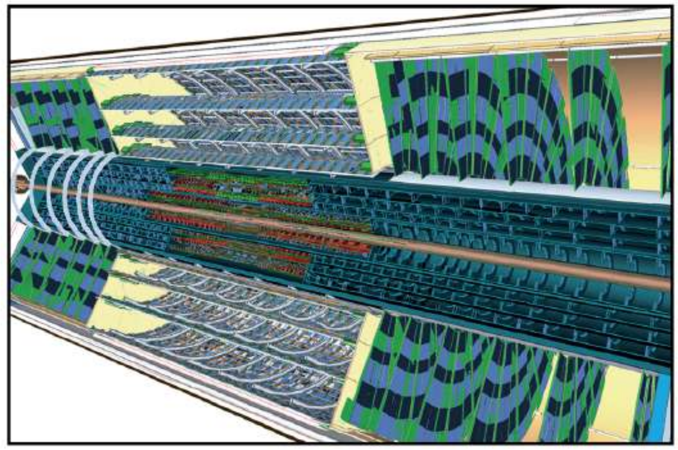

(b)

Figure 4.1: Layout of the ATLAS ITk detector

measured radius from the interaction point (Figure 4.1b).

4.2.1 ITk Strip Staves and Petals

The silicon strips find their home in local support structures crafted from carbon fibre, referred to as "staves". In the barrel region, there are 28 modules evenly distributed, with 14 on each side, as depicted in Figure 4.2. These staves, serving as the fundamental components of the Strip detector, play a crucial role in delivering essential electrical and optical services to ensure stability. These services encompass data and power transmission, cooling mechanisms, timing synchronization, and data control. The ITk Strip Staves and Petals are:

- Staves (Barrel) and Petals (End-cap) are the support structure for the modules.
- They hosts the common electrical, optical connections and cooling services.
- 28 Barrel modules on each stave (14 modules per side).
- 18 End-Caps modules on each petal (9 modules per side, R0-R5).

4.2.2 ITk Strip Modules

In Figure 4.4, the configuration of each ITk strip module encompasses a silicon sensor, one or two hybrids, and the powerboard. The silicon sensors are characterized by n-type implant strips on a p-type bulk, featuring an active thickness of approximately 300 m. The use of n-in-p sensors ensures that detector signals primarily emanate from electrons. Consequently, the transit time for charge carriers is shorter compared to p-in-n sensors, attributed to the superior mobility of electrons relative to holes, leading to diminished

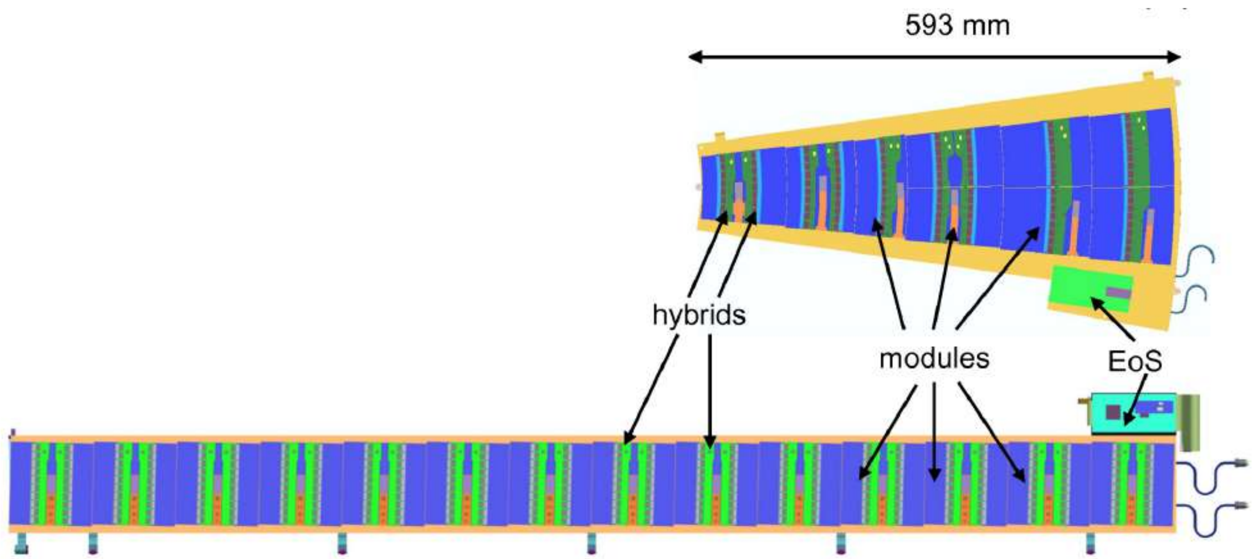

Figure 4.2: Sketch of barrel short strip stave.

losses from charge trapping [41, 42]. Furthermore, n-in-p sensors remain resistant to type inversion under irradiation. P-stop implants serve the purpose of isolation between strips. The module's individual channels for readout are AC-coupled to the n-type strips. In summary the building blocks of the ITk strip detector:

- Consists of the sensor, one (for long strip, LS 4.3a) or two (for short strip, SS 4.3b), PCBs called Hybrid and one Power board.
- The hybrid hosts the readout ASICs: the ABCStar and the HCCStar.

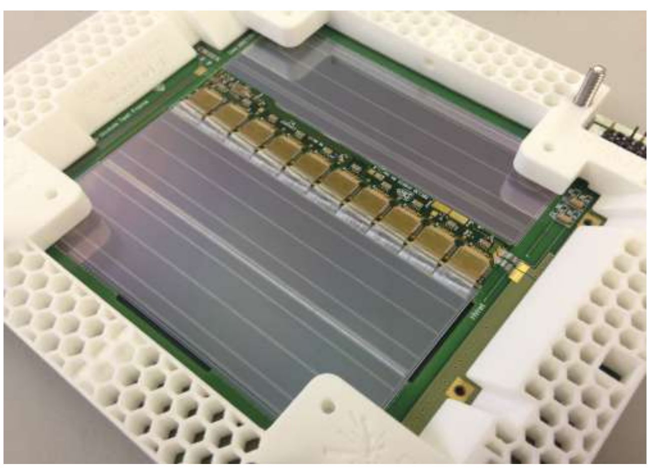

(a)

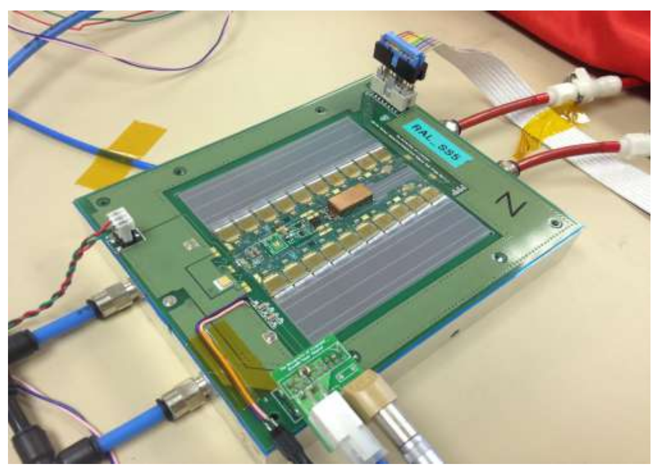

(b)

Figure 4.3: Prototype modules of LS (a) and SS (b).

The hybrid serves as a flexible PCB, housing the Application Specific Integrated Circuits (ASICs) for readout, specifically the ATLAS Binary Chips (ABCStar), affixed to it. The ABCStar chips establish direct communication with an HCCStar. Interconnection between the individual channels of ABCStar chips and the sensor strips is achieved through wire bonds. When a charged particle traverses the sensor, it generates a signal

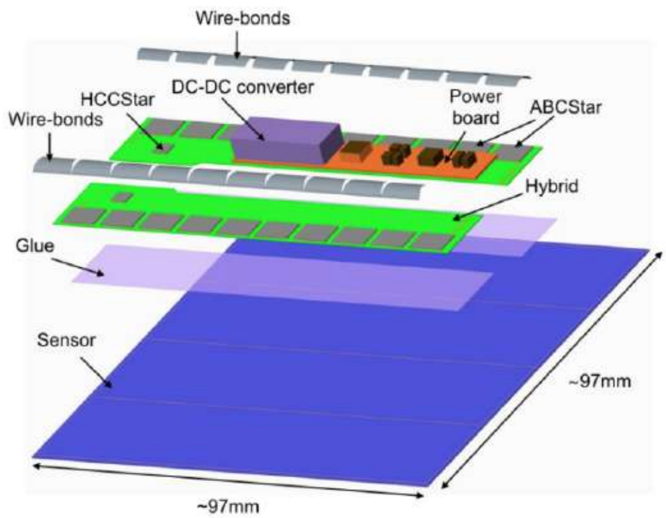

Figure 4.4: View of Short-Strip Module.

transferred to the input channels of the ABCStar chips. Subsequently, the analogue signal from each strip undergoes conversion to binary hit/no-hit data.

The front end of the ABCStar chips incorporates a charge-sensitive pre-amplifier and gain stage, a shaper, a discriminator, a pipeline accommodating 256 channels, and a buffer. Additionally, a cluster algorithm is employed to compress data for efficient output. Following the gain stage, the voltage signal is compared with a threshold in the discriminator, resulting in the generation of binary output. This binary output is then stored in the pipeline memory. This process ensures effective signal processing and data compression, enhancing the efficiency of the overall system.

This chapter aims to elucidate the investigation into the impact of thermal cycling on the operational efficacy of both the electrical and cooling services embedded within the staves. These staves serve as pivotal components in both the Inner Tracker and the local support structures for the barrel regions. The comprehensive description of the experimental setup utilized for monitoring temperature and humidity within the enclosure is presented in the subsequent section, emphasizing the criticality of ensuring stave reliability at low temperatures. The chapter concludes by synthesizing the findings derived from the conducted experiments.

4.3 Experimental setup

The Strip detector, configured to house 392 staves, assigns Brookhaven National Laboratory (BNL) the responsibility of constructing half of this quantity. In the preliminary pre-production stage, one side of the Long Strip modules stave was assembled in early

2022, with the assembly of the other side set for May 2022. In pursuit of precision, a dedicated clean room at BNL is employed for stave testing within a controlled environment, utilizing a coldbox where both humidity and temperature are meticulously regulated, as illustrated in Figure 4.5.
The experimental setup employed in this study featured a coldbox housing the stave, enhanced with a chiller designed to lower the stave's temperature. This configuration also included a booster pump, which augmented the cooling process for the remote modules of the stave. Temperature measurements were facilitated by a TC08 [43] logger, monitoring both the chiller pipes and the interior of the box through strategically placed thermocouples. Additionally, SHT85 [44] sensors were incorporated to gauge the humidity levels within the box. The environmental sensor readout was managed by a Raspberry Pi4 [45], contributing to the comprehensive data collection and analysis process.

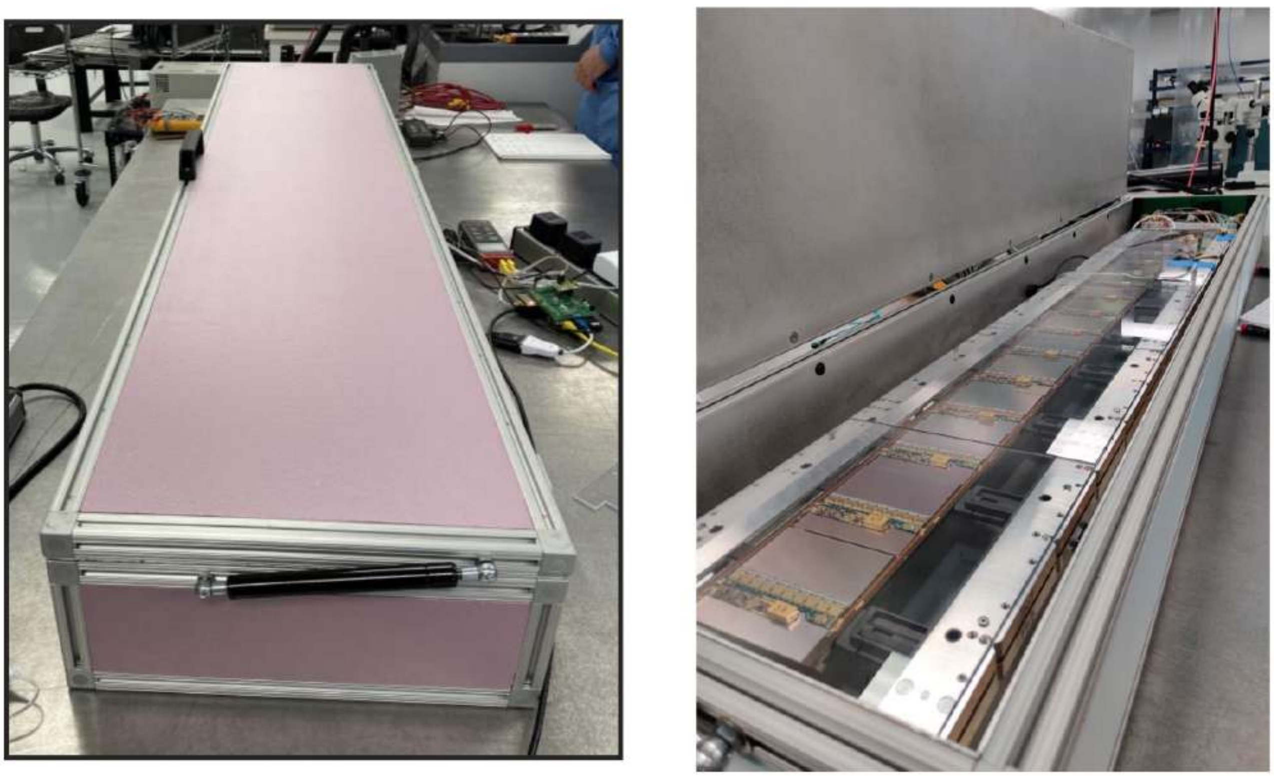

(a) (b)

Figure 4.5: Coldbox (a) with a stave installed inside (b).

- **<u>USB-TC08 data logger:</u>**

  The USB TC-08, illustrated in Figure 4.6a, serves as an advanced data logger equipped with eight channels capable of accommodating eight thermocouples simultaneously. This device is meticulously designed to swiftly and precisely monitor temperature variations across an extensive range from -270 °C to +1820 °C, leveraging the capabilities of these thermocouples sensors.

To facilitate compatibility with diverse temperature ranges, the USB TC-08 supports various thermocouple types (B, E, J, K, N, R, S, T). The specific thermocouple type employed is contingent upon the targeted temperature range. In the context of the presented scenario, Figure 4.6b exemplifies the use of Type K thermocouples, chosen for their suitability.
In the specific thermal cycle testing mentioned, a total of four thermocouples are employed. Two of these thermocouples are strategically positioned to measure the temperature of the chiller pipes, while the remaining two are placed inside the cold-box. This configuration enables comprehensive monitoring of temperature dynamics throughout the thermal cycle test.

(a)

(b)

Figure 4.6: USB TC-08 data logger (a) with Type K thermocouple (b).

- **SHT85 sensor:**

The SHT85 sensor stands out as a precision instrument tailored for exacting humidity and temperature measurements in challenging environments and test scenarios. Its pin-type connect design, exemplified in Figure 4.7, facilitates seamless integration and replacement. Notably, the sensor's exceptional reliability and enduring stability make it a preferred choice for demanding applications.

Operating within a temperature range of 20°C to 50°C, the SHT85 sensor is optimized for various conditions. However, considering the lower temperature degrees expected during the thermal cycle testing of the stave, temperature measurements solely rely on the data logger. In this context, two SHT85 sensors will be strategically deployed to gauge humidity levels inside the coldbox, harnessing the sensor's precision and dependability for accurate measurements throughout the testing process.

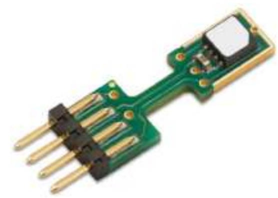

Figure 4.7: SHT85 humidity and temperature sensor.

- **Raspberry Pi4:**

The Raspberry Pi4 stands out as an affordable single-board computer crafted to foster programming skills, support hardware projects, facilitate home automation, and extend its utility to industrial applications. Running on Linux, it offers a distinctive feature set through its GPIO (General Purpose Input/Output) pins, empowering users to exercise control over electronic components for physical computing endeavours and delve into the realms of the Internet of Things (IoT).
In the context of this study, the Raspberry Pi4 assumes a pivotal role, serving as the powerhouse for environmental sensors and data logger readouts. Leveraging its computing capabilities and GPIO pins, it proves instrumental in orchestrating the collection and management of data from environmental sensors, exemplifying the versatile applications of the Raspberry Pi in the field of sensor technology and data acquisition.Figure 4.9 illustrates the diagram of the stave testing setup.

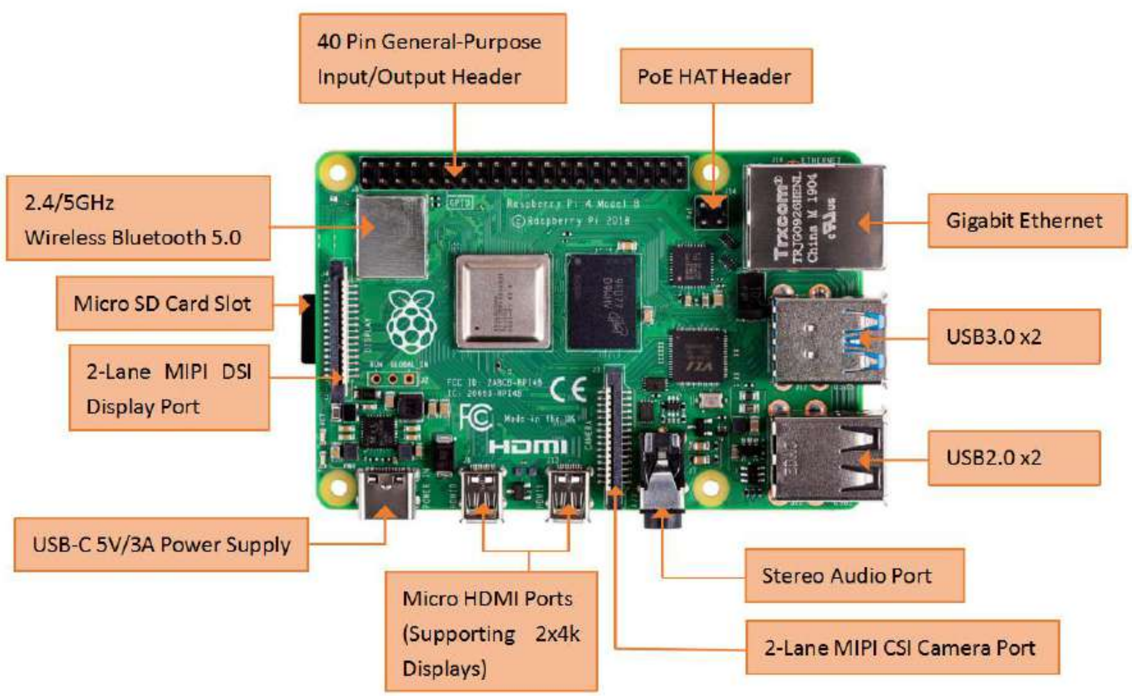

Figure 4.8: A peripheral interface overview of the Raspberry Pi4.

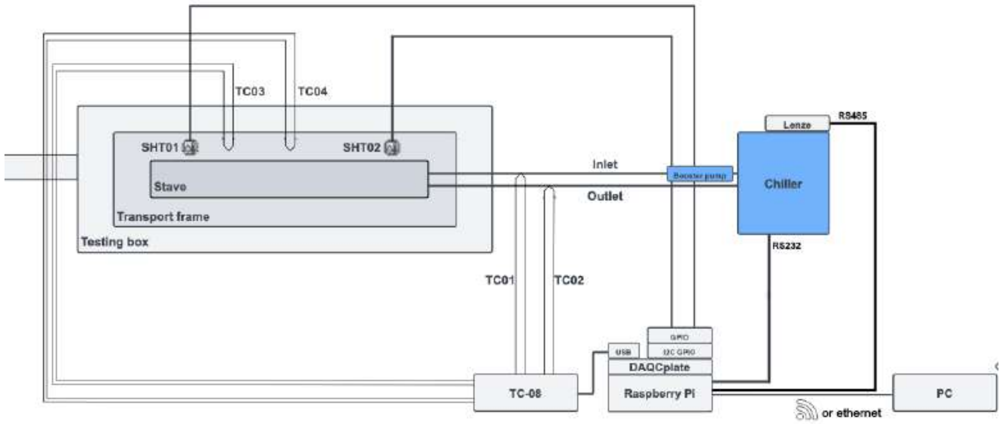

Figure 4.9: Diagram showing the setup used for the thermal cycle testing at the BNL clean room.

4.4 Thermal performance of the ITk Strip Module

During the interim phase between Module production and Stave assembly, each individual Module undergoes rigorous electrical and thermal quality control (QC) testing. This meticulous process involves subjecting each module to ten thermal cycles, ranging from -35 °C to +40 °C, meticulously measured by the Hybrid NTC. Modules that do not meet the specified criteria during these tests are meticulously addressed and handled accordingly. If feasible, these modules undergo repair and are subjected to retesting to ensure adherence to quality standards. This stringent quality control protocol ensures that only modules meeting the specified performance criteria proceed to the subsequent stages of Stave assembly, guaranteeing the overall reliability and integrity of the final product.

A Python-based control and readout software system are employed for monitoring the temperature and humidity of the stave throughout the thermal cycling process. The collected data is stored and retrieved using the InfluxDB [46] database and visualized through the Grafana [47] open-source software, as illustrated in Figure 4.10. This graphical representation depicts the time-dependent results of the thermal cycling process, initiated from room temperature (RT) down to -45°C (lower figure), concurrently capturing variations in humidity within the stave box (upper figure).

The outcomes of the thermal cycling experiment affirm the robustness of the examined ITk stave, demonstrating its capacity to endure a temperature range from 23°C to -45°C without encountering notable damage or performance degradation. Insights from Figure 4.10 include:

- The outlet pipe temperature exhibiting higher values than the inlet due to the stave core's thermal mass.
- Humidity augmentation inside the box observed when the dry air is deactivated, indicating a correlation between the absence of dry air and increased humidity.

- Upon resetting the chiller to room temperature, the air temperature rises, prompting an ongoing investigation into the humidity trend. Possible causative factors are being explored, including the evaporation of trapped water as a potential contributor.

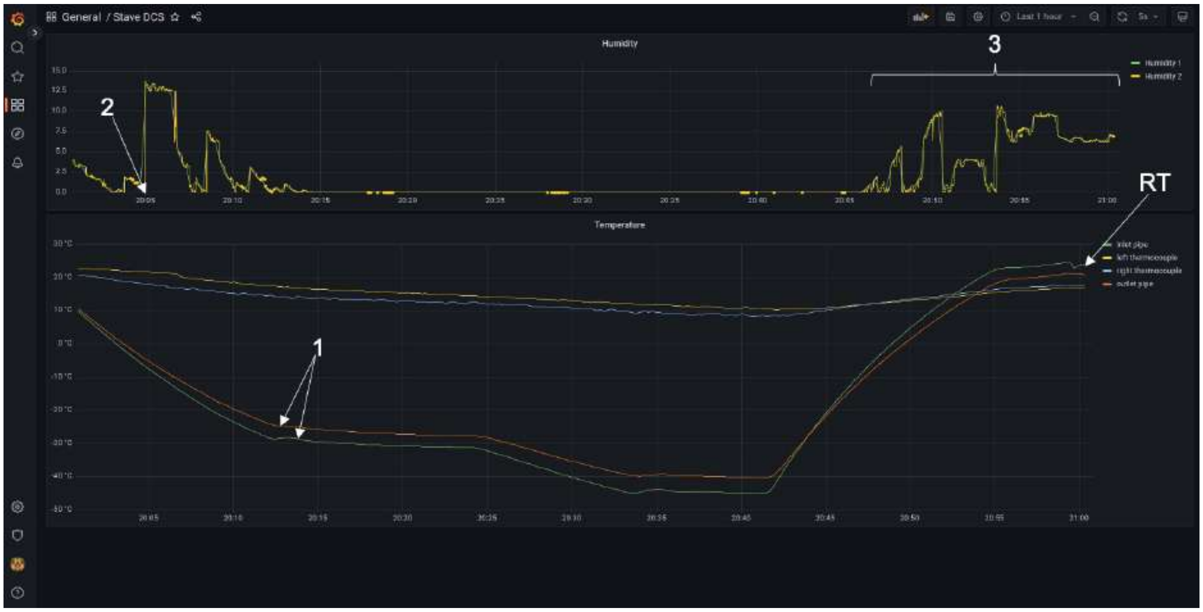

Figure 4.10: The humidity (top) and temperature (down) variations during the thermal cycle testing of the stave in the function of the measurement's time.

4.5 Conclusion

This study has successfully investigated the effects of thermal cycling on the performance of the Inner Tracker stave assembled at the BNL and demonstrated its effectiveness in coping with the High-Luminosity resulting radiations.

In future studies, two boxes will be used, in parallel, to straightforward the testing and gain time. For that purpose, an I2C multiplexer devise [48] was suggested to connect more than two SHT85 sensors for better humidity and temperature monitoring. Additionally, the control of the booster pump and the power supplies will be also integrated, to monitor the temperature variations inside the pipes remotely.

For the sake of safety, an interlock functionality will be implemented.

Chapter 5

Physics object reconstruction

To comprehend the data captured by the ATLAS detector, it is imperative to possess an accurate projection of the detector's outcomes. Monte Carlo (MC) programs find extensive utility in both experimental and theoretical high-energy physics domains, serving to replicate events or compute the total and differential cross-sections for specific physics phenomena. The alignment of experimental data with the MC simulation offers the means to assess the anticipations of the underlying theory. Additionally, this comparison aids in the interpretation of the observed data, facilitating the process of detector calibration.

The simulation process for the ATLAS experiment involves multiple stages [49]. It begins with *event generation*, utilizing a MC generator to simulate the initial proton-proton collision and prompt decays, followed by the *simulation* of the ATLAS detector's geometry and material characteristics. Subsequently, *digitization* takes place in transforming the hits generated by the core simulation into the detector's actual response. Finally, object *reconstruction* within the detector occurs. Notably, both the real data and the results from the simulation sequence utilize identical ATLAS trigger and reconstruction software packages.

In the present chapter, an overview of the MC generators used for the signal and background samples simulation is detailed, followed by several stages in the reconstruction and identification process of the different physics objects used in this analysis.

5.1 Monte Carlo Event Generation

5.1.1 Monte Carlo simulation

The concept of a perfect event generator remains elusive due to the inherent limitations in our understanding of various aspects of physics. Constructing an ideal event generator would only be feasible if our knowledge was already exhaustive, rendering experimental investigations redundant. Therefore, the pragmatic approach involves utilizing programs

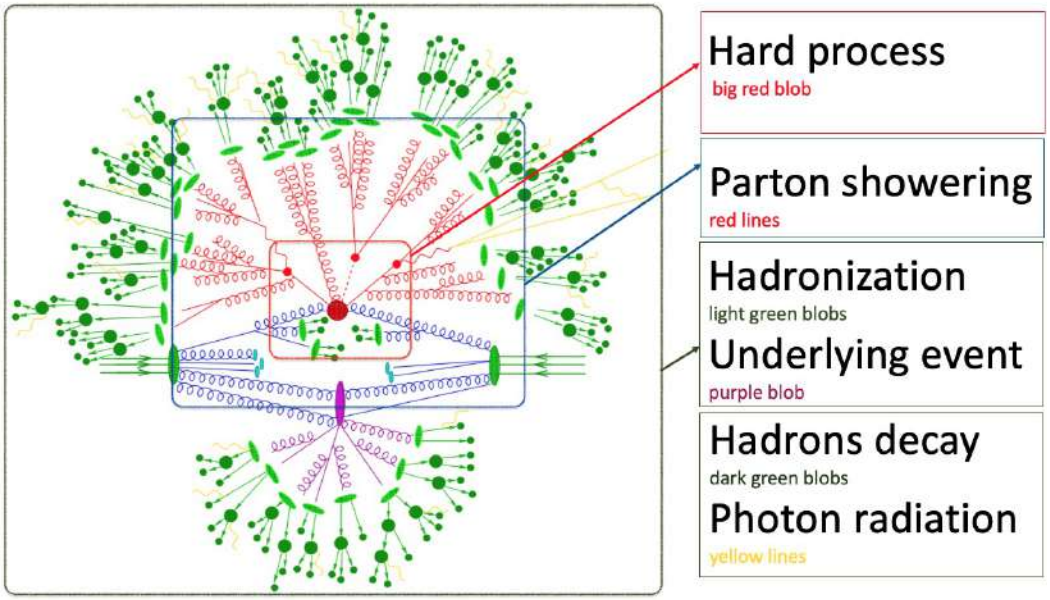

Figure 5.1: Pictorial representation of a $t\bar{t}h$ event as produced by an event generator. The decay of both top quarks and the Higgs boson is presented with small red blobs [50].

that exhibit reasonable agreement with the wealth of existing theoretical knowledge and experience while also providing plausible extrapolations to higher energy domains. Given the overarching goal of uncovering new dimensions in physics, it becomes essential to incorporate simulations that encompass a range of alternative scenarios.

The different stages that the event generation process goes through are sketched in Figure 5.1 and explained as follows:

- **Hard process:**

  The hard process highlights the interaction with the highest momentum between two partons originating from the incoming protons, leading to the generation of new massive particles. For example, the collision involving a pair of gluons from the incoming protons can yield a $t\bar{t}$ pair.
  The simulation procedure for the hard process necessitates the availability of Parton Distribution Functions (PDFs) as well as the partonic cross-section. The partonic cross-section symbolized as $\hat{\sigma}_{i,j\to X}$, for a final state X, can be computed from the matrix element, $\mathcal{M}_{i,j\to X}$, corresponding to a specific initial state $(i,\ j)$. This is achieved by integrating over the entire solid angle Ω, leading to the expression $\hat{\sigma}_{i,j\to X} = \int d\Omega |\mathcal{M}_{i,j\to X}|^2(\Omega, \mu_f^2)$. The matrix element $\mathcal{M}_{i,j\to X}$ corresponds to the scattering amplitude of the process and is derived from Feynman diagrams up to a certain order within the perturbative series in α_S. Including higher-order corrections is important for the precision and stability of the calculation. In specific cases, calculations exist up to the Next-to-Leading Order (NLO) or even the Next-to-Next-

to-Leading Order (NNLO).

- **Parton showering:**

  The progression denoted by the Parton Shower (PS) step encompasses the QCD evolution of both incoming and outgoing partons (quarks, gluons) engaged within the hard scatter procedure. Spanning from the hard process down to lower momentum scales, the parton shower characterizes the perturbative QCD Bremsstrahlung process. It effectively models the emission of radiation (Initial State Radiation (ISR) of the incoming partons, and the Final State Radiation (FSR) of the outgoing partons) at scales where perturbation theory remains applicable, eventually reaching a point beyond which the perturbative framework loses its validity.

- **Hadronisation**

  QCD transitions into a non-perturbative state in circumstances of extended distances (low energy). In this regime, the force of the strong interaction grows stronger, resulting in the confinement of quarks and gluons into colour-neutral hadrons. The process responsible for binding partons into these configurations is known as hadronization. To characterize this phenomenon, numerous phenomenological models have been formulated. These models can be broadly categorized into two groups: string models and cluster models. In string models [51], colour-linked pairs of partons are depicted as segments of strings, with quarks located at the string's endpoints and gluons visualized as bends in the string. In cluster models [52], following the Parton Shower, gluons are compelled to split into pairs of quark and anti-quark. Post-splitting, a collection of colour-neutral entities is constructed from these quark-anti-quark pairs.

- **Underlying event**

  The Underlying Event (UE) encompasses all additional interactions and phenomena occurring within a *pp* collision that remain distinct from the central hard scattering process. The UE shares colour connections with the hard process and encompasses partons that remain outside the purview of the hard-scatter event (termed beam remnants), radiation phenomena, and a further contribution stemming from Multiple Parton Interactions (MPI). In MPI, multiple pairs of partons engage in secondary hard or semi-hard interactions.
  Given the relatively low energy scale characterizing these processes, where non-perturbative QCD prevail, their simulation relies on phenomenological models. These models introduce various free parameters that require adjustment to achieve congruence with experimental data—a process known as *tuning*.

5.1.2 Monte Carlo generators

MC generators are categorised into two groups: multi-purpose generators, which execute all event generation steps, and ME generators. ME generators simulate the hard scattering process and necessitate integration with multi-purpose generators to facilitate the simulation of subsequent steps, such as PS, hadronisation, the decay of unstable hadrons, and UE.

The event generators utilized within this analysis are:

- **General Purpose Generators:**

  PYTHIA8 [53, 54]: operates as a multi-purpose event generator, encompassing multiple functionalities. The calculation of the hard scattering process is executed with leading-order (LO) accuracy in the context of QCD. The simulation of parton showers follows a transverse momentum-based ordering, while the hadronization process relies on the utilization of the Lund string model.

  SHERPA [55–59] employs a method outlined in [60] to combine fixed-order matrix elements, with QCD showers. The aim is to enhance its ability to accurately depict events that include a large number of isolated jets. This capability surpasses the performance achieved by Pythia. It seamlessly integrates with different external tools and easy to incorporate new processes. In such situations, SHERPA is frequently selected for simulating scenarios related to physics Beyond the Standard Model (BSM).

- **Specialized Purpose Generators:**

  POWHEG [61–65] executes ME calculations for a particular hard scattering process with (Next)Next-to-Leading Order (N(NLO)) accuracy in the perturbative QCD. Furthermore, it incorporates the POWHEG method to establish compatibility between the N(NLO) calculation and a parton-shower generator. This combination results in the generation of the most significant emissions as a component of the ME. Notably, this approach ensures the generation of events without any occurrence of negative weights.

  MADGRAPH5_AMC@NLO [66, 67] is an event generator for ME. It conducts the ME computations of a certain hard scatter process at NLO accuracy in perturbative QCD. The MC@NLO approach is used to match the created hard process with the PS. In the ME calculation, the overlap from the PS is subtracted. This approach generates a significant number of events with negative weights.

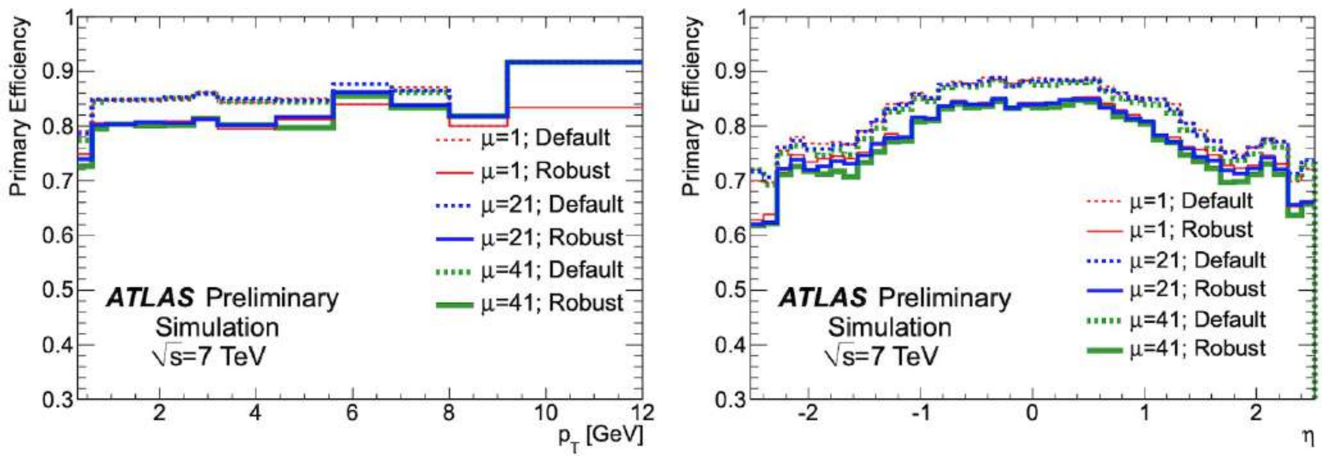

(a) (b)

Figure 5.2: The primary track reconstruction efficiency in minimum bias Monte Carlo samples containing exactly one interaction, and 21 or 41 interactions on average. The distributions are shown for tracks passing the default (dashed) and robust (solid) requirements [69].

5.2 Physics objects reconstruction and identification

In the computing system of ATLAS, the raw signals from the detector are converted into information that physicists can study in their analyses using a set of algorithms. Combining and piecing together those individual detector signals, the algorithms can reconstruct the physics objects (electrons, muons, photons, ...) and identify their type and kinematics for meaningful results.

The first basic step in the reconstruction and identification process is constructing tracks from both ID and MS hits in the case of muons, to provide an estimation of the objects' momentum and then matching this with clusters of energy deposits in the calorimeters.

.

5.2.1 Track and vertex reconstruction

Tracks are first reconstructed in the ID (Section 3.2.1) using a set of algorithms [68]. The inside-out algorithm starts from three points seeds in the SCT followed by a combinatorial Kalman Filter to add hits moving away from the interaction point (An iterative algorithm that provides the best estimation based on the projection of earlier and current measurements). Ambiguities in the track candidates are resolved, and tracks are extended into the TRT. The inside-out algorithm is the baseline algorithm designed for the efficient reconstruction of primary charged particles. To reconstruct the secondary particles, a back-tracking algorithm is performed to search for tracks starting from the TRT-reconstructed segments and extending them inwards by adding silicon hits [69]. Figure 5.2 illustrates the track reconstruction efficiency as a function of p_T and η.

5.2.2 Electrons and photons

5.2.2.1 Reconstruction

The electron reconstruction is based on three fundamental parts specifying the electron signature, by fitting a track using the Inner Detector information and matching it to the energy cluster in the EM Calorimeter:

- **The Seed-cluster reconstruction**
  A slide form window with a size of 3×5 in units of 0.025×0.025 in $\eta \times \phi$ [70] space is used to look for electron cluster seeds (according to the EM Calorimeter middle layer's granularity), as longitudinal towers with total cluster transverse energy above 2.5 GeV. Around the seeds, the clusters are formed using a specific algorithm responsible for duplicate removal. Depending on the cluster position in the calorimeter, an extended window is used to reconstruct the kinematics of the cluster.

- **Track reconstruction**
  The track reconstruction is performed in 2 steps:

  → Pattern recognition using pion hypothesis [71] for handling the energy loss in the detector material. The algorithm of pattern recognition allows for 30% energy loss at each interaction of the track with the material to account for possible bremsstrahlung.

  → Pattern recognition using electron hypothesis occurs when a track seed with $p_T > 1$ GeV can not be extended to a full track of at least seven hits using the pion hypothesis.

  The tracks are then fit with one of the hypotheses using the ATLAS Global χ^2 Track Filter according to which hypothesis is used in the pattern recognition.

- **Electron specific track fit**
  The distance in η and ϕ between the position of the particle and the track is used to match the obtained tracks to EM clusters loosely after extrapolation in the calorimeter middle layer and the cluster barycentre.

5.2.2.2 Identification

The candidate electrons built by the reconstruction algorithm are not all meant to be prompt ones and could be considered mainly as signal objects; other objects treated as background are also results of the reconstruction process and could include hadronic jets, electrons from photon conversions, Dalitz decays and electrons from semileptonic heavy-flavour hadron decay.

To discriminate between the signal and the background electrons and reject as much as possible the backgrounds while keeping the efficiency high for prompt electrons, the identification algorithms use combined discriminating variables of selections with various rejecting powers of the backgrounds.

Properties of the tracks in the ID, the matching between the tracks and the energy clusters, and variables describing the longitudinal and lateral shapes of the EM showers are all used as discrimination against background objects.

The common selections used in the identification, so-called **Cut-based** selections, are:

- *Loose* **cuts** These cuts consist of simple selections related basically to limited information from the calorimeters. They provide excellent efficiency of the identification but low rejection of the background. This set of cuts is applied to the hadronic leak and shower-shape variables from the middle layer of the EM calorimeter.
- *Medium* **cuts** By adding cuts on the strips in the first layer of the EM calorimeter and on the tracking variables, the quality of the identification is improved and the jet rejection is increased by a factor of 3 to 4 compared to the *Loose* cuts while the efficiency is reduced by 10%.
- *Tight* **cuts** These cuts require the usage of all the particle-identification tools. Several variables are applied by the Tight cuts such as the number of vertexing-layer hits, the number of hits in TRT, and the ratio of high-threshold hits to the number of hits in TRT, etc [72]. In general, this set of cuts yields the highest isolated electron identification and the highest rejection against jets.

Electrons considered in the $S \rightarrow Z_d Z_d \rightarrow 4l$ analysis are required to pass the *Loose* working point since it requires at least two hits in the pixel detector, seven hits total in the pixel, and silicon-strip detectors and one in the inner-most pixel layer. More details will be given in Section 6.

The **Likelihood-based** cuts, in contrast, is the one used in electron identification. It is a multivariate technique (MVA) that has been developed and implemented in the ATLAS software. It simultaneously evaluates several properties of the electron candidates when making a selection decision. A discriminant $d_{\mathcal{L}}$ is formed from the likelihood of a reconstructed electron whether it originates from a signal or background. The LH selection makes use of the probability density functions (PDFs) of the signal $\mathcal{L}_S$ and the background $\mathcal{L}_B$ that are obtained from data and treated as uncorrelated.
The LH discriminant $d_{\mathcal{L}}$ is calculated as:

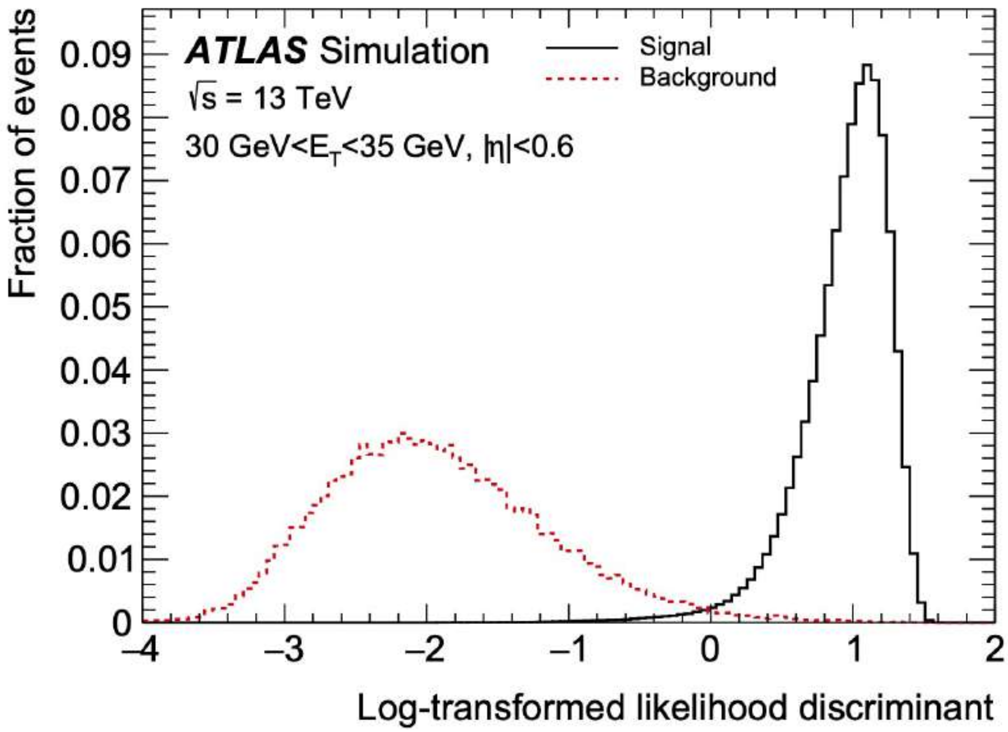

Figure 5.3: The transformed LH-based identification discriminant $d'_{\mathcal{L}}$ for reconstructed electron candidates with good quality tracks with 30 GeV $< E_T <$ 35 GeV and $|\eta| < 0.6$, where the signal is for prompt electrons in a $Z \rightarrow ee$ process [73].

$$d_{\mathcal{L}} = \frac{\mathcal{L}_S}{\mathcal{L}_S + \mathcal{L}_B}, \text{ with: } \mathcal{L}_{S(B)}(\overrightarrow{x}) = \prod_{i=1}^{n} \mathcal{P}_{S(B),i}(x_i). \tag{5.1}$$

For both the signal and the background, the PDFs take the values of $\mathcal{P}_{S,i}(x_i)$ and $\mathcal{P}_{B,i}(x_i)$ respectively for the i^{th} variable evaluated at value x_i.

The electron likelihood identification imposes some other requirements besides the likelihood discriminant selection, with significant discriminating power.

The discriminant $d_{\mathcal{L}}$ has a sharp peak at unity (zero) for signal (background); this sharp peak makes it inconvenient to select operating points as it would require extremely fine binning. An inverse sigmoid function is used to transform the distribution of the discriminant:

$$d'_{\mathcal{L}} = -\tau^{-1} ln(d_{\mathcal{L}}^{-1} - 1), \tag{5.2}$$

where the parameter τ takes the value 15 [74].

Figure 5.3 illustrates an example of the transformed discriminant distribution for prompt electrons from the Z boson decays and for background.

Quite similar to the cut-based selections, there are four values of the LH discriminant used to define four operating points (working points) which are referred to as `Loose`, `Medium`, `Tight`, and `VeryTight`. For example, the efficiencies for identifying a prompt electron with $E_T = 40$ GeV are 93%, 88%, and 80% for the `Loose`, `Medium`, and `Tight` working points, respectively, as shown in Figure 5.4.

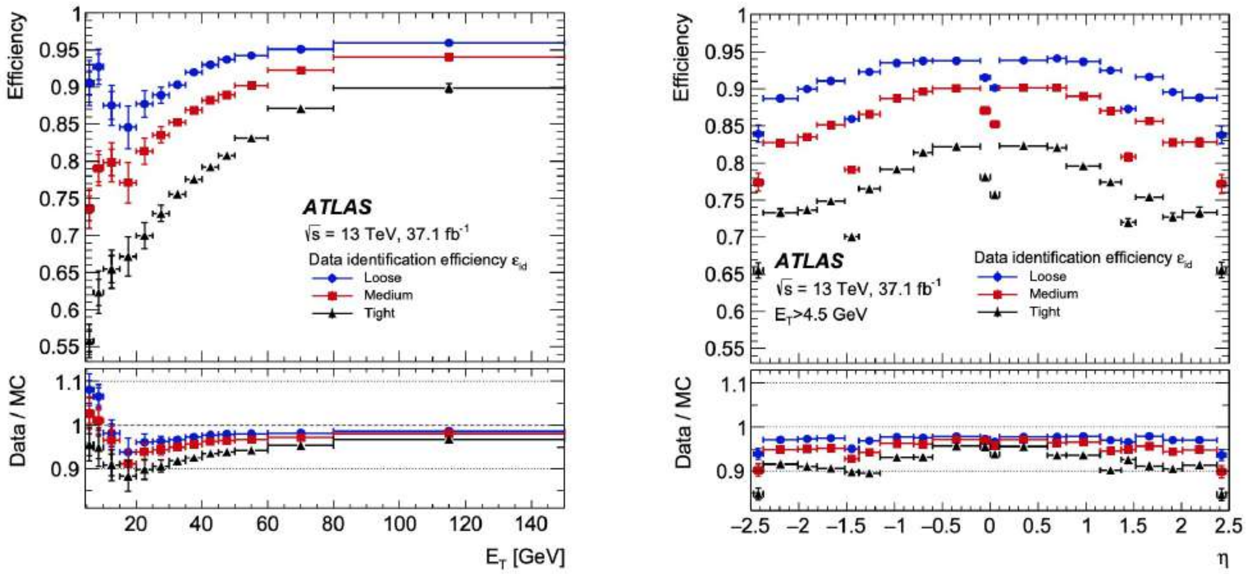

(a) (b)

Figure 5.4: The electron identification efficiency in $Z \to e^+e^-$ events as function of E_T (a) and as function of η (b) for the three Working Points, (WPs): `Loose`, `Medium`, and `Tight` [73].

5.2.2.3 Photons

Photons originating from collisions within the LHC are detected and reconstructed similarly to electrons, utilizing the same framework. These photons primarily fall into two main categories: *converted* and *unconverted*. Converted photons refer to those that interact with material within the Inner Detector (ID), giving rise to an electron-positron pair. When these charged particles are distinguishable, they create a *conversion vertex*. Identification of the photon and its trajectory is achieved through matching a supercluster [70] to a conversion vertex. On the other hand, unconverted photons do not interact with the ID, manifesting solely as energy deposits in the calorimeters. These are distinguished through superclusters lacking matching tracks or conversion vertices.

Similarly to electrons, photons undergo identification, and isolation procedures, employing distinct algorithms and WPs. Given the resemblances in their signatures, it is crucial to resolve any ambiguities that may arise between candidates resembling both electrons and photons.

5.2.3 Muons

5.2.3.1 Reconstruction

The reconstruction of the muons depends on different parameters such as the p_T and η values, as well as the detector involved in the identification. The muon is firstly independently reconstructed in the ID and the MS (Section 3.2.3) detectors and then uses the energy deposit information left in the calorimeters. Four types of muons can be selected depending on which detector information is used:

- **Combined muons (CB)**: After reconstructing tracks independently in the ID and the MS detectors, combined track information is used and the hits from the ID and the MS are fitted.
- **Segment-tagged muons (ST)**: are defined when an ID muon track is matched to a local track segment in the MDT or CSC layer of the MS detector. This algorithm looks for muons with low p_T, that are unable to reach the outer MDT layer due to the magnetic field.
- **Calorimeter-tagged muons (CT)**: When an ID track is matched to energy deposits in the calorimeter and is compatible with the one left from a minimum ionizing particle, it is classified as a muon. This technique is used to identify muon in the pseudo-rapidity range $\eta < 0.1$, where the MS is not efficient due to geometrical vetoes.
- **Extrapolated (Standalone) muons (ME)**: are identified when reconstructing their tracks from only the MS detector by applying a compatibility requirement with the interaction point (IP). These muons are used to recover the acceptance in the region $2.5 < |\eta| < 2.7$, where the ID cannot work.

5.2.3.2 Identification

The ratio q/p or so-called significance is one of the criteria used to select muons with the highest possible efficiency and purity. It is utilized to perform discrimination of good muons from other muons, where q and p are the charge and the momentum of muons respectively, and the ratio is defined as:

$$(q/p)_{significance} = \frac{|q/p|_{MS} - |q/p|_{ID}}{\sqrt{\sigma^2_{q/p_{ID}} + \sigma^2_{q/p_{MS}}}}, \tag{5.3}$$

where $|q/p|_{ID}$ is the charge-to-momentum-ratio measured by the ID and $|q/p|_{MS}$ is the same ratio measured in the MS. $\sigma_{q/p}$ is the sum in quadrature of the corresponding uncertainties.

Along with the significance discriminant, there are other variables used for combined muons identification:

- $\rho^{'}$ is the absolute value of the difference between the p_T measured in the ID and MS, normalized by the p_T of the combined track.

$$\rho^{'} = \frac{|p_{T,ID} - p_{T,MS}|}{p_{T,CB}} \tag{5.4}$$

- χ^2 of the combined track fit.

Besides these selection criteria, different requirements are used depending on different physics analyses such as:

- `Medium`: This WP includes only the CB and ME muons requiring three hits on two precision MDT and CSC layers. It is the most common selection used in ATLAS physics analyses.
- `Loose`: The CB and ME muons that passed the `Medium` selection are included; ST and CT muons are restricted in the region $|\eta| < 0.1$ since it's not covered by the MS. This selection is used to maximise the reconstruction efficiency of all muons and all muons types are included.
- `Tight`: To increase the purity of muons, the `Tight` WP is used considering only the CB muons that passed the `Medium` requirements. To reject, as many as possible the backgrounds, a cut on the q/p variable is applied as well.
- $\mathtt{High-p_T}$: Only the CB muons, passing the `Medium` requirements and having hits on the three precision layers, are the only ones considered. This selection increases the resolution of the muons' momentum with $p_T > 200$ GeV.

Figure 5.5 shows the muon identification efficiency as a function of η (left) and p_T (right), for transverse momenta $p_T > 10$ GeV using the $t\bar{t}$ events reconstructed from pp collisions at $\sqrt{s} = 13$ TeV, recorded at the LHC in 2015-2018.

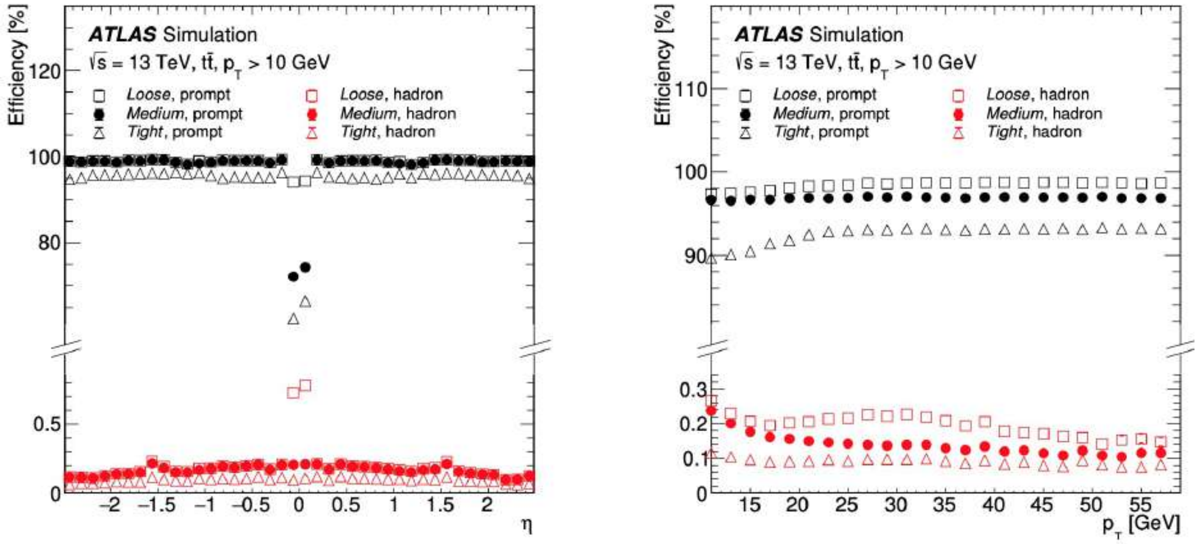

Figure 5.5: Muon-identification efficiency, as a function of η (left) and p_T (right), for three different selections (`Loose`, `Medium`, and `Tight`) WPs requirements in simulated $t\bar{t}$ events, shown separately for prompt muons and muons from light hadron decays [75].

5.2.4 Jets

Quarks are constrained to exist solely in configurations that maintain colour singlet combinations due to QCD confinement that imposes limitations on the free propagation of these individual quarks. They are often generated in LHC *pp* collisions, and their confinement gives rise to showers of secondary quarks and gluons. These showers subsequently undergo hadronization, culminating in the creation of color-neutral hadrons. Mainly, this involves pions, with some contribution from kaons and light baryons.
These high-momentum showers are subjected to relativistic boosting, resulting in the formation of tightly clustered *jets*. These jets deposit their energy within the calorimeters and generate tracks within the ID. Employing algorithms, the information collected from these detectors is combined to reconstruct both the energy and trajectory of the centrally-produced particle.

5.2.4.1 Reconstruction

For the jets reconstruction, a clustering algorithm is employed, utilizing four-vectors derived from energy deposits and tracks associated with charged particles within a specific topology. Within the ATLAS experiment, this algorithm incorporates signals from connected calorimeter cells called topo-clusters. The responsible algorithm for generating these topo-clusters analyzes the spatial distribution of energy deposits across neighbouring calorimeter cells in three dimensions. A comprehensive explanation of this process is available in reference [76].

The critical determinant for cluster formation is the cell signal significance, represented as ς_{cell}^{EM}. This significance is established by comparing the amplitude of the cell signal to the expected noise level of the cell:

$$\varsigma_{cell}^{EM} = \frac{E_{cell}^{EM}}{\sigma_{noise,cell}^{EM}}. \tag{5.5}$$

Several algorithms are available for reconstructing jets from fractional energy distributions within calorimeters. The anti-k_t algorithm [77] is used for jet reconstruction in the context of the ATLAS experiment. This algorithm is based on several inputs, including groups of energy clusters derived from calorimeters and distances (d_{ij}) estimated between jet candidates i and j. In addition, for each jet candidate i, a distance (d_{iB}) relative to the beam is calculated. These distances, d_{ij} and d_{iB}, are precisely defined as follows:

$$d_{ij} = min(\frac{1}{p_{T,i}^2}, \frac{1}{p_{T,j}^2})\frac{(\eta_i - \eta_j)^2 + (\phi_i - \phi_j)^2}{R^2},\ d_{iB} = p_{T,i}^{-2} \tag{5.6}$$

in terms of the transverse momenta p_T, pseudo-rapidities, and azimuthal angles ϕ. R is an adjustable algorithm parameter that regulates the size of the output jet.

5.2.4.2 Pileup jet tagging

When several proton-proton collisions occur inside a single event in high-energy physics, there might be many interaction vertices from which particles originate. These vertices can be linked to the original collision of interest and pileup collisions. Pileup particles may contaminate signals of interest, such as those originating from the primary collision.

The jet-vertex fraction (JVF) [78] requirement quantifies the amount of a jet's energy coming from a specific vertex. It estimates the fraction of a jet's energy associated with the primary vertex (the vertex of interest in the collision) vs. the pileup vertices. This fraction helps determine the purity of a jet's energy with respect to the primary interaction:

$$JVF = \frac{\sum_k p_T^{trk_k}(PV_0)}{\sum_l p_T^{trk_l}(PV_0) + \sum_{n\geq 1}\sum_l p_T^{trk_l}(PV_n)}, \tag{5.7}$$

considering PV_0 the hard-scatter vertex and PV_j, with $j \geq 1$, the primary vertices due to pileup interactions in the same bunch crossing. k runs over all tracks originating from PV_0, l runs over all primary vertices in the event and n over all tracks originating from PV_n. Tracks with p_T greater than 500 MeV are the only ones considered in the calculation of JVF.

There are other variables used to distinguish whether the jets are originating from the primary vertex or pileup interaction, such as the improved variables for pileup jets, $corrJVF$ and R_{pT} and Jet Vertex Tagger (JVT) as detailed in reference [79].

5.2.4.3 Heavy-flavour jet tagging

Flavour tagging is an important tool for precisely distinguishing and classifying jets arising from light quarks or gluons (referred to as light-flavour jets) and those originating from heavy quarks, notably c- or b-jets. The characteristics of heavy-flavoured hadrons, such as their extended lives, which result in the development of displaced (or secondary) vertices, as well as their large impact parameters and mass, differentiate these types of jets. As a result, good flavour tagging implementation needs rapid and trustworthy track reconstruction, as well as exact vertex position measurements.

To distinguish between b-, c-, and light-flavor jets, a variety of specialised algorithms for analysing certain discriminating qualities have been developed. These include IP2D and IP3D [80], which evaluate the relevance of track d_0 and z_0 and their correlations. There's also SV1 [81], which reconstructs variables to reveal the presence of both single and inclusive secondary vertices, and JetFitter [82], which can rebuild the whole decay chain of a b-hadron.

The results of these complementary algorithms are then merged into high-level taggers to generate more versatile and robust tools. The MV2 algorithm [80], which is based on a Boosted Decision Tree (BDT), was frequently used during Run2. The DL1 algorithm [80], based on a neural network (NN) architecture, is a more recent innovation. In addition, in recent years, RNNIP, a new low-level impact parameter-based tagger, has been deployed. Using a Recurrent Neural Network (RNN) technique, this tagger capitalises on track correlations. High-level tagger variations that also utilise RNNIP output have been introduced, with DL1r now acting as the ATLAS experiment's recommended flavour tagging algorithm.

5.2.5 Taus

Taus possess a distinctive property not shared by other leptons: their mass is sufficient to make them decay into hadrons. The reconstruction of these hadronic decays can be accomplished through two distinct methods.

In the track-based approach, tracks are required to have a minimum of two hits in the pixel detector and IBL, with a total of seven hits mandated when considering the SCT. Additionally, these tracks must exhibit a transverse momentum $p_T > 1$ GeV and be confined within a cone region defined by $\Delta R < 0.2$.

Conversely, the jet-based strategy involves the reconstruction of seeds as jets using topoclusters with energies $E_T > 10$ GeV within the $|\eta| < 2.5$ region. If tau candidates fall within $1.37 < |\eta| < 1.52$, they are not considered. In cases where topojets are present in the event, they are matched to seed tracks, and a Tau candidate is considered to possess two valid seeds.

The determination of the Tau vertex relies on identifying the candidate track vertex that contributes the most significant proportion of momentum from tracks associated with the jet ($\Delta R < 0.2$). Additionally, specific criteria necessitate that the track's shortest distance to the tau vertex satisfies $d_0 < 1.0$ mm in the transverse plane and $\Delta z_0 sin(\theta) < 1.5$ mm in the longitudinal plane.

5.2.6 Missing transverse energy

In a proton-proton collision, the Hard Scattering (HS) involves quarks and gluons, and their momenta, determined by parton densities, are inherently random. The conservation law mandates that the momentum of the proton-proton system remains constant, resulting in zero transverse momentum. Consequently, the sum of transverse momenta from the collision products must also be zero. Any non-zero measured transverse momentum implies the presence of an undetected particle.

The existence of non-zero missing transverse energy (MET) signals potential particle production weakly interacting with the detector. MET acts as an experimental proxy to estimate transverse momentum for undetected particles, posing a reconstruction challenge across all detector subsystems. Accurate reconstruction of detectable particles from the hard interaction is crucial.

The measurement of MET in the detector is vital for physics analyses, calculating the imbalance in total transverse momentum post-collision. This imbalance arises from particles undetected in ATLAS. While neutrinos are the undetected particles in the Standard Model, other models introduce new particles beyond the SM, escaping the ATLAS detector undetected, potentially contributing to missing transverse energy.

The quantity describing missing transverse momentum is termed missing transverse momentum (MET), with its magnitude referred to as missing transverse energy (E^T_{miss}). E^T_{miss} is computed based on calibrated objects, and its x and y components are determined by the magnitudes along the x and y axes of various contributions.

$$E^{miss}_{x(y)} = E^{miss,\mu}_{x(y)} + E^{miss,e}_{x(y)} + E^{miss,\gamma}_{x(y)} + E^{miss,\tau}_{x(y)} + E^{miss,jets}_{x(y)} + E^{miss,soft}_{x(y)}. \quad (5.8)$$

Each term in the calculation corresponds to the negative vectorial sum of transverse momenta from both tracks and energy deposits. These energy deposits and tracks are subsequently matched to physics objects, encompassing all reconstructed and calibrated entities. The priority order for object assignment is as follows: electrons, photons, hadronically decaying τ-leptons, jets, and muons, collectively known as the hard term. To mitigate the risk of double-counting detector signals, an ambiguity-solving procedure is implemented [83]. The quantity $E_{(x,y)}^{miss,,soft}$, referred to as the soft term, encompasses all signals not associated with any of the previously identified objects.

$$E_{x(y)}^{miss} = - \sum_{i \in \{hard\ objects\}} p_{x(y),i} - \sum_{j \in \{soft\ objects\}} p_{x(y),j}. \tag{5.9}$$

Then it is easy to construct other widely used variables based on Equation 5.9:

$$\begin{aligned} E_T^{miss} &= |\overrightarrow{E}_T^{miss}| \\ &= \sqrt{(E_x^{miss})^2 + (E_y^{miss})^2}. \end{aligned} \tag{5.10}$$

$$\phi^{miss} = tan^{-1}\left(\frac{E_y^{miss}}{E_x^{miss}}\right). \tag{5.11}$$

The quantity E_T^{miss} is inherently non-negative by definition, with ϕ^{miss} denoting the azimuthal angle that characterizes its direction. The determination of E_T^{miss} is performed both in the trigger and offline computation [83].

For the assessment of the soft term, one can consider ID tracks or topo-clusters in the calorimeter. ATLAS employs a track soft term (TST), designed to be insensitive to pileup effects since it exclusively considers tracks associated with the hard-scattering (HS) vertex. However, it is noteworthy that TST does not account for the presence of neutral particles.

5.2.6.1 Reconstruction of the Missing Transverse Momentum

Reconstructing the missing transverse momentum (E_T^{miss}) for an event at ATLAS involves two primary contributions. The first contribution utilizes signals from physics hard objects, consisting of reconstructed electrons, photons, τ-leptons, jets, and muon particles. The second contribution arises from soft-event signals, comprising reconstructed charged particle tracks not associated with hard objects. Terms associated with physics objects must pass specific object selection criteria.

Electrons are reconstructed based on their shower shapes in the ECAL calorimeter, matched to ID tracks [84]. Electrons included in the E_T^{miss} calculation must be identified within the range of $|\eta| < 2.47$, avoiding the transition region between the barrel and end-cap EM calorimeters ($1.37 < |\eta| < 1.52$). They are calibrated at the EM scale [85] and must satisfy the "Medium" likelihood and "Loose" isolation criteria [84] with $p_T > 10$ GeV.

The identification and reconstruction of photons rely on electromagnetic showers in the calorimeters [86]. Photons are chosen and calibrated using the "Tight" selection criteria discussed in [87]. Photons with $p_T > 25$ GeV, $|\eta| < 1.37$, or $1.52 < |\eta| < 2.37$ are utilized.

Hadronically decaying τ leptons with $p_T > 20$ GeV and $|\eta| < 1.37$ or $1.52 < |\eta| < 2.47$ are considered, satisfying the "Medium" quality selection [88]. Additionally, a τ-lepton not meeting the criteria may contribute to E_T^{miss} if it satisfies the jet selection criteria.

Muon candidates are reconstructed within $|\eta| < 2.5$ using an association of MS and ID tracks. Outside the ID area coverage, muons are identified in the region of $2.5 < |\eta| < 2.7$ from a track fit to MS track segments alone. Medium muons with $p_T > 10$ GeV in $|\eta| < 2.5$ contribute to the E_T^{miss} terms. Jets are reconstructed using the anti-k_T algorithm with radius $R = 0.4$, incorporating electromagnetic, jet energy scale, and pile-up corrections. The $E_T^{miss,soft}$ term is constructed from tracks with $p_T > 400$ MeV and $|\eta| < 2.5$, along with additional fit quality criteria. Vertices are constructed from at least two tracks passing selections on the transverse (longitudinal) impact parameter $|d_0| < 1.5$ mm ($|z_0 sin\theta| < 1.5$ mm) relative to the vertex candidate [83].

The E^T_{miss} scale and resolution are calibrated using events with $Z \rightarrow \mu^+\mu$, where the decay of the Z boson into two muons serves as a genuine E_T^{miss} source. In this context, muons are considered minimum ionizing particles (MIPs), leaving a small fraction of their energy in the calorimeter (ranging from 100 MeV/c to 100 GeV/c). A di-muon decay provides an ideal source of no genuine missing transverse momentum.

The two muons produced by the Z boson must have opposite electric charges due to charge conservation in the decay process. The leading muon is required to have a p_T greater than 25 GeV, while the sub-leading muon must have a $p_T > 20$ GeV. Muon identification relies on quality requirements assessing the likelihood of an object being a muon based on variables such as the χ^2 value of the fit and the p_T difference between inner detector and muon spectrometer measurements. The isolation criterion mandates the muon to be isolated from other objects like jets. Both muons must be of "Medium" quality within $|\eta| < 2.5$ and pass isolation requirements [83]. The invariant mass of the Z-boson can be constructed from the four momenta of the two muons found in the events.

The performance of the modeling in the simulation of the E_T^{miss} magnitude calculation was tested in events with and without genuine E_T^{miss}, as depicted in Figure 5.6 and Figures 5.7.

5.2.6.2 E_T^{miss} performance

The performance of E_T^{miss} has been meticulously assessed using $Z \rightarrow \ell\ell$ events, representing a pristine event signature with a relatively large cross-section, owing to the absence of genuine E_T^{miss}. Within each event topology featuring $Z \rightarrow \ell\ell$ decay, an axis in the transverse plane is defined such that the E_T^{miss} component along this axis becomes sensitive

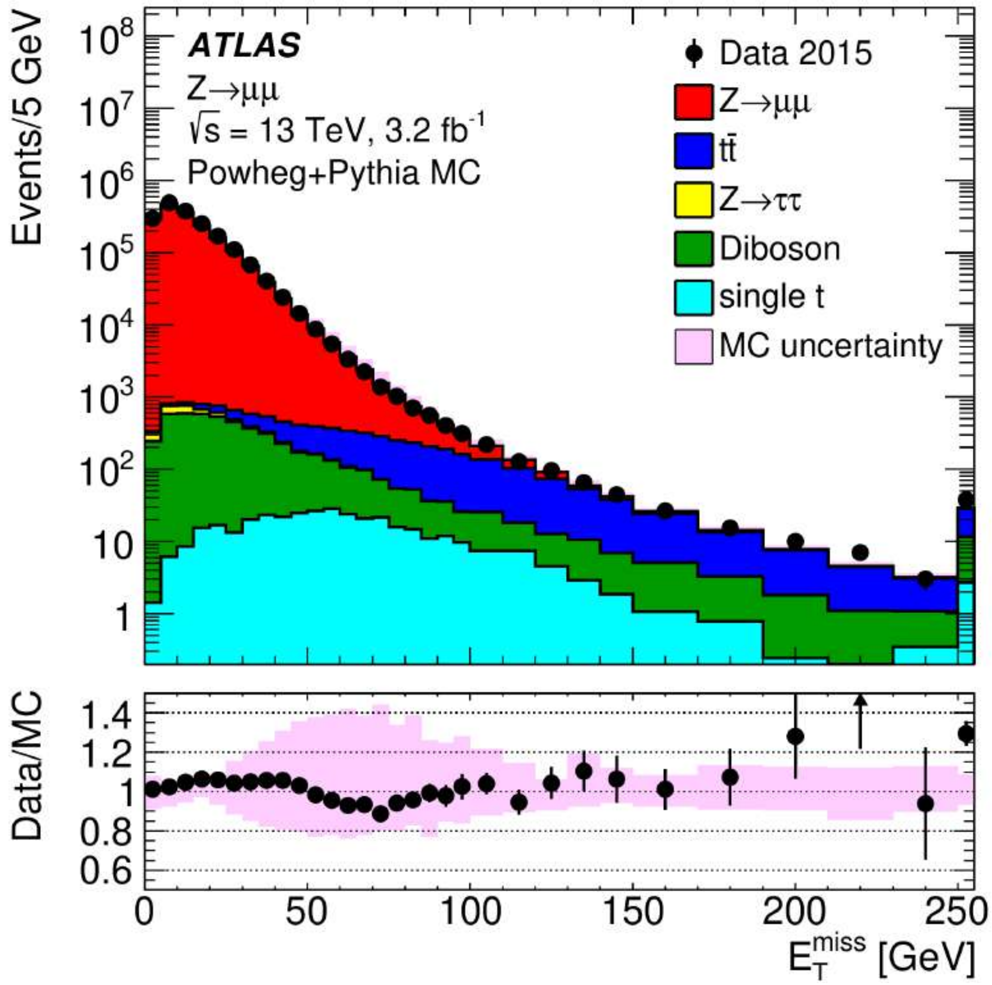

Figure 5.6: Comparison of the E_T^{miss} distribution in $Z + jets$ events where no genuine E_T^{miss} is expected from the non-reconstruction of the neutrino [83].

to detector resolution and biases. The vector $\boldsymbol{E}_T^{miss}$ is projected onto the reconstructed flight direction of the Z boson ($\boldsymbol{A}_Z$), effectively reconstructing the motion direction of the Z boson.

The mean value of the projection of $\boldsymbol{E}_T^{miss}$ onto the longitudinal axis, denoted as $\langle \boldsymbol{E}_T^{miss}.\boldsymbol{A}_Z \rangle$, serves as a gauge for the E_T^{miss} scale, given its sensitivity to the balance between the leptons and the hadronic recoil. In events devoid of jets, the anticipated value of this quantity is 0. Values below 0 are expected if the estimation of hadronic recoiling activity is underestimated. Figure 5.8 illustrates the variation of $\langle \boldsymbol{E}_T^{miss}.\boldsymbol{A}_Z \rangle$ with p_T^Z. These mean values serve as a diagnostic tool to validate E_T^{miss} reconstruction algorithms.

In an ideal scenario where leptons perfectly balance the hadronic recoil, regardless of the net momentum of the lepton system, $\langle \boldsymbol{E}_T^{miss}.\boldsymbol{A}_Z \rangle$ would be zero, independent of p_T^Z. Instead, $\langle \boldsymbol{E}_T^{miss}.\boldsymbol{A}_Z \rangle$ exhibits a slight bias, reasonably replicated by the Monte Carlo

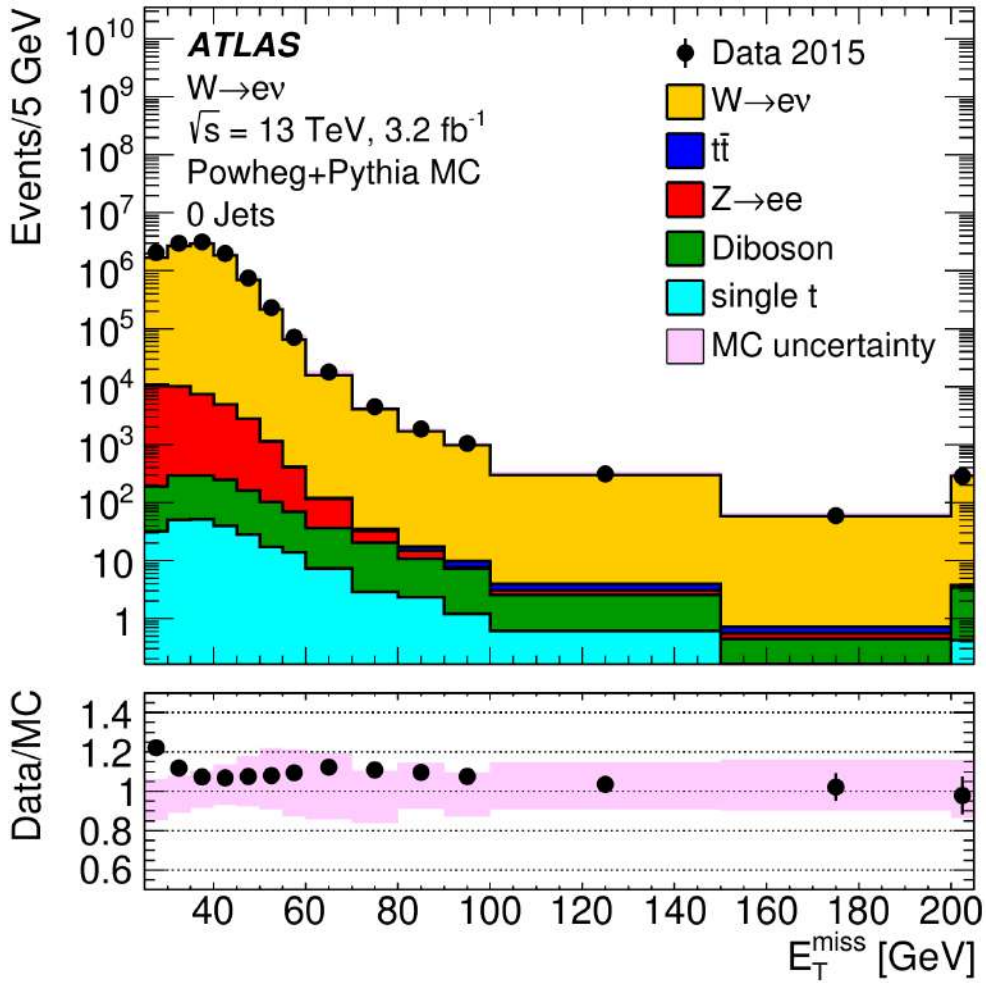

Figure 5.7: Comparison of the E_T^{miss} distribution in $W + jets$ events, where genuine E_T^{miss} is expected from the non-reconstruction of the neutrino [83].

(MC) simulation. At low values, the presence of a missing neutral component in the soft term leads to an underestimation of the hadronic recoil activity. As p_T increases, the jet term in the E_T^{miss} definition tends to dominate, resulting in a noticeable flat offset. Data and MC simulation exhibit good agreement within uncertainties.

A more rigorous quantitative assessment of E_T^{miss} performance, can be achieved through an examination of the (E_x^{miss}, E_y^{miss}) resolutions as a function of the scalar sum of transverse energies ($\sum E_T$). The resolution is quantified by the root mean square (RMS) of the combined distribution of E_x^{miss} and E_y^{miss} in bins of $\sum E_T$. This evaluation is conducted using $Z \to \mu\mu$ events, where E_T^{miss} is expected to be zero. Figure 5.9 illustrates the RMS of the E_x^{miss} and E_y^{miss} components of E_T^{miss} as a function of $\sum E_T$, demonstrating that the resolution is predominantly influenced by the measurement of the two muons at low $\sum E_T$ values, while the logarithmic behaviour above ~180 GeV is associated with Jet Energy Resolution.

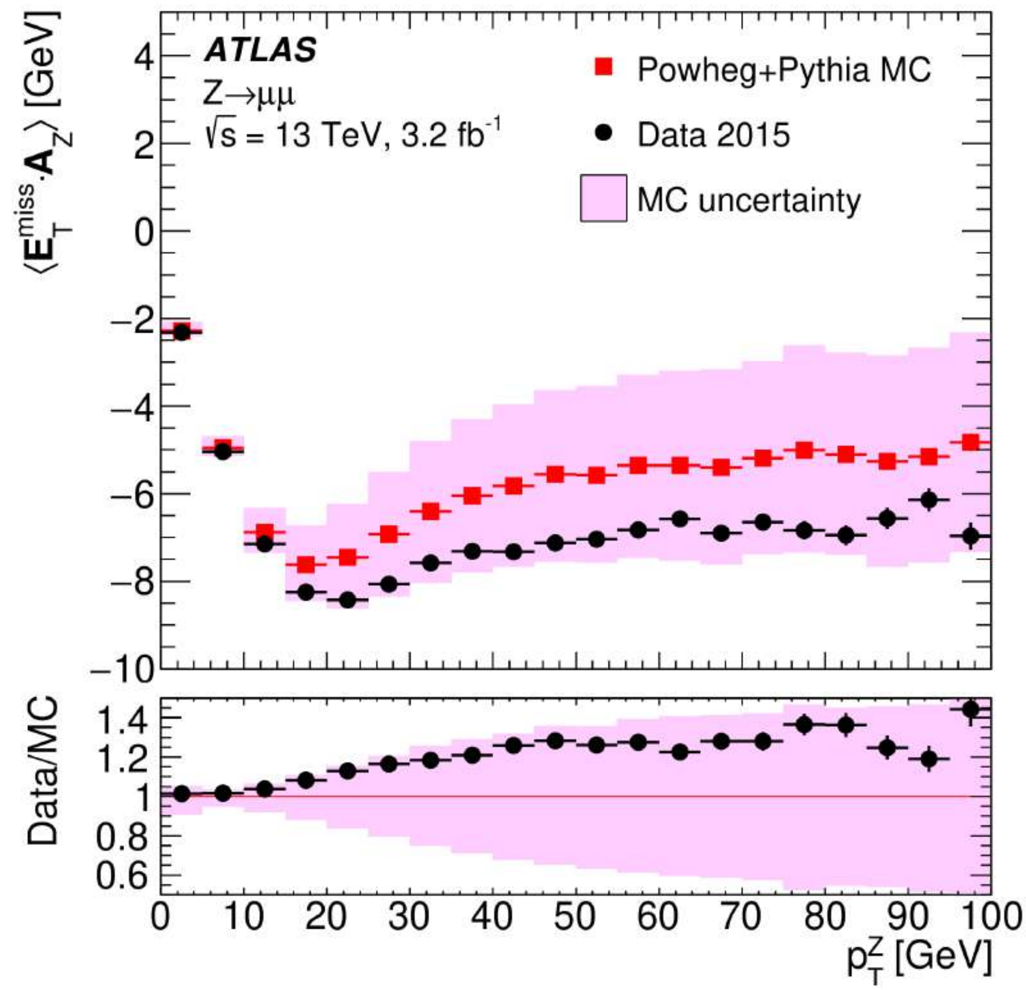

Figure 5.8: Comparison of the average projection of E_T^{miss} on the flight direction of the Z boson in $Z \to \mu\mu + jets$ events [83].

For any analysis utilizing E_T^{miss}, a crucial requirement is the ability to assess the systematic uncertainty on the E_T^{miss} scale. The E_T^{miss} in this chapter is defined as the sum of various terms corresponding to different types of reconstructed objects. The uncertainty associated with each individual term can be determined based on the knowledge of the reconstructed objects used in its construction, and this uncertainty is then propagated to E_T^{miss}. The overall systematic uncertainty on the E_T^{miss} scale is computed by combining the uncertainties on each term. Consequently, systematic uncertainties on E_T^{miss} reconstruction are provided for both scale and resolution measurements. The hard term uncertainty component is propagated from the objects used in its definition, while soft-term systematic uncertainties are evaluated from data and MC simulation by examining $E_T^{miss,soft}$ components parallel and perpendicular to the reconstructed direction of the hard term [83]. During my qualification task project, I delved extensively into the study of E_T^{miss} performance.

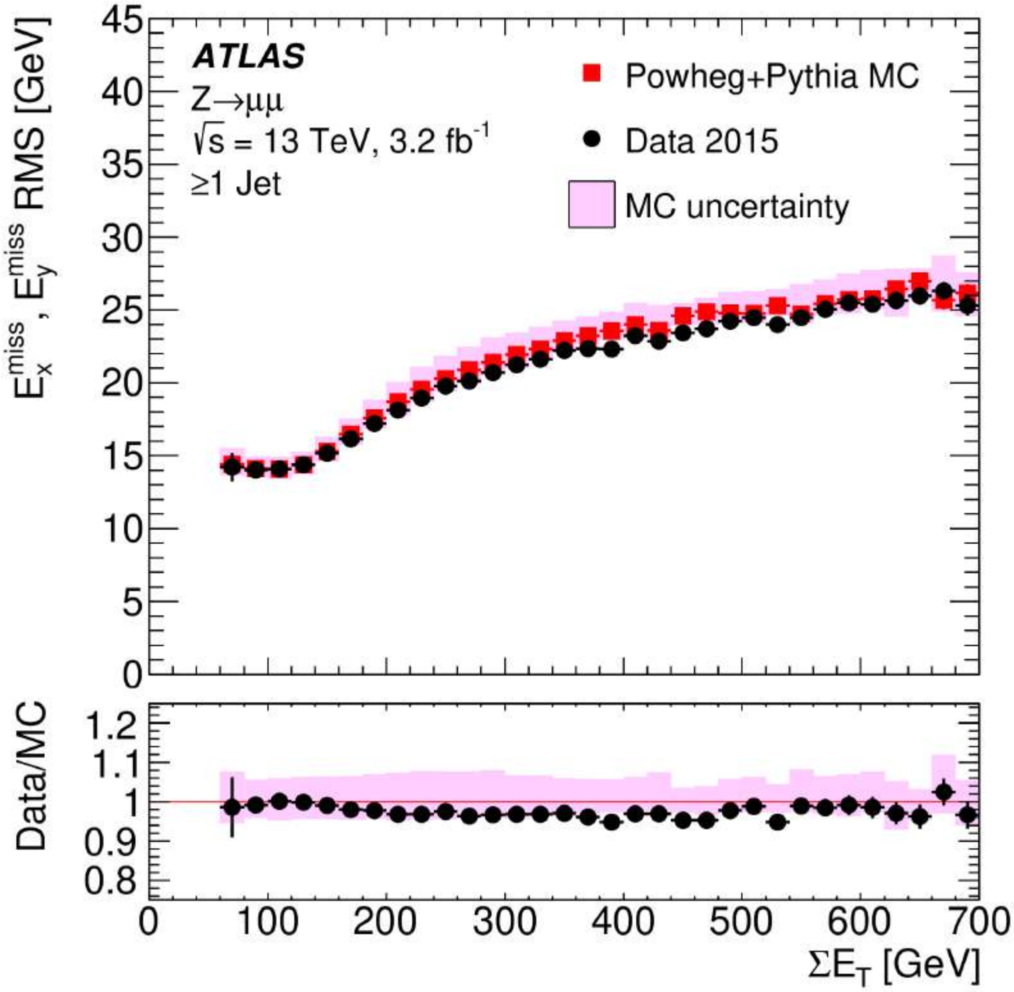

Figure 5.9: Resolution on the measurement of E_T^{miss} (E_x^{miss}, E_y^{miss}) components as measured in data and obtained in MC simulation in $Z \rightarrow \mu\mu + jets$ events [83].

Chapter 6

$S \rightarrow Z_d Z_d \rightarrow 4l$ search

As mentioned in Chapter 2, in the present thesis, a search for a new scalar boson S is conducted, with mass distinct from the 125 GeV Higgs boson ($m_S \in [15, 115[\cup]130, 800]$ GeV) decaying into four leptons. This decay is presumed to occur via an intermediate state containing two Z-dark bosons. The benchmark model adopted is the HAHM as illustrated in Figure 2.8b.

In this chapter, the object and event selections will be detailed, and the background estimation, validation regions as well as signal region selection will be discussed. Full Run2 results are shown at the end using pp collision events collected in 2015-2018 at the LHC at $\sqrt{s} = 13$ TeV for an integrated luminosity of $139 fb^{-1}$.

6.1 Object and Event selection

The event selection passes through several steps defined as cutflow, where a sequence of requirements is applied to the event variables in the region of interest.

6.1.1 Event preselection

The preselected events should have passed some basic requirements such as:

- Good Run Lists (GRL).
- Cleaning (not have `LArError`, `TileError`, `SCTError`, or `CoreError`).
- Firing at least one of the triggers listed in Table 6.1.
- Having at least one primary vertex reconstructed with two or more associated tracks with $p_T > 400$ MeV.
- Having at least four leptons.

ℓ	Trigger name	2015	2016	2017	2018
e	HLT_e24_lhmedium_L1EM20VH	*Ok*			
	HLT_e24_lhmedium_iloose_L1EM18VH				
	HLT_e24_lhtight_nod0_ivarloose		*Ok*		
	HLT_e26_lhtight_nod0				*Ok*
	HLT_e26_lhtight_nod0_ivarloose		*Ok*	*Ok*	*Ok*
	HLT_e60_lhmedium	*Ok*	*Ok*		
	HLT_e60_lhmedium_nod0		*Ok*	*Ok*	*Ok*
	HLT_e60_medium				
ee	HLT_2e12_lhloose_L12EM10VH	*Ok*			
	HLT_2e15_lhvloose_nod0_L12EM13VH		*Ok*		
	HLT_2e17_lhvloose_nod0		*Ok*		
	HLT_2e17_lhvloose_nod0_L12EM15VHI			*Ok*	*Ok*
	HLT_2e24_lhvloose_nod0			*Ok*	*Ok*
μ	HLT_mu20_iloose_L1MU15	*Ok*			
	HLT_mu26_ivarmedium		*Ok*	*Ok*	*Ok*
	HLT_mu50	*Ok*	*Ok*	*Ok*	*Ok*
	HLT_mu60_0eta105_msonly	*Ok*	*Ok*	*Ok*	*Ok*
$\mu\mu$	HLT_mu18_mu8noL1	*Ok*			
	HLT_mu22_mu8noL1		*Ok*	*Ok*	*Ok*
	HLT_2mu10	*Ok*	*Ok*		
	HLT_2mu14		*Ok*	*Ok*	*Ok*
$e\mu$	HLT_e17_lhloose_mu14	*Ok*			
	HLT_e17_lhloose_nod0_mu14		*Ok*	*Ok*	*Ok*
	HLT_e24_lhmedium_nod0_L1EM20VHI_mu8noL1		*Ok*		
	HLT_e26_lhmedium_nod0_mu8noL1			*Ok*	*Ok*
	HLT_e7_lhmedium_mu24	*Ok*			
	HLT_e7_lhmedium_nod0_mu24		*Ok*	*Ok*	*Ok*
$e\mu\mu$	HLT_e12_lhloose_2mu10	*Ok*			
	HLT_e12_lhloose_nod0_2mu10		*Ok*	*Ok*	*Ok*
$ee\mu$	HLT_2e12_lhloose_mu10	*Ok*			
	HLT_2e12_lhloose_nod0_mu10		*Ok*	*Ok*	*Ok*
eee	HLT_e17_lhloose_2e9_lhloose	*Ok*			
	HLT_e17_lhloose_nod0_2e9_lhloose_nod0		*Ok*		
	HLT_e17_lhloose_nod0_2e10_lhloose_nod0_L1EM15VH_3EM8VH		*Ok*		
	HLT_e24_lhvloose_nod0_2e12_lhvloose_nod0_L1EM20VH_3EM10VH			*Ok*	*Ok*
$\mu\mu\mu$	HLT_mu18_2mu4noL1	*Ok*			
	HLT_mu20_2mu4noL1		*Ok*	*Ok*	*Ok*
	HLT_3mu4			*Ok*	
	HLT_3mu6	*Ok*	*Ok*	*Ok*	*Ok*
	HLT_3mu6_msonly	*Ok*	*Ok*	*Ok*	*Ok*

Table 6.1: Triggers used in the 2015-2018 analysis. Triggers are only used when they are unprescaled (a separate GRL is maintained for each trigger that records which lumiblocks the trigger was unprescaled for). Prescaled triggers are not included because of their low thresholds (the events that pass only prescaled triggers would not pass our lepton p_T cuts). *Ok* means that the specified trigger is used.

6.1.2 Baseline lepton selection

Electrons must pass a baseline selection of:

- $p_T > 7$ GeV and $|\eta| < 2.47$,

- `Loose` likelihood identification,
- $|z_0 sin\theta| < 0.5$ mm,
- the electron is required to pass an object quality check (not from a bad cluster).

As for the muons, they must pass the selections below:

- $p_T > 5$ GeV (> 15 GeV if calo-tagged), $|\eta| < 2.5$,
- `Loose` likelihood identification,
- $|z_0 sin\theta| < 0.5$ mm and $d_0 < 1$ mm (not applied to ME muons since they don't have an ID track),

6.1.3 Quadruplet selection

Once the leptons pass the baseline selections, all same-flavour opposite-sign dilepton pairs are assembled; all possible quadruplets are constructed as combinations of $e^+e^-e^+e^-$, $e^+e^-\mu^+\mu^-$, $\mu^+\mu^-e^+e^-$, and $\mu^+\mu^-\mu^+\mu^-$.
The formed quadruplets must follow the below requirements:

- Overlap-removal on electrons is applied, and are ignored when:

  → They share an ID track with a selected muon.

  → They share their track or cluster in the calorimeter with a selected high-pT electron.

  → They are not passing the likelihood-based identification, they are ignored to avoid poor quality electrons.

  The only case where muons are rejected in the Overlap-removal is when electrons share an ID track with a selected calo-tagged muons.

- The formed quadruplet must have at least one lepton firing a trigger, and if the fired trigger is a multi-trigger, the quadruplet has to be constituted of the specific multi-lepton set, or the quadruplet will be rejected.

- The muon-quadruplet must have either one calorimeter-tagged or one standalone muon. The number of $\mu_{CT} + \mu_{ME}$ must not exceed 1, or the quadruplet will be removed.

- $p_T^1 > 20$ GeV, $p_T^2 > 15$ GeV, $p_T^3 > 10$ GeV, where p_T^i $(i = 1, 3)$ is the transverse momentum running from the lepton with the largest to lowest p_T in the quadruplet.

- ΔR >0.10 (0.20) for same-flavour (different-flavour) leptons in the quadruplet.

6.1.4 Quadruplet ranking

In the case where more than one quadruplet is selected in the event, the quadruplet with the smallest $\Delta m_{ll} \equiv |m_{ab} - m_{cd}|$ is selected, where m_{ab} is the invariant mass that identifies the primary pair of the quadruplet, and m_{cd} identifies the secondary one, satisfying: $m_{ab} > m_{cd}$.

For the four-electron and four-muon quadruplets, an alternative pairing of Same-Flavour Opposite-Sign (SFOS) can be performed. When the positively charged lepton of the primary pair is paired to the negatively charged lepton of the secondary pair, we denote their invariant mass m_{ad}, while where the positively charged lepton of the secondary pair is paired to the negatively charged lepton of the primary pair, we denote their invariant mass m_{cb}.

6.1.5 Event selection

The selected quadruplet has to pass further cuts on the leptons, such as electron quality, impact parameter significance, isolation, and event kinematic requirements.

Leptons further cuts

The requirements that should be applied to leptons in the event selection are:

- All the quadruplets electrons must pass the `Loose` Likelihood identification.

- The transverse impact parameter's significance $d_0^{BL} Sig = d_0/\sigma_{d_0}$, which is calculated relative to the beamline, should be < 5 for electrons and < 3 for muons except for the ME muons since they don't have an ID track.

Isolation

Leptons generated by quantum chromodynamics processes in colliders typically occur in conjunction with nearby particles that leave their tracks and energy deposits in the detectors. On the other hand, leptons from electroweak processes often lack these extra fingerprints. It is possible to differentiate between these two genesis processes using this characteristic of being more "isolated."

The ATLAS experiment has detailed frameworks that define isolation and give clear cuts, or working points, on them. For further information, see reference [89]. For electron isolation and muon isolation, respectively, this analysis employs the `FCLoose` isolation working point and `FCLoose_FixedRad` isolation working point. Cuts are applied to tracker and calorimeter variables at each working point:

Working point	Track Isolation	Calorimeter Isolation
FCLoose	$p_{T,TTVA}^{varcone20}/p_T < 0.15$	$E_T^{cone20}/p_T < 0.2$
FCLoose_FixedRad	$\max(p_{T,TTVA}^{varcone30},\ p_{T,TTVA}^{cone20})/p_T < 0.15$	$E_T^{cone20}/p_T < 0.3$

Table 6.2: Electron and Muon working points definitions.

- The calorimeter cut variable for both WPs is E_T^{cone20} and is defined as the sum of the energies of the topological clusters whose barycenters fall within $\Delta R = \sqrt{(\Delta\eta)^2 + (\Delta\phi)^2} = 0.2$ of the lepton in interest, minus the cluster's energy that is directly associated with the lepton [90].

- The tracker cut variables, $p_{T,TTVA}^{coneXX}$ and $p_{T,TTVA}^{varconeXX}$, are given by the sum of track transverse momenta in a cone of radius ΔR centered around the lepton of interest. To be included in the cone, the track must:

  * Pass `Loose` track quality cut,

  * Have been included in the vertex fit of the lepton of interest,

  * Have $p_T > 1$ GeV.

  The cone radius in $p_{T,TTVA}^{coneXX}$ is given by $\Delta R = XX/100$, while the cone radius for $p_{T,TTVA}^{varconeXX}$ is of variable size and given by $\Delta R = min(10 \text{ GeV } /p_T, XX/100)$. `FCLoose` uses $XX = 20$, while `FCLoose_FixedRad` utilises $XX = 20$ or 30, depending on the transverse momentum of the muon. Table 6.2 summarises the isolation cuts for both electrons and muons.

Corrections are made for contributions from nearby leptons in the aforementioned isolation variables. Only the other three leptons in the quadruplet are utilized for this adjustment, therefore the isolation decision for a lepton is determined for each quadruplet the lepton is used in. These are the corrections made to the isolation variables:

- E_T^{cone20}: subtract the E_T of topoclusters that are both within $0.1 < \Delta R < 0.2$ of the lepton to be corrected and within $\Delta R < 0.1$ of any of the three other leptons.

- $p_{T,TTVA}^{coneXX}$, $p_{T,TTVA}^{varconeXX}$: subtract the ID track p_T of any of the three other leptons if the track is within the *variable size* isolation cone of the particle.

Event Kinematic requirements

Two signal regions are defined in the AS search, SR1 where the four-lepton invariant mass, $m_{4\ell} < 115$ GeV, and SR2 where $m_{4\ell} > 130$ GeV.

The kinematic cuts applied to the dilepton and quadruplet invariant masses are outlined in Table 6.3:

	cuts	SR1	SR2
Event Selection	Quarkonia Veto	$(m_{J/\psi} - 0.25$ GeV $) < m_{ab}, m_{cd}, m_{ad}, m_{cb} < (m_{\psi(2S)} + 0.30$ GeV $)$ or, $(m_{\Upsilon/(1S)} - 0.70$ GeV $) < m_{ab}, m_{cd}, m_{ad}, m_{cb} < (m_{\Upsilon(3S)} + 0.75$ GeV $)$	same
	LowMass Veto	$(m_{ab}, m_{cd}, m_{ad}, m_{cb}) > 5$ GeV	same
	Higgs Mass Window veto	$m_{4\ell} < 115$ GeV	$m_{4\ell} > 130$ GeV
	ZVeto	$m_{ab} \notin [50, 106]$ GeV	m_{ab} and $m_{cd} \notin [83.2, 99.2]$ GeV , m_{ad} and $m_{cb} \notin [87.2, 95.2]$ GeV
	LooseSR	$(m_{ab}, m_{cd}) > 10$ GeV	same
	MediumSR	$m_{cd} > 0.85m_{ab} - 0.1125f(m_{ab})m_{ab}$	same
	TightSR	$\lvert E'_{ab}/M_{4\ell} - 0.5\rvert < 0.008$	same

Table 6.3: Summary of the event selection of SR1 and SR2 for the AS search.

- **Quarkonia veto around J/ψ, $\Upsilon(1S)$, $\Upsilon(2S)$, and $\Upsilon(3S)$:** any event verifying $(m_{J/\psi} - 0.25$ GeV $) < m_{ab}, m_{cd}, m_{ad}, m_{cb} < (m_{\psi(2S)} + 0.30$ GeV $)$ or, $(m_{\Upsilon/(1S)} - 0.70$ GeV $) < m_{ab}, m_{cd}, m_{ad}, m_{cb} < (m_{\Upsilon(3S)} + 0.75$ GeV $)$, is rejected.

- **Low Mass Veto:** is required to avoid discrepancies between data and MC observed in validation plots, verifying $(m_{ab}, m_{cd}, m_{ad}, m_{cb}) > 5$ GeV .

- **Z Veto in SR1:** any event passes this requirement is accepted
  $m_{ab} \notin [50, 106]$ GeV

- **Z Veto in SR2:** any event passes this requirement is accepted
  m_{ab} and $m_{cd} \notin [83.2, 99.2]$ GeV, m_{ad} and $m_{cb} \notin [87.2, 95.2]$ (for $4e$ and 4μ channels).

  The Z veto's cut was optimized by the procedure defined and discussed in [91].

- **Medium SR:** this cut is applied for the the dilepton invariant masses' compatibility. For the HM and LM channels, it was specified as $m_{34}/m_{12} > 0.85$ in the prior iteration (Run2 search). This cut is utilized for AS channel as well as HM throughout the full

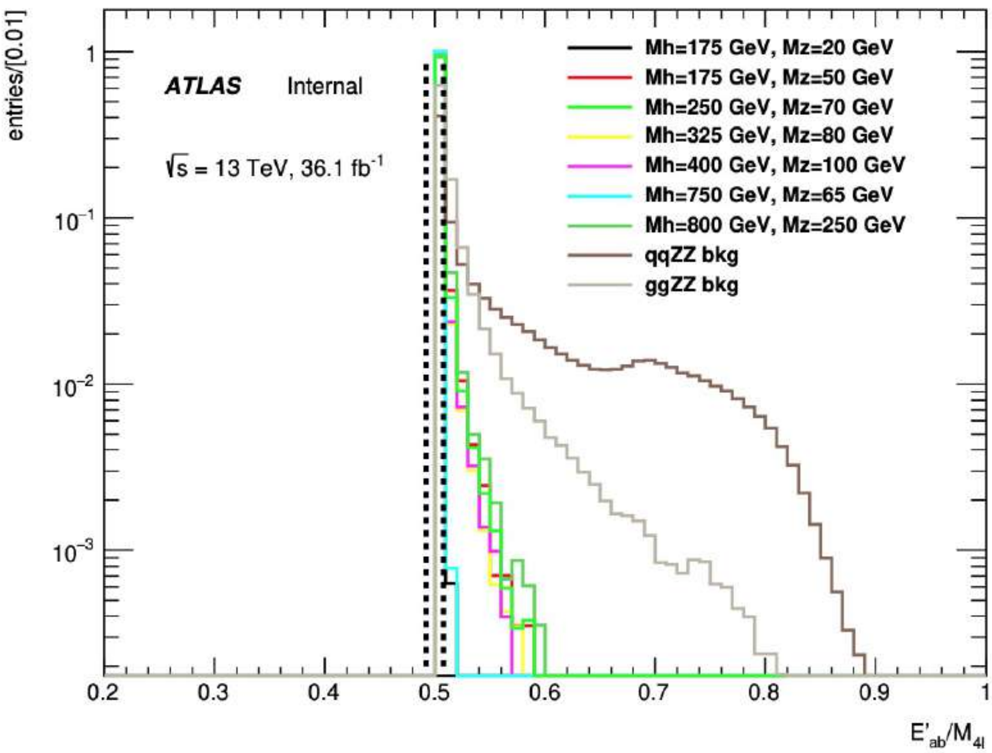

Figure 6.1: $E^{'}_{ab}/m_{4\ell}$ distributions for additional scalar signal hypothesis and the two leading SM background processes. The dotted lines delimit the cut applied using this variable.

Run2 iteration. $m_{cd} > 0.85m_{ab} - 0.1125f(m_{ab})m_{ab}$, where $f(m_{ab})$ is a modulating function with constants, is the definition of the optimal cut. Its derivation is covered in [91].

- **Tight SR:** this requirement is on the $E^{'}_{ab}/m_{4\ell}$ which is a kinematic variable defined as the energy component of the lepton pair's four-momentum in the center-of-momentum frame (CMF) and obtained by:

$$E^{'}_{ab}/m_{4\ell} = \frac{1}{2} \times [1 + (m^2_{ab} - m^2_{cd})/m^2_{4\ell}]. \tag{6.1}$$

Figure 6.1 shows the distributions of the $E^{'}_{ab}/m_{4\ell}$ variable and [91] discusses the Tight SR requirement optimization in details.

6.2 Signal and background simulation

6.2.1 Background simulation

The background processes considered in this search are split into two categories:

Process	Generator	Accuracy	PDF set	Parton showering, hadronization, MPI(Tune and PDF)	K-Factor
$q\bar{q}ZZ^*$	Sherpa 2.2.2 [55–57]	NLO	NNPDF30NNLO[99]	Sherpa 2.2.2 w/NNPDF30NNLO PDF & tune	None
$g\bar{g}ZZ^*$	Sherpa 2.2.2	NLO	NNPDF30NNLO	Sherpa 2.2.2 w/NNPDF30NNLO PDF & tune	1.7[92]
ggF	Powheg [61–65]	NNLO	PDF4LHC15$_{NNLO}$[93]	Pythia8 [53] w/AZNLO[94] & CTEQ6L1 PDF[95]	1.1[96]
VBF	Powheg	NLO	PDF4LHC15$_{NLO}$	Pythia8 w/AZNLO & CTEQ6L1 PDF	None
VH	Pythia8 [54]	LO	NNPDF23LO	Pythia8 w/A14[97] & NNPDF23LO PDF[98]	None
ggZH	Powheg	NLO	PDF4LHC15$_{NLO}$	Pythia8 w/AZNLO & CTEQ6L1 PDF	None
$b\bar{b}H$	MadGraph5_aMC@NLO [66, 67]	NLO	NNPDF23LO	Pythia8 w/A14 & NNPDF23LO PDF	None
$t\bar{t}H$	Powheg	LO	NNPDF30LO	Pythia8 w/A14 & NNPDF23LO PDF	None
VVV	Sherpa 2.2.2 [58]	incl@NLO, 1,2j@LO[57, 59]	NNPDF30NNLO	Sherpa 2.2.2 w/NNPDF30NNLO PDF & tune	None
V+jets	Sherpa 2.2.1	0,1,2j@NLO, 3,4j@LO	NNPDF30NNLO	Sherpa 2.2.1 w/NNPDF30NNLO PDF & tune	0.9751[100]
$t\bar{t}$	Powheg	NLO	NNPDF23NLO	Pythia8 w/A14 & NNPDF2.3LO PDF	1.1398[101]
$t\bar{t}+Z$	Sherpa 2.2.0	LO	NNPDF23NLO	Sherpa 2.2.1 w/NNPDF30NNLO PDF & tune	1.09[102]
WZ	Powheg	NLO	CT10NLO[103]	Pythia8 w/AZNLO & CTEQ6L1 PDF	1.14[101]

Table 6.4: All backgrounds simulation samples along with the k-factors used in this analysis.

Irreducible backgrounds

- $\mathbf{ZZ^* \rightarrow 4l}$: forms the main background of the AS channel, considering both loop-induced $g\bar{g}$-initiated ZZ^* production, and the $q\bar{q}$ non-resonant SM ZZ^* process. It accounts for over 90% of the total prediction.

- $\mathbf{H \rightarrow ZZ^* \rightarrow 4l}$: Higgs boson production via *gluon-gluon Fusion* (ggF), *vector-boson Fusion* (VBF), in association with a vector boson (VH), in association with a vector boson generated by the loop-induced $gg \rightarrow ZH$, and in association with quarks ($t\bar{t}H$ and $b\bar{b}H$) are considered as an irreducible background for the AS channel.

- **VVV**: the triboson backgrounds (ZZZ, WZZ, and WWZ) with four or more leptons originating from the hard scatter (HS).

Reducible backgrounds

- $\mathbf{V + jets}, \mathbf{t\bar{t}}, \mathbf{t\bar{t} + Z}$, and **WZ** backgrounds are considered as reducible backgrounds producing less than four prompt leptons but can contribute to the selection through jets misidentified as leptons.

Table 6.4 lists the samples used to simulate the backgrounds processes.

The influence of numerous pp interactions in the same and neighbouring bunch crossings is included in the production of the simulated samples (pile-up). Then, the latter passed through a GEANT4-based [105] simulation of the ATLAS detector [104]. The reconstruction, identification, isolation, and impact parameter efficiency for electrons and muons were different somewhat from the data. Therefore, weights were used to adjust the simulated events [106, 107]. To fit the data, the lepton momentum scales and resolutions were also modified [107, 108].

Table 6.5 shows the simulated ZZ^* yields after selections since this background accounts for over 90% of the total prediction.

6.2.2 Signal simulation

Signal event samples with different masses of $S \to Z_d Z_d \to 4l$ process were generated using the HAHM and were produced in the ggF production mode. At the generation stage, MadGraph5_aMC@NLO v2.2.3 was used to generate events at leading-order (LO) with the NNPDF23 Parton Distribution Functions (PDF). The parton shower, hadronization, and underlying events' modelling was interfaced with Pythia8 v8.170 using the A14 tune.

Samples were generated respecting the requirements below:

- considering different S and Z_d masses in the region of $m_S < 115$ GeV (SR1), and $m_S > 130$ GeV (SR2) requirement.
- $\kappa >> \epsilon$ to allow only the $S \to Z_d Z_d \to 4l$ decay.
- the dark Higgs width was varied according to the S mass as reported here [109].
- the SM Higgs boson production cross-section $\sigma_{SM}(ggF)$ is used for normalization[1].
- $\mathcal{B}(H \to Z_d Z_d \to 4\ell) = 1$

Figure 6.2 illustrates the width of both SM and dark Higgses.

The yields after selections application are represented in Table 6.6 for $(m_{Z_d}, m_S) = (20, 50)$ and $(m_{Z_d}, m_S) = (50, 400)$ GeV mass points, and their efficiencies as shown in Table 6.7.

[1] https://twiki.cern.ch/twiki/bin/view/LHCPhysics/CERNYellowReportPageBSMAt7TeV

Cleaning	96200							
Primary Vertex	70400							
Selection	$4e$		$2e2\mu$		4μ		all	
	Yield	Eff(%)	Yield	Eff(%)	Yield	Eff(%)	Yield	Eff(%)
SFOS	4770	100	8900	100	3250	100	16900	100
Not Overlaps	4770	99.9	8890	99.9	3250	100	16900	99.9
Kinematics	4290	89.9	7690	86.4	2710	83.4	14700	86.8
Trigger Matched	4250	89.1	7660	86.1	2710	83.5	14600	86.5
DeltaR	4040	84.7	7170	80.5	2720	83.6	13900	82.3
μ Quality	4040	84.7	7170	80.5	2710	83.5	13900	82.3
Isolation	1510	31.7	3570	40.1	2260	69.5	7340	43.4
Electron ID	934	19.6	2790	31.3	2260	69.5	5980	35.3
Impact Parameter	917	19.2	2690	30.3	2150	66.0	5760	34.0
QVeto	866	18.1	2580	28.9	1960	60.4	5410	31.9
Low Mass Veto	837	17.5	2460	27.6	1830	56.5	5130	30.3
SR1								
Higgs Window	105	2.20	410	4.61	399	12.3	915	5.41
ZVeto	91.3	1.91	165	1.86	344	10.6	601	3.55
LooseSR	77.2	1.62	84.9	0.954	285	8.77	447	2.64
MediumSR	23.2	0.487	12.3	0.138	75.1	2.31	111	0.653
TightSR	8.50	0.178	5.97	0.0671	26.8	0.825	41.3	0.244
SR2								
Higgs Window	716	15.0	1990	22.4	1380	42.6	4090	24.2
ZVeto	62.4	1.31	140	1.57	115	3.55	318	1.88
LooseSR	60.7	1.27	122	1.37	110	3.38	293	1.73
MediumSR	22.8	0.478	34.3	0.385	41.2	1.27	98.3	0.581
TightSR	14.0	0.293	23.4	0.263	26.6	0.817	63.9	0.378

Table 6.5: Cut flow for the simulated $ZZ^* \to 4\ell$ background with all production modes combined, corresponding to the full 2015–2018 data set, expressed as the number of predicted events and the fraction of events with a same-flavour opposite-sign quadruplet. Yields from each simulation campaign are individually normalized to the corresponding integrated luminosities (2015–2016: 36.2 fb^{-1}; 2017: 44.3 fb^{-1}; 2018: 58.45 fb^{-1}) and then combined (2015–2018: 139 fb^{-1}). Per-channel, the quadruplet cutflow can increase because events can move from one channel to another during the quadruplet selection if a higher-ranked quadruplet fails a cut that a lower-ranked one can pass (however, the cutflow summed across all channels can only decrease).

Selection	$(m_{Z_d}, m_S) = (20, 50)$ GeV				$(m_{Z_d}, m_S) = (50, 400)$ GeV			
	4e	2e2μ	4μ	all	4e	2e2μ	4μ	all
All	190000.000	190000.000	190000.000	190000.000	185039.720	185039.720	185039.720	185039.720
Overlap Event	190000.000	190000.000	190000.000	190000.000	185039.720	185039.720	185039.720	185039.720
Cleaning	190000.000	190000.000	190000.000	190000.000	185039.720	185039.720	185039.720	185039.720
PrimaryVertex	190000.000	190000.000	190000.000	190000.000	185039.720	185039.720	185039.720	185039.720
SFOS	3450.756	8919.814	6301.347	18671.917	37294.128	70642.735	32465.668	140402.531
Not Overlaps	3449.735	8916.470	6301.347	18667.551	37232.133	70562.442	32541.291	140335.865
Kinematics	2798.726	6214.907	2718.068	11731.702	36799.821	70300.796	32605.984	139706.601
Trigger Matched	2748.993	6211.297	2718.068	11678.358	36766.631	70288.697	32620.499	139675.827
DeltaR	2718.490	5601.768	2610.867	10931.125	36173.122	69601.775	32752.044	138526.940
μ Quality	2718.490	5601.937	2609.195	10929.622	36175.090	69593.140	32674.194	138442.425
Isolation	976.008	2546.520	1979.456	5501.984	25172.903	55759.806	30091.744	111024.453
Electron ID	652.079	2030.268	1979.456	4661.803	20134.228	49717.790	30091.744	99943.762
Impact Parameter	647.585	1983.055	1904.331	4534.970	19970.952	49055.728	29496.056	98522.736
Impact Parameter Z	646.534	1976.309	1902.236	4525.079	19933.329	48979.232	29459.000	98371.561
Impact Parameter D	646.534	1976.309	1902.236	4525.079	19933.329	48979.232	29459.000	98371.561
QVeto	555.074	1976.309	1621.124	4152.507	19932.371	48973.712	29452.074	98358.157
Low Mass Veto	536.281	1976.309	1556.778	4069.367	19932.371	48973.712	29451.273	98357.355
Higgs Window	535.560	1975.347	1556.778	4067.685	19931.388	48973.682	29450.184	98355.255
ZVeto	534.473	1975.347	1556.778	4066.597	19109.494	48973.536	28171.032	96254.063
LooseSR	534.473	1974.253	1556.778	4065.504	19109.494	48970.452	28168.920	96248.866
MediumSR	531.960	1964.048	1552.974	4048.982	18823.040	47610.828	27089.683	93523.552
TightSR	337.143	1385.954	1351.171	3074.268	18812.181	47608.624	27029.912	93450.717

Table 6.6: Cut-flow for the simulated signals with $(m_{Z_d}, m_S) = (20, 50)$ and $(m_{Z_d}, m_S) = (50, 400)$. The represented yields from simulation are for the combined campaigns (2015-18).

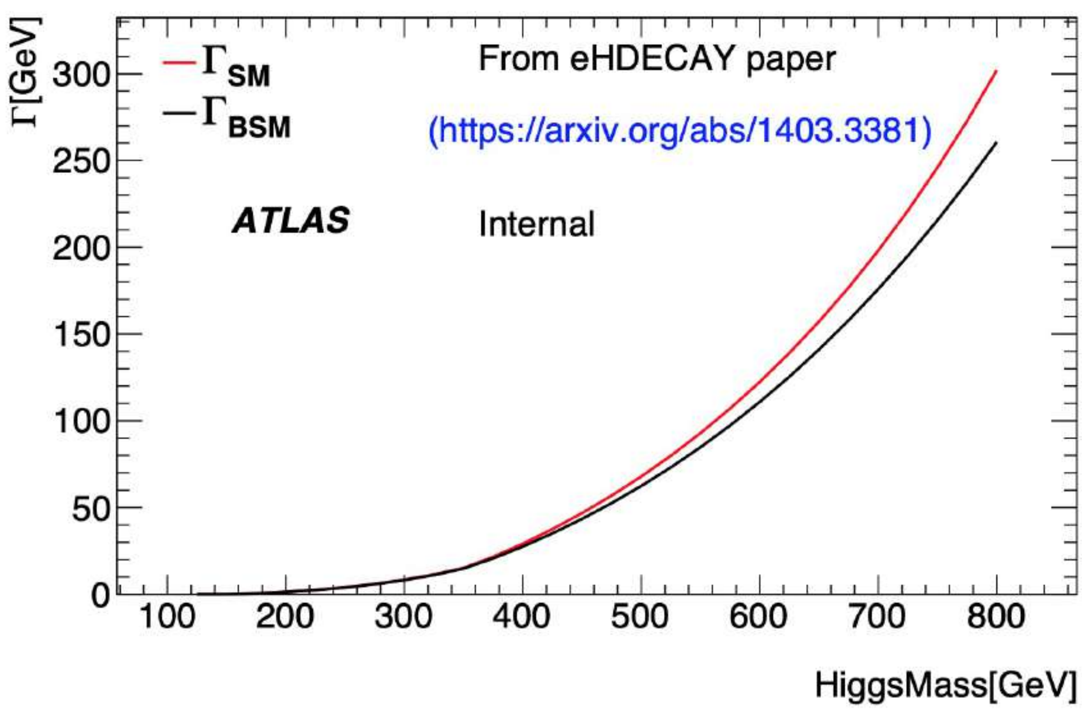

Figure 6.2: The SM Higgs boson's width compared to that of the BSM dark Higgs boson as a function of mass.

Selection	$(m_{Z_d}, m_S) = (20, 50)$ GeV				$(m_{Z_d}, m_S) = (50, 400)$ GeV			
	eff_{4e}	$eff_{2e2\mu}$	$eff_{4\mu}$	all	eff_{4e}	$eff_{2e2\mu}$	$eff_{4\mu}$	all
SFOS	100	100	100	100	100	100	100	100
Not Overlaps	99.97	99.96	100	100	99.83	99.88	100	99.95
Kinematics	81.1	69.67	43.13	99.97	98.67	99.51	100	99.5
Trigger Matched	79.66	69.63	43.13	62.83	98.58	99.45	100	99.48
DeltaR	78.78	62.8	41.43	58.54	96.99	98.52	100	98.66
μ Quality	78.78	62.8	41.41	58.53	96.99	98.51	100	98.6
Isolation	28.28	28.54	31.41	29.47	67.5	78.93	92.68	79.07
Electron ID	18.89	22.76	31.41	24.97	54	70.38	92.68	71.18
Impact Parameter	18.76	22.23	30.22	24.29	53.55	69.44	90.85	70.17
Impact Parameter Z	18.73	22.15	30.19	24.23	53.45	69.33	90.74	70.06
Impact Parameter D	18.73	22.15	30.19	24.23	53.45	69.33	90.74	70.06
QVeto	16.08	22.15	25.73	22.24	53.45	69.32	90.71	70.05
Low Mass Veto	15.54	22.15	24.7	22.24	53.45	69.32	90.71	70.05
Higgs Window	15.52	22.14	24.7	21.78	53.44	69.32	90.71	70.05
ZVeto	15.49	22.14	24.7	21.78	51.24	69.32	86.77	68.55
LooseSR	15.49	22.13	24.7	21.77	51.24	69.32	86.76	68.55
MediumSR	15.41	22.01	24.64	21.68	50.47	67.39	83.44	66.61
TightSR	9.77	15.54	21.44	16.46	50.44	67.39	83.25	66.56

Table 6.7: Cut-flow efficiency in SR1 and SR2.

6.3 Background estimation

The two types of background estimation that we adopted in this analysis are subject to two methods:

6.3.1 Validation region

The $ZZ^* \to 4\ell$ irreducible background is estimated using Monte Carlo simulation and validated by validation region VR3, and it is defined as it is orthogonal to the signal by inverting the MediumSR cut and inverting the Higgs window requirements in the SR:

- $m_{cd} < 0.85 m_{ab} - 0.1125 f(m_{ab}) m_{ab}$
- $m_{4\ell} < 115$ GeV & $m_{4\ell} > 130$ GeV.

These cuts result in the domination of the $ZZ^* \to 4\ell$ process in the validation region 3, as shown in Figure 6.3 for both the average di-lepton mass and the invariant mass distributions, and the yields are as in Table 6.8.

6.3.2 Data-driven estimation: ABCD method

This method is performed to estimate the reducible backgrounds such as $Z + jets$ and $t\bar{t}$ using the isolation and impact parameters as discriminants which are mentioned earlier. It is defined by four regions from the two variables: A, B, C, and D.

Channel	VR 3	
	Expected	Observed
$4e$	68.15 ± 3.97	70
4μ	242.28 ± 1.70	234
$2e2\mu$	162.79 ± 1.27	164
Combined	473.23 ± 4.50	468

Table 6.8: Expected background yields and observed yields in the validation regions per channel. The uncertainties listed are statistical and systematic, respectively.

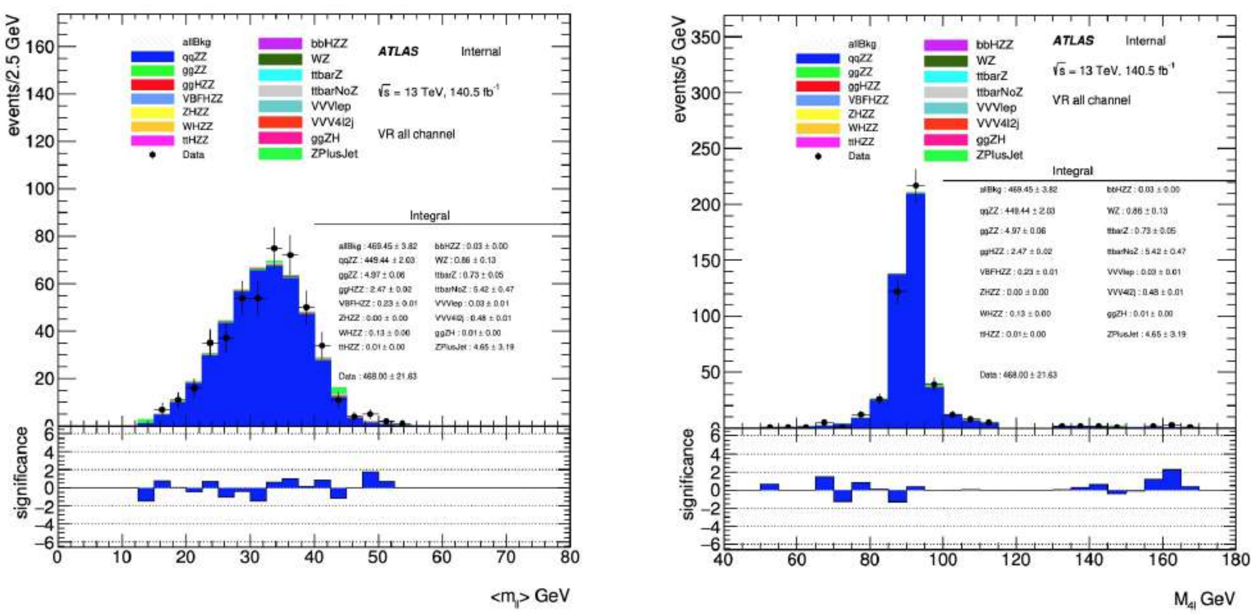

(a) (b)

Figure 6.3: Distribution of $m_{2\ell}$ 6.3a, and $m_{4\ell}$ 6.3b in validation region for all channels combined in 2015-18 data.

The two leptons in the $Z + jets$ process where their dilepton mass is closest to the Z boson mass must pass both requirements, while for the $t\bar{t}$ case, the two leptons with the largest p_T must pass both requirements.
The two uncorrelated variables divided up into four regions (Figure 6.4):

- **Region A:** All the quadruplet leptons pass both requirements (Signal region).
- **Region B:** The two remaining leptons both pass the isolation cut but at least one of them fails the impact parameter cut.
- **Region C:** The two remaining leptons both pass the impact parameter cut but at

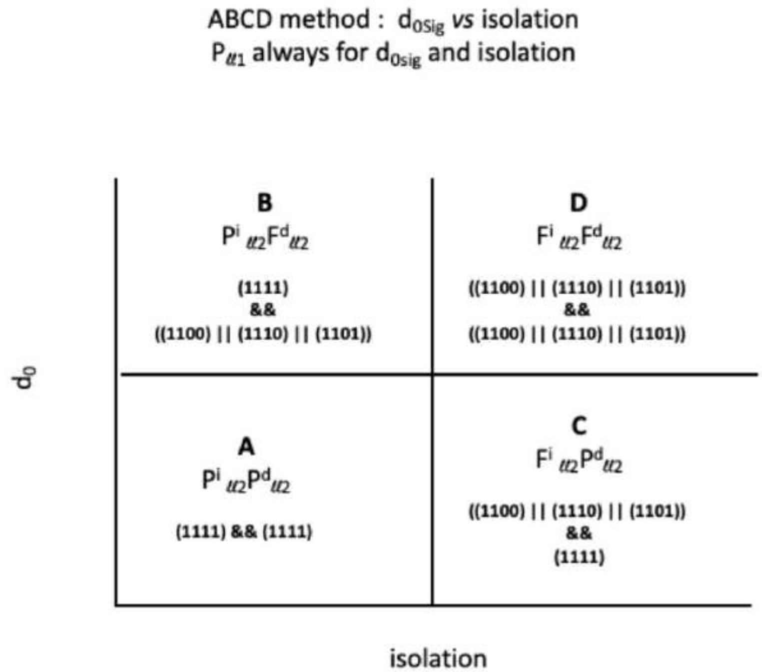

Figure 6.4: ABCD method region definitions.

least one of them fails the isolation cut.

- **Region D:** One of the remaining leptons should, at least, fail both cuts.

The variables are assumed to be uncorrelated by this method, and to double check, the correlation coefficient r is calculated in this case by:

$$r = \frac{A \times D - B \times C}{\sqrt{(A+C) \times (B+D) \times (A+B) \times (C+D)}}, \tag{6.2}$$

and shown in Table 6.9 for all the possible final state channels. The higher correlation

r	2015–16 data	2017 data	2018 data	Full data
4e	0.01	0.02	0.02	0.002
2e2μ	0.02	0.02	0.02	0.002
4μ	0.59	0.59	0.59	0.38

Table 6.9: Correlation coefficient for the isolation and impact parameter requirements for the channels $4e$, $2e2\mu$, and 4μ, for the 2015–16, 2017 and 2018 data sets. All selections have been applied through the quarkonia vetoes.

observed for the 4μ channel was taken into account, in Run2, as a systematic uncertainty in the final results by multiplying the statistical error by r[1].

The method is performed as follows:

- All background processes are considered except the one we want to estimate, either $t\bar{t}$ or $Z + jets$; X_{bkg}.

[1] To have enough statistics, the study is done at the level of the Qveto cut, and the electron ID cut is not applied.

- Calculate the number of background events in each region: B_{bkg}, C_{bkg}, and D_{bkg}.
- Calculate the number of data events in each region: B_{data}, C_{data}, and D_{data}.
- Calculate the difference between data and background, region by region: $B_{data} - B_{bkg}$, $C_{data} - C_{bkg}$, and $D_{data} - D_{bkg}$.
- The background events' number in region A of X_{bkg} is estimated by:

$$A_{bkg} = \epsilon \times \frac{(B_{data} - B_{bkg}) \times (C_{data} - C_{bkg})}{(D_{data} - D_{bkg})}, \tag{6.3}$$

where ϵ is the efficiency of the remaining cuts.

Table 6.10 shows the results of each step of the method on the $t\bar{t}$ and $Z+jets$ backgrounds using 2018 data.

Yields data	2018 data					
	$t\bar{t}$			$Z+jets$		
	$4e$	$2e2\mu$	4μ	$4e$	$2e2\mu$	4μ
B	510	840	103	455	932	67
C	534040	616079	782	534040	616286	782
D	82549	113753	2163	55811	91529	1199
–	Yields bkg without $t\bar{t}$			Yields bkg without $Z+jets$		
B	244.85	329.74	58.96	70.11	137.84	30.05
C	506627	592480	495.85	44805	49741	364.13
D	46509.1	55146.3	1097.74	18131.8	28460.2	595.9
–	(data)−(bkg without $t\bar{t}$)			(data)−(bkg without $Z+jets$)		
B	265.15	510.26	44.04	384.9	794.2	37.0
C	27413	23598.9	286.15	489235	566545	417.9
D	36039.9	58606.7	1065.26	37679.2	63068.8	603.1
–	SR1					
efficiency ϵ	$(3.0 \pm 1.7) \times 10^{-6}$	$(1.7 \pm 0.2) \times 10^{-5}$	$(0.2 \pm 0.00) \times 10^{-1}$	$(2.9 \pm 1.7) \times 10^{-6}$	$(1.7 \pm 0.2) \times 10^{-5}$	$(0.2 \pm 0.0) \times 10^{-1}$
Bkg estimates	0.0 ± 0.0	0.0 ± 0.0	0.2 ± 0.2	0.0 ± 0.0	0.1 ± 0.0	0.6 ± 0.3
Estimates including systematics	0.0 ± 0.0	0.0 ± 0.0	0.2 ± 0.2	0.0 ± 0.0	0.1 ± 0.0	0.6 ± 0.4
–	SR2					
efficiency (ϵ)	$(2.4 \pm 0.5) \times 10^{-5}$	$(3.4 \pm 0.3) \times 10^{-5}$	$(0.3 \pm 0.0) \times 10^{-1}$	$(2.4 \pm 0.5) \times 10^{-5}$	$(3.4 \pm 0.3) \times 10^{-5}$	$(0.3 \pm 0.0) \times 10^{-1}$
Bkg estimates	0.0 ± 0.0	0.0 ± 0.0	0.4 ± 0.4	0.1 ± 0.0	0.2 ± 0.0	0.9 ± 0.4
Estimates including systematics	0.0 ± 0.0	0.0 ± 0.0	0.4 ± 0.4	0.1 ± 0.0	0.2 ± 0.0	0.9 ± 0.7

Table 6.10: Estimation of the $t\bar{t}$ and $Z+jets$ backgrounds for the 2018 data (with mc16e MC), by channel.

6.4 Systematic uncertainties

Two classes of systematics are considered and needed to be assessed:

- **Experimental systematics:** are coming from the detector's nature, for instance, the uncertainties associated with lepton identifications and uncertainties in momentum resolution and energy scale. Those are applied to signal and background estimated by simulation.

- **Theoretical systematics:** are generated by parameters and modelling uncertainties used in the simulation, such as QCD scale, PDFs, and parton showering.

6.4.1 Experimental systematics

Electrons

To increase agreement with data, the resolution, energy scale, and identification/isolation/reconst efficiencies of electrons in simulation are adjusted. Each electron receives electron resolution and energy scale corrections, and identification, isolation, and reconstruction efficiency corrections are applied by event re-weighting.

The correction model provided by `AsgElectronEfficeincyCorrectionTool` [110] from the egamma CP group is used, where the keys are:

- `EL_EFF_ID_TOTAL`: Identification.
- `EL_EFF_ISO_TOTAL`: Isolation.
- `EL_EFF_RECO_TOTAL`: Reconstruction.

For resolution and energy scale corrections, kinematic smearing and calibration uncertainties are considered, where the calibration is a transfer factor from the detector's raw hit value to energy. As for smearing, it simulates detector resolution for MC samples to improve the agreement between data and simulation.
The tools used are `EgammaCalibrationAndSmearingTool` [110], with the following keys:

- `EG_RESOLUTION_ALL`: Smearing.
- `EG_SCALE_ALL`: Calibration.

Muons

As for muons, the resolution, momentum scale, and isolation/reconstruction/track-to-vertex association efficiencies of muons in simulation are as well corrected. The tool used for that purpose is `CP::MuonEfficiencyScaleFactors` [110], and the associated keys are:

- `MUON_EFF_ISO_STAT`: Isolation efficiency broken up into statistical errors on the weights.
- `MUON_EFF_ISO_SYS`: Isolation efficiency broken up into systematic errors on the weights.

- MUON_EFF_RECO_STAT: Reconstruction efficiency broken up into statistical errors on the weights.
- MUON_EFF_RECO_STAT_LOWPT: Reconstruction efficiency which is extrapolated for muon with $p_T < 10$ GeV, broken up into statistical errors on the weights.
- MUON_EFF_RECO_SYS: Reconstruction efficiency broken up into systematic errors on the weights.
- MUON_EFF_RECO_SYS_LOWPT: Reconstruction efficiency which is extrapolated for muon with $p_T < 10$ GeV, broken up into systematic errors on the weights.
- MUON_TTVA_ISO_STAT: Track-to-vertex association efficiency broken up into statistical errors on the weights.
- MUON_TTVA_ISO_SYS: Track-to-vertex association efficiency broken up into systematic errors on the weights.

The calibration, for the case of muons, is a transfer factor from detector's raw hit to momentum,
and the CP::MuonCalibrationAndSmearingTool tool [110] is used for that purpose along with the smearing, and the keys are:

- MUON_ID: Muon inner detector track p_T smearing.
- MUON_MS: Muon spectrometer track p_T smearing.
- MUON_SCALE: Muon calibration scale.

Luminosity

The uncertainty for the combined Run2 dataset (2015-8) is **1.7%** as reported [111], and its methodology is documented in: [112].

Pileup Re-Weighting (PRW)

Some discrepancies are seen between the predicted and measured inelastic cross-section in the fiducial volume defined by $M_X > 13$ GeV, where $M_X > 13$ is the mass of the non-diffractive hadronic system, and they arise from the mismodelling of the central activity by the MC tune. To cover those discrepancies, the pileup re-weighting uncertainties are introduced on the mean number of interactions μ corresponding to a given MC event.

Systematic	SR1			SR2		
	$(m_{Z_d}, m_S) = (35, 80)$ GeV			$(m_{Z_d}, m_S) = (20, 175)$ GeV		
	$4e$	$2e2\mu$	4μ	$4e$	$2e2\mu$	4μ
EG_RESOLUTION_ALL	$^{-2.93}_{+0.00}$	$^{-2.14}_{+0.00}$	$^{+0.00}_{-0.05}$	$^{+0.32}_{0.00}$	$^{+0.07}_{-0.01}$	$^{0.00}_{+0.12}$
EG_SCALE_ALL	$^{+0.95}_{-0.40}$	$^{0.00}_{-0.44}$	–	$^{+0.38}_{-0.54}$	±0.15	$^{0.00}_{+0.06}$
EL_EFF_ID_TOTAL_1NPCOR_PLUS_UNCOR	$^{+17.3}_{-14.6}$	$^{+8.24}_{-7.83}$	–	$^{+13.8}_{-12.7}$	$^{+6.27}_{-6.14}$	–
EL_EFF_Iso_TOTAL_1NPCOR_PLUS_UNCOR	$^{+1.61}_{-1.59}$	$^{+0.785}_{-0.784}$	–	$^{+0.95}_{-0.94}$	±0.42	–
EL_EFF_Reco_TOTAL_1NPCOR_PLUS_UNCOR	$^{+4.51}_{-4.37}$	$^{+2.31}_{-2.29}$	–	$^{+2.03}_{-2.}$	±0.92	–
MUONS_ID	–	$^{-1.22}_{+0.00}$	$^{-1.51}_{+0.24}$	–	$^{+0.04}_{-0.00}$	$^{0.00}_{+0.23}$
MUONS_MS	–	$^{-1.77}_{+0.00}$	$^{-2.35}_{+1.01}$	–	$^{-0.05}_{+0.03}$	$^{0.00}_{+0.56}$
MUONS_SAGITTA_RESBIAS	–	$^{+0.00}_{-0.29}$	$^{+0.869}_{-0.00}$	–	–	–
MUONS_SAGITTA_RHO	–	$^{-0.49}_{+0.00}$	$^{+0.725}_{-0.00}$	–	–	–
MUONS_SCALE	–	$^{-1.14}_{+0.00}$	$^{-1.16}_{+0.162}$	–	$^{-0.06}_{+0.05}$	$^{-0.00}_{+0.11}$
MUON_EFF_ISO_STAT	–	$^{+0.23}_{-0.23}$	$^{+0.44}_{-0.44}$	–	±0.13	±0.28
MUON_EFF_ISO_SYS	–	$^{+1.1}_{-1.1}$	$^{+2.13}_{-2.08}$	–	±0.52	$^{+1.06}_{-1.05}$
MUON_EFF_RECO_STAT	–	$^{+0.12}_{-0.12}$	$^{+0.24}_{-0.24}$	–	±0.15	±0.29
MUON_EFF_RECO_STAT_LOWPT	–	$^{+0.17}_{-0.17}$	$^{+0.33}_{-0.33}$	–	±0.06	±0.12
MUON_EFF_RECO_SYS	–	$^{+0.63}_{-0.62}$	$^{+1.30}_{-1.27}$	–	±0.59	$^{+1.16}_{-1.15}$
MUON_EFF_RECO_SYS_LOWPT	–	$^{+0.54}_{-0.54}$	$^{+1.06}_{-1.06}$	–	±0.15	±0.33
MUON_EFF_TTVA_STAT	–	$^{+0.18}_{-0.19}$	$^{+0.33}_{-0.37}$	–	±0.06	±0.11
MUON_EFF_TTVA_SYS	–	$^{+0.03}_{-0.02}$	$^{+0.05}_{-0.04}$	–	±0.05	±0.09
PileupWeight	$^{-2.52}_{+2.15}$	$^{-1.25}_{+1.2}$	$^{-1.03}_{+0.94}$	$^{-1.3}_{+0.66}$	$^{-0.73}_{+0.78}$	$^{-0.35}_{+0.36}$

Table 6.11: The relative experimental uncertainties (%) in SR1 (SR2) for the mass point $(m_{Z_d}, m_S) = (35, 80)$ GeV ($(20, 175)$ GeV) for mc16a which corresponds to the 2015-16 collected data.

Table 6.11 presents the relative experimental uncertainties (%) in SR1 (SR2) for the mass point $(m_{Z_d}, m_S) = (35, 80)$ GeV ($(20, 175)$ GeV). Table 6.12 shows the relative experimental uncertainties (%) in SR1 (SR2) for the main background $ZZ^* \to 4\ell$.

6.4.2 Theoretical systematics

Signal

In this search, the QCD and PDF signal uncertainties are the ones recommended in the Reference [113] as shown in Table 6.13 for some dark Higgs' mass points.

Background

The theoretical QCD and PDF uncertainties of the ZZ^* background are obtained as follows:

- **Intra-PDF set:** The MC was created nominally using the `NNPDF23_lo_as_0130_qed` PDF set (LHAPDF ID 247000). There are 100 deviations from the nominal in this group. Each PDF set produces a separate weight during the event generation step, which is then applied as the event weight in a truth analysis. There are 101 weights

Systematic	$ZZ^* \to 4\ell$					
	SR1			SR2		
	$4e$	$2e2\mu$	4μ	$4e$	$2e2\mu$	4μ
EG_RESOLUTION_ALL	$^{+1.71}_{0}$	$^{0}_{-0.64}$	$^{-0.02}_{0.01}$	$^{-0.32}_{0}$	$^{-0.25}_{+0.02}$	$^{+0.01}_{-0.00}$
EG_SCALE_ALL	$^{-1.44}_{+0.88}$	$^{-0.56}_{+0.17}$	$^{+0.00}_{-0.01}$	$^{+1.59}_{-1.18}$	$^{+1.23}_{-0.82}$	$^{+0.00}_{-0.01}$
EL_EFF_ID_TOTAL_1NPCOR_PLUS_UNCOR	$^{+16.6}_{-14.3}$	$^{+7.54}_{-7.23}$	–	$^{+7.54}_{-7.08}$	$^{+3.73}_{-3.67}$	–
EL_EFF_Iso_TOTAL_1NPCOR_PLUS_UNCOR	$^{+2.65}_{-2.62}$	±1.1	–	$^{+0.813}_{-0.806}$	±0.39	–
EL_EFF_Reco_TOTAL_1NPCOR_PLUS_UNCOR	$^{+4.86}_{-4.72}$	±2.36	–	$^{+1.8}_{-1.78}$	±0.89	–
MUONS_ID	–	$^{0.00}_{+0.18}$	$^{-0.35}_{0.00}$	–	$^{0.00}_{+0.16}$	$^{-0.04}_{+0.81}$
MUONS_MS	–	±0.49	±0.66	–	±0.15	±0.46
MUONS_SAGITTA_RESBIAS	–	–	–	–	–	–
MUONS_SAGITTA_RHO	–	–	–	–	–	–
MUONS_SCALE	–	$^{+0.34}_{-0.01}$	$^{+0.35}_{-0.2}$	–	$^{-0.35}_{+0.60}$	$^{-0.32}_{+0.65}$
MUON_EFF_ISO_STAT	–	±0.44	±0.98	–	±0.11	±0.27
MUON_EFF_ISO_SYS	–	±0.99	$^{+2.02}_{-1.99}$	–	±0.58	$^{+1.2}_{-1.19}$
MUON_EFF_RECO_STAT	–	±0.13	±0.24	–	±0.18	±0.35
MUON_EFF_RECO_STAT_LOWPT	–	±0.2	±0.38	–	±0.04	±0.09
MUON_EFF_RECO_SYS	–	±0.60	$^{+1.07}_{-1.06}$	–	$^{+0.81}_{-0.81}$	$^{+1.63}_{-1.6}$
MUON_EFF_RECO_SYS_LOWPT	–	±0.53	±1.05	–	±0.11	±0.26
MUON_EFF_TTVA_STAT	–	±0.08	±0.16	–	±0.07	±0.13
MUON_EFF_TTVA_SYS	–	±0.12	±0.25	–	±0.05	±0.11
PileupWeight	$^{-1.91}_{+1.81}$	$^{-0.89}_{+0.71}$	$^{-0.76}_{+0.57}$	$^{-1.1}_{+1.06}$	$^{-0.49}_{+0.45}$	$^{-0.16}_{+0.20}$

Table 6.12: The relative experimental uncertainties (%) in SR1 (SR2) for the $ZZ^* \to 4\ell$ backgrounds for mc16a+d+e (2015–8) simulation.

m_S (GeV) \ uncertainties(%)	QCD up	QCD down	PDF^{up}_{down}
20	25.7	-22.5	±4.8
80	9.4	-9.5	±3.4
100	8.4	-8.8	±3.2
250	5.9	-6.5	±2.9
450	5.7	-5.3	±3
750	5.4	-4.8	±3.9

Table 6.13: Theoretical systematic uncertainties of some signal mass points.

and 101 signal region histograms for each of the 101 PDF sets (100 variants and the nominal). The quantiles of a distribution of normalized yields, which are 15.87% and 84.14%, are then used to estimate the asymmetric systematic uncertainty on the acceptance.

- **Inter-PDF set:** With the alternative PDF collections `CT14lo` (LHAPDF ID 13200) and `MMHT2014lo68cl` (LHAPDF ID 25000), the background samples were created. According to `NNPDF23_lo_as_0130_qed`, the nominal member of each set was regarded as an inter-PDF variation from the nominal PDF set. The process is the same as it is for uncertainty in intra-PDF sets. The greatest yields above and below the nominal in a distribution of the normalized yields (envelope) are then used to determine the asymmetric systematic uncertainty on the acceptance.

- **QCD scale:** The choice of the QCD renormalization and factorization scales, as well as knowledge of the momentum fraction x carried by each parton, are necessary for event generation. Experimentally PDFs are used to identify the proper QCD normalization and factorization scales. Variations in the PDF and QCD scales are used to evaluate the underlying systematic uncertainty.

  Seven pairwise variations of the renormalization μ_r and factorization μ_f scales were considered: $(\mu_r\ ,\ \mu_f\ )$ = (0.5, 0.5), (0.5, 1.0), (1.0, 0.5), (1.0, 2.0), (2.0, 1.0), (2.0, 2.0). The procedure is the same as it is for PDF set uncertainties.

Table 6.14 shows the QCD and PDF uncertainties in UP and DOWN variations of the ZZ^* background in SR1 and SR2.

Intra PDF uncertainty				
Bkg	SR1		SR2	
	up	down	up	down
qqZZ	1.30	1.15	1.37	1.11
ggZZ	2.14	1.53	1.92	1.44
Inter PDF uncertainty				
qqZZ	1.06	2	1.04	2.1
ggZZ	1.35	0.7	1.8	0.8
QCD uncertainty				
qqZZ	6.59	5.22	6.06	3.89
ggZZ	35.81	23.31	34.67	22.79

Table 6.14: Theoretical systematic uncertainties of ZZ^* in SR1 and SR2 signal regions.

6.5 Results

The distributions of the average dilepton mass, $< m_{\ell\ell} >$, and $m_{4\ell}$ in both SR1 and SR2 for the $4e$ final state using the full Run2 data are illustrated in Figure 6.5. Same thing is shown in Figures 6.6, 6.7 and 6.8 for $2e2\mu$, 4μ, and combined channels respectively. Table 6.15 summarises the expected and the observed yields in both SR1 and SR2 for the combined channels using full MC simulation.

Process	Yield (±stat. ± syst.)					
	SR1			SR2		
$ZZ^* \to 4\ell$	41.2	±0.5	±4.7	63.9	±0.6	±3.1
$H \to ZZ^* \to 4\ell$	0.64	±0.01	±0.05	0.23	±0.01	±0.04
WZ	0.10	±0.04	±0.03	0.46	±0.10	±0.05
VVV	0.08	±0.01	±0.02	0.78	±0.02	±0.17
$t\bar{t}$	0.33	±0.00	±0.31	0.78	±0.00	±0.46
$Z +$ jets	0.70	±0.01	±0.72	2.50	±0.00	±1.08
Total	43.1	±0.5	±4.7	68.7	±0.6	±3.5
Data	45			58		

Table 6.15: Expected event yields of the SM background processes and observed data in SR1 and SR2 with statistical and systematic uncertainties.

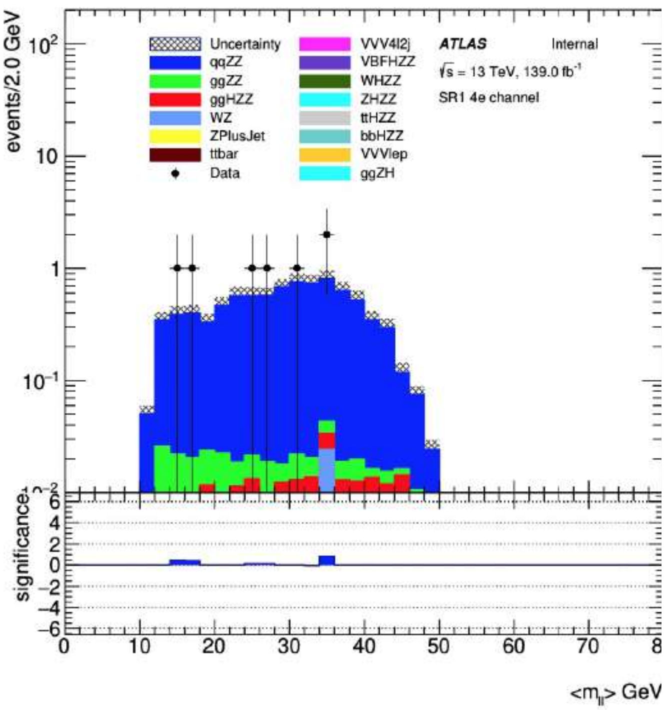

(a)

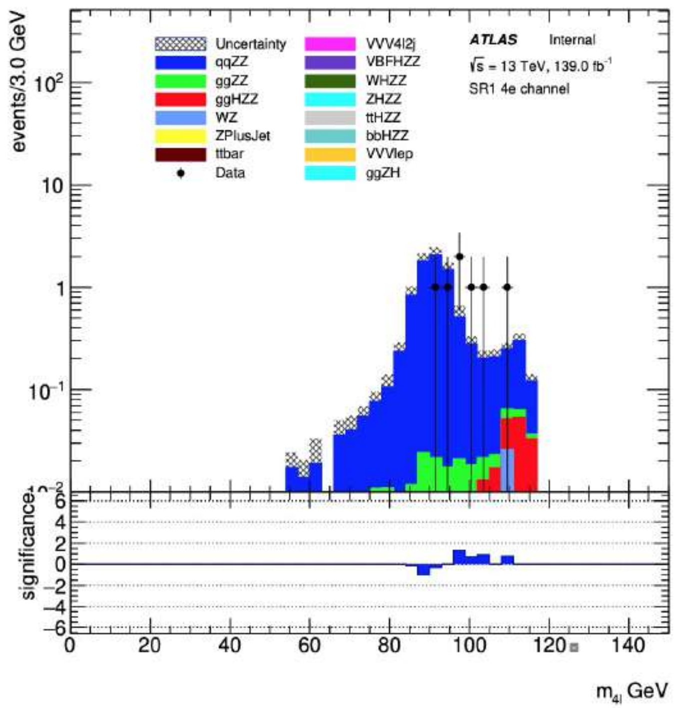

(b)

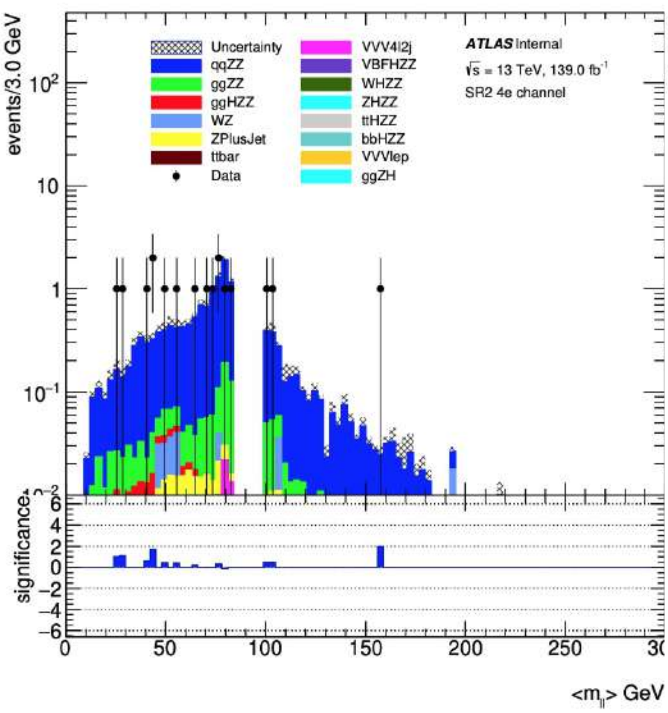

(c)

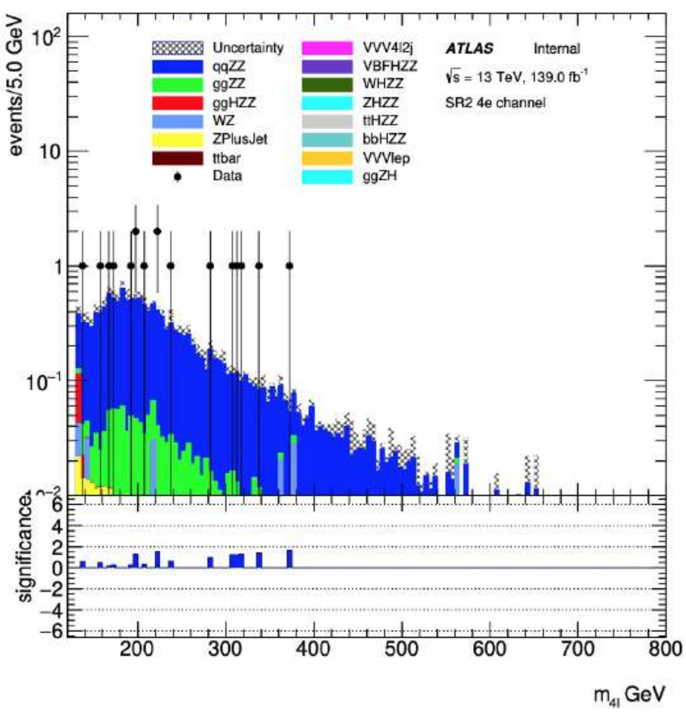

(d)

Figure 6.5: a (c) and b (d) are respectively the distributions of $< m_{ll} >$ and $m_{4\ell}$ in SR1 (SR2) for the $4e$ channel using the full MC campaigns merged.

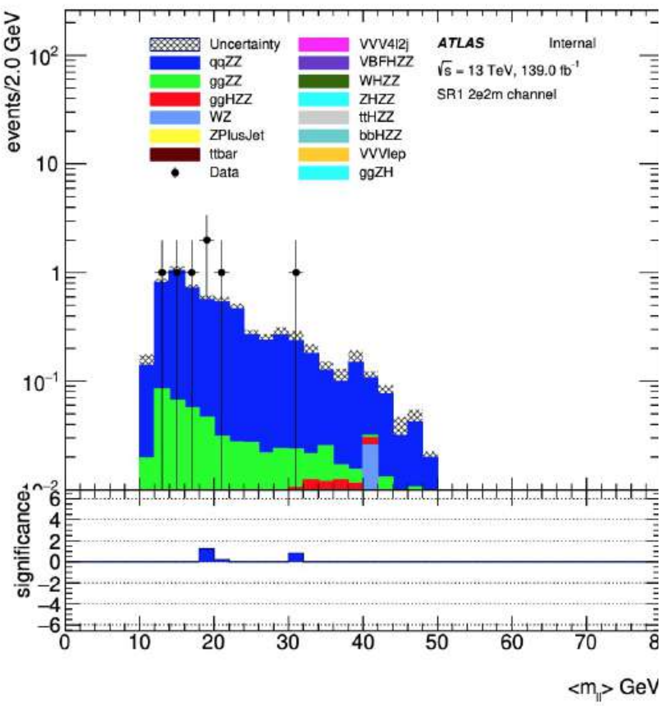

(a)

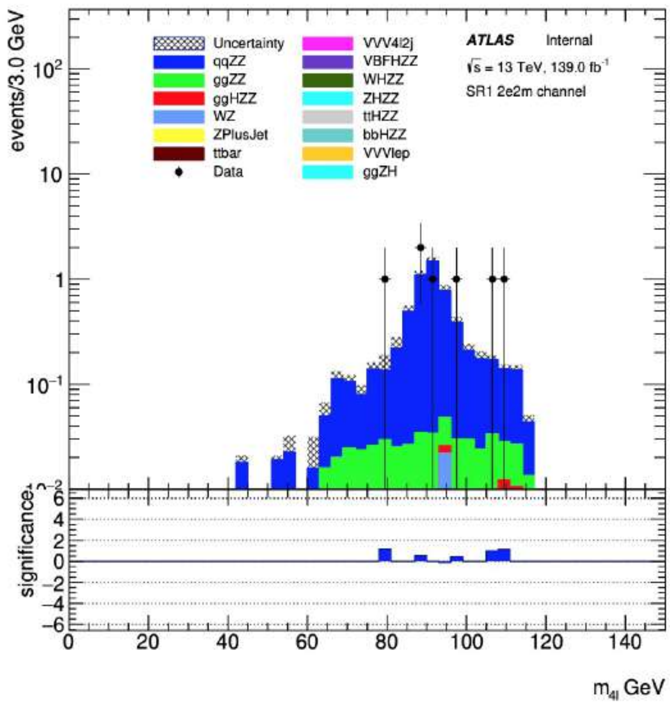

(b)

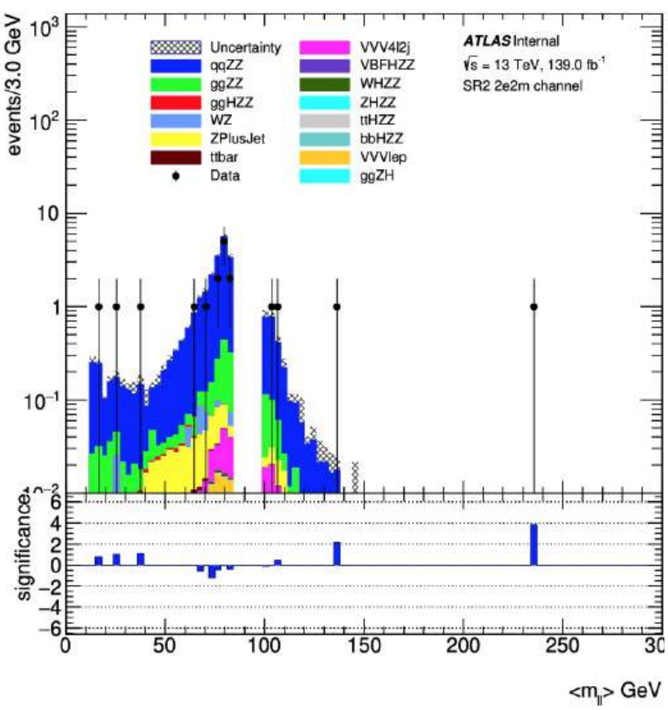

(c)

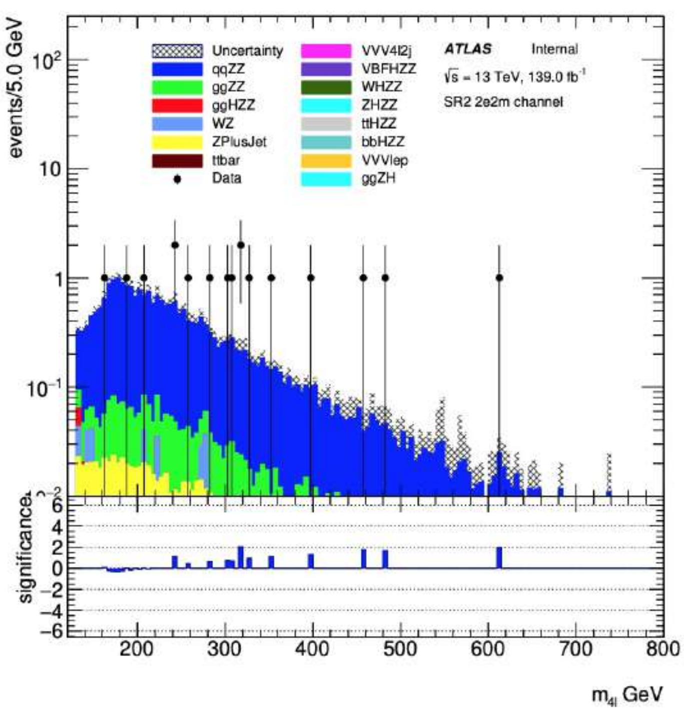

(d)

Figure 6.6: a (c) and b (d) are respectively the distributions of $< m_{ll} >$ and $m_{4\ell}$ in SR1 (SR2) for the $2e2\mu$ channel using the full MC campaigns merged.

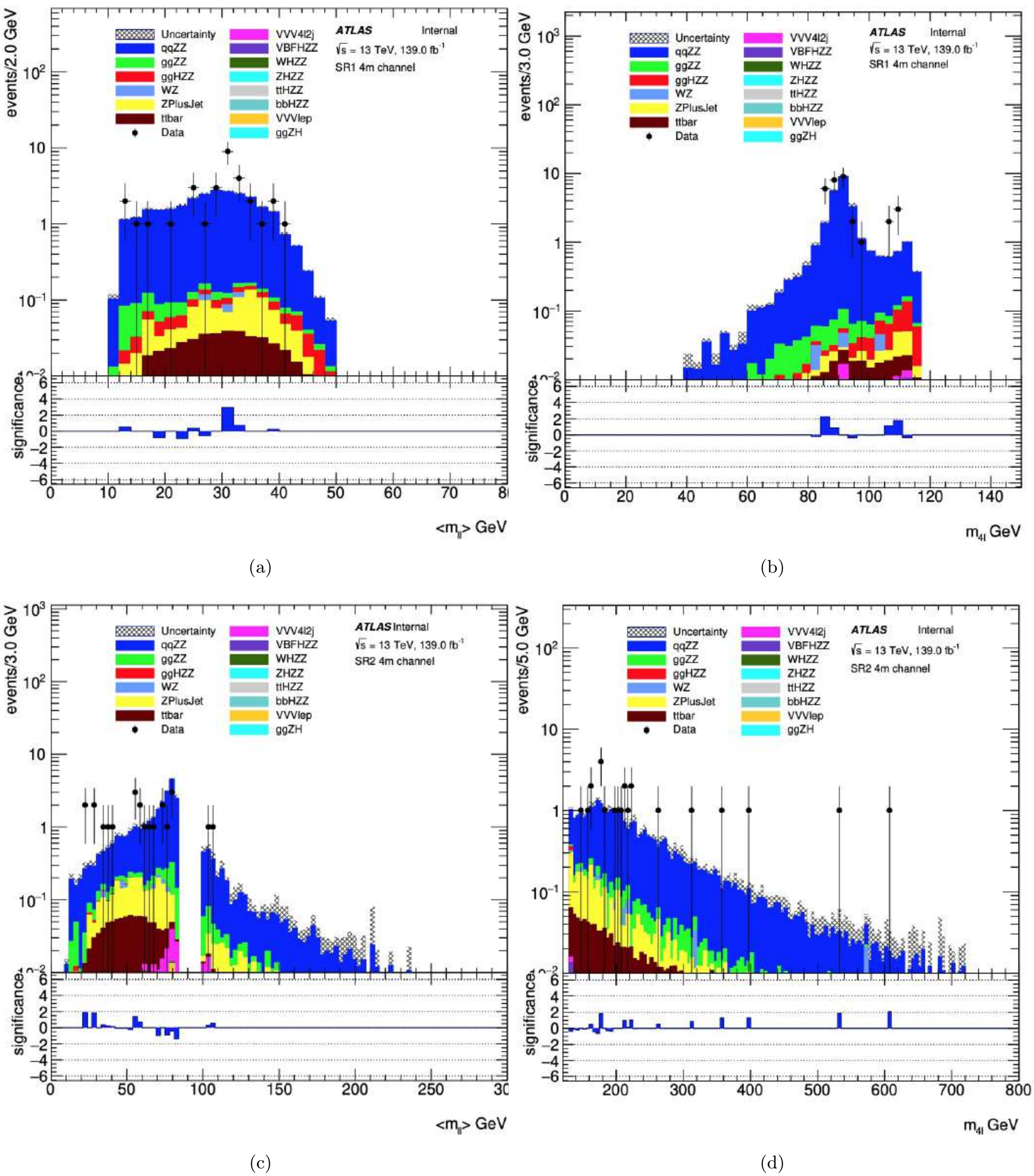

Figure 6.7: a (c) and b (d) are respectively the distributions of $< m_{ll} >$ and $m_{4\ell}$ in SR1 (SR2) for the 4μ channel using the full MC campaigns merged.

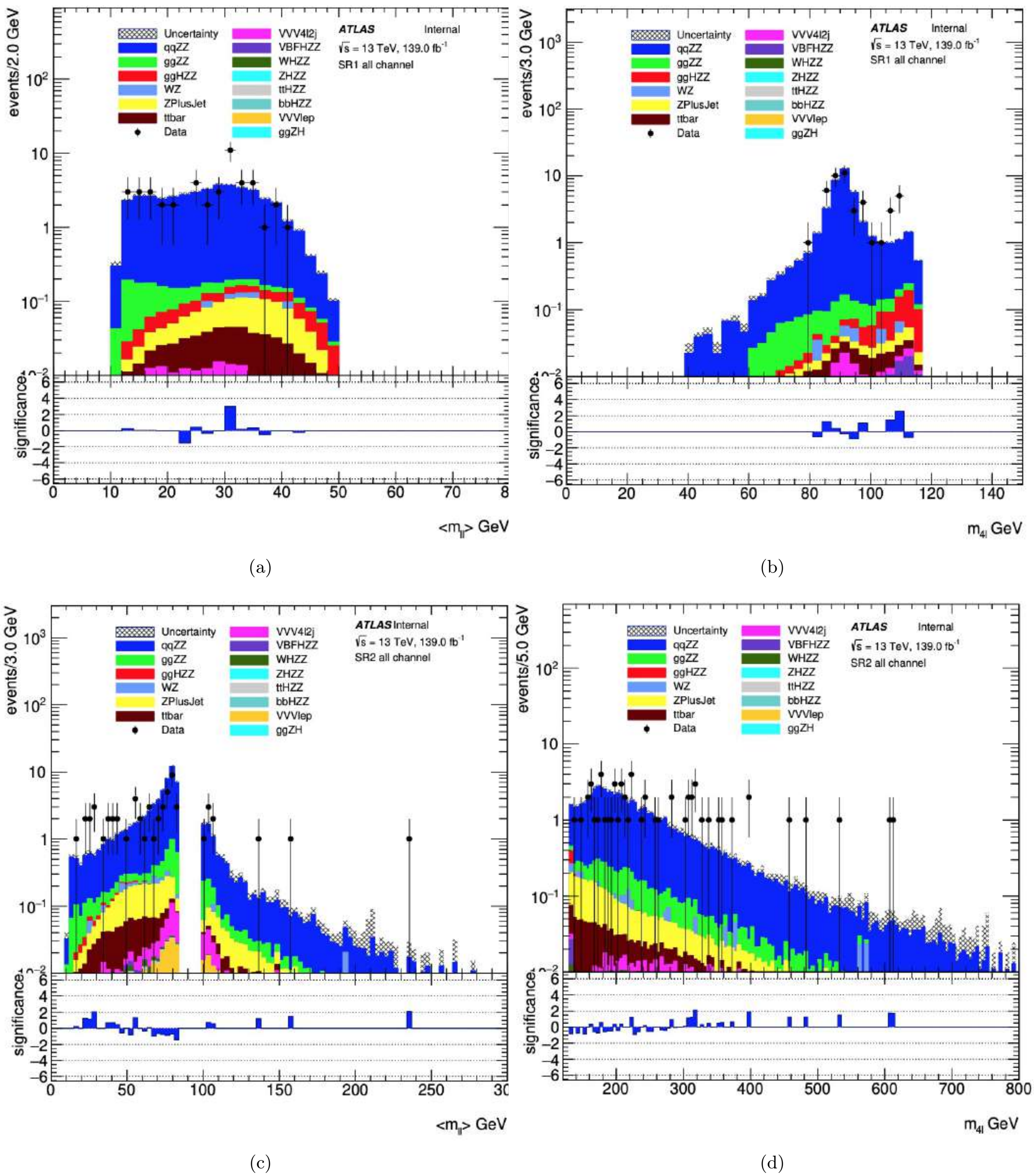

(a) (b)

(c) (d)

Figure 6.8: a (c) and b (d) are respectively the distributions of $< m_{ll} >$ and $m_{4\ell}$ in SR1 (SR2) for all channels combined using the full MC campaigns merged.

Chapter 7

Interpretation

For the interpretation of the analysis results, the maximum likelihood approach was adopted to fit the yields in the signal regions using the modified frequentist formalism CL_S, along with a profiled likelihood ratio statistic test [114, 115]. Generally, expected signal and background probability distributions are established using MC predictions or data-driven techniques as described earlier. Except for the statistical uncertainties, which are restricted using Poisson constraints, all nuisance parameters are constrained with Gaussians. The model is built from the input histograms using the HistFactory [116] model-building program. In all samples, the experimental systematic uncertainties are considered correlated.

7.1 Limits on total cross section

The limits on the total cross section $\sigma_S \mathcal{B}r(S \to Z_d Z_d \to 4\ell)$ are calculated considering both the additional scalar and the Z_d boson masses in a 2D plane (m_S, m_{Z_d}) in both signal regions SR1 and SR2. The limits results at a confidence level of 95% in CL_S upper limits as a function of the Z_d mass in each S mass point ($m_{4\ell}$), are illustrated in Figure 7.1. Figures 7.1a (7.1c) and Figures 7.1b (7.1d) are the limits of the expected and the observed cross section respectively in SR1 (SR2).

7.2 Limits on the dark scalar branching ratio

Results can also be interpreted in terms of branching ratios. Once the limits on the total cross section are determined based on the method explained in Reference [9], $\mathcal{B}r(S \to Z_d Z_d \to 4\ell)$ limits are calculated using model-dependent presumptions on $\mathcal{B}r(Z_d \to 2\ell)$.

The branching ratio calculation is derived from the total cross section formulae as

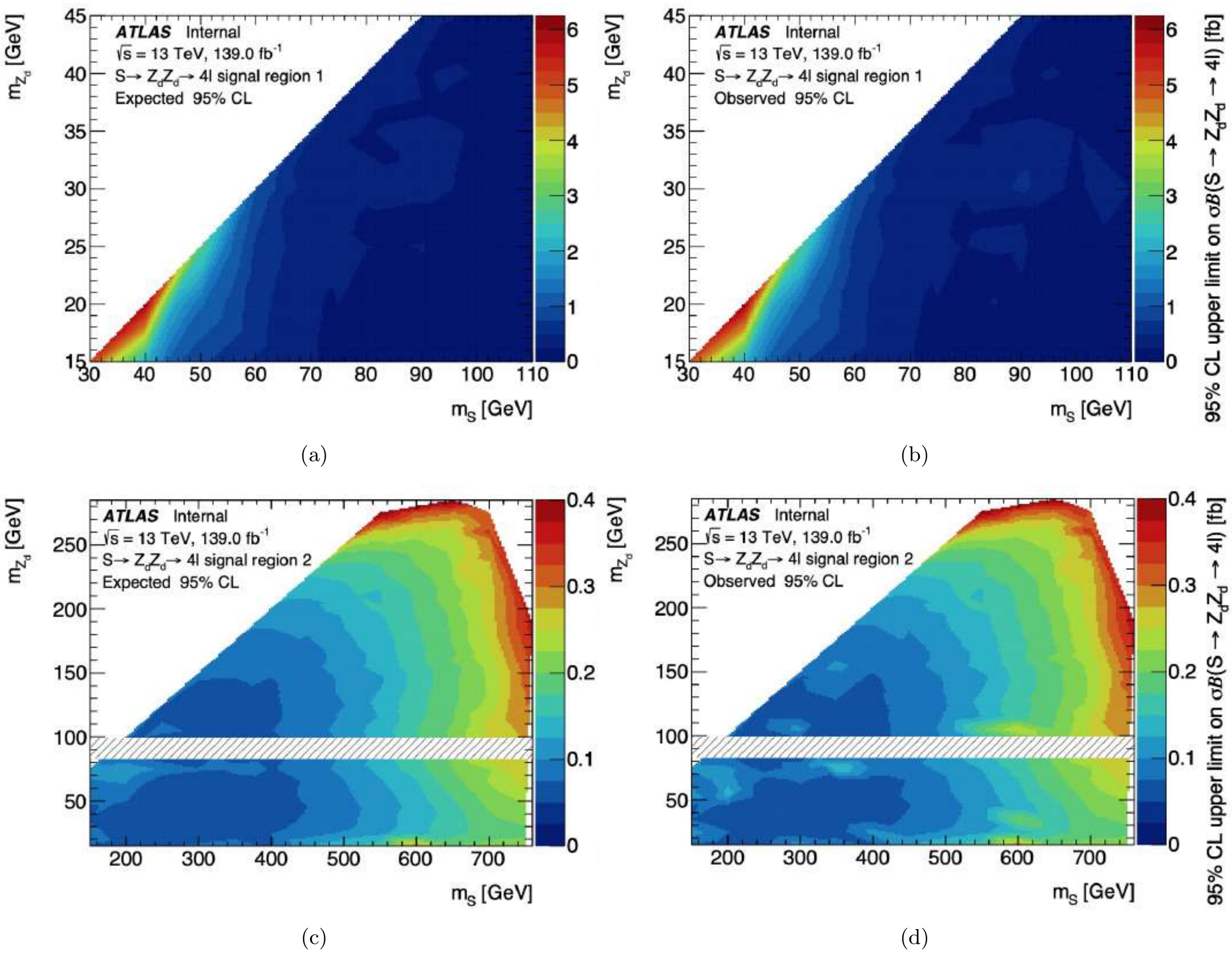

Figure 7.1: Expected a (c) and observed b (d) upper limits at 95% CL on the total cross section × branching ratio $\sigma_S \mathcal{B}r(S \to Z_d Z_d \to 4\ell)$ in SR1 (SR2).

follows:

$$\sigma_{(S\to Z_d Z_d \to 4\ell)} = \frac{N_{signal,SR}}{\mathcal{L}umi} \tag{7.1}$$

$$\mathcal{B}r(S \to Z_d Z_d \to 4\ell) = \frac{\sigma_{(S\to Z_d Z_d \to 4\ell)}}{\sigma_S} \tag{7.2}$$

$$\mathcal{B}r(S \to Z_d Z_d) = \frac{\mathcal{B}r(S \to Z_d Z_d \to 4\ell)}{\Sigma_{allchannels}[\mathcal{B}r(Z_d \to 2\ell)]^2}, \tag{7.3}$$

where $N_{signal,SR}$ is the signal prediction in SR, and σ_S is the BSM dark Higgs cross section taken from [113].

Since in this analysis we are considering $4e$, 4μ, and $2e2\mu$ channels in the final states, the Equation 7.3 becomes:

$$\mathcal{B}r(S \to Z_d Z_d) = \frac{\mathcal{B}r(S \to Z_d Z_d \to 4\ell)}{4[\mathcal{B}r(Z_d \to 2\ell)]^2}, \tag{7.4}$$

where the 4 factor accounts for all final states with considering double counting of $2e2\mu$

since the two Z_d bosons are interchangeable.

As given in Reference [26], the $\mathcal{B}r(Z_d \to 2\ell)$ values in a mass range of $[1, 60]$ GeV are illustrated in Figure 2.10. An extrapolation is performed for higher mass range of Z_d ($[1, 300]$GeV) as shown in Figure 7.2 to cover both SR1 an SR2.
In Figure 7.3, the branching ratios upper limits of $S \to Z_d Z_d$ are shown in SR1 and SR2

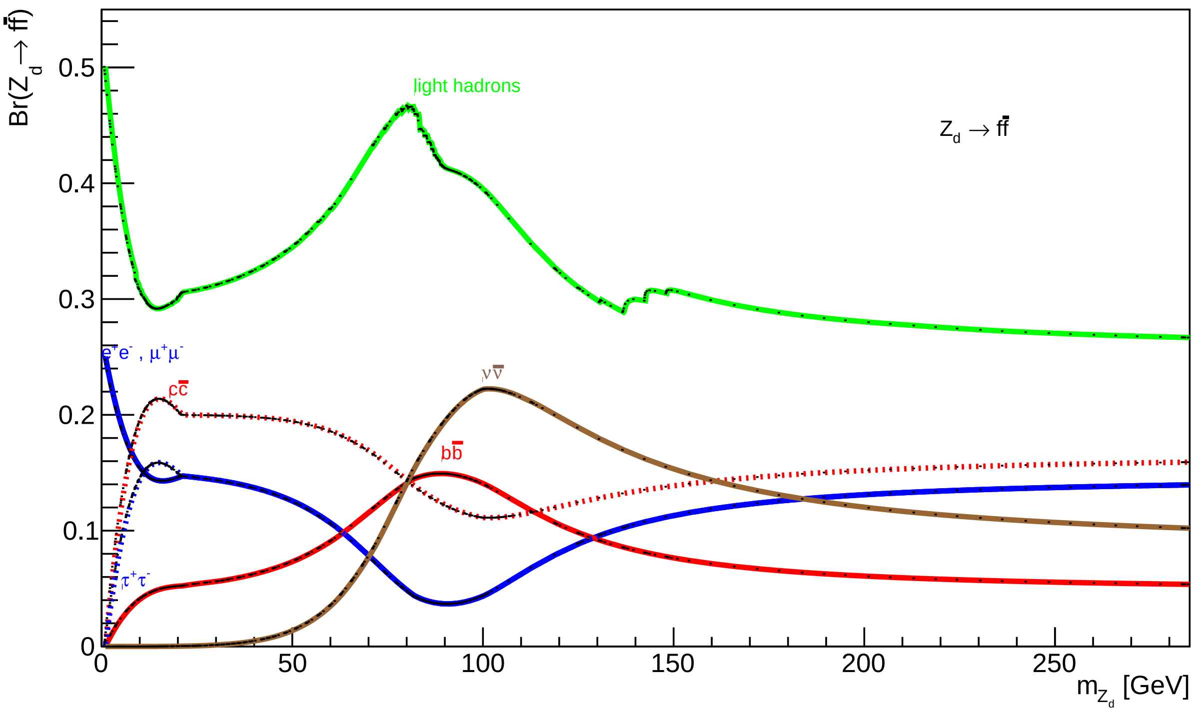

Figure 7.2: Extrapolated $\mathcal{B}r(Z_d \to 2f)$ branching ratio for higher Z_d masses.

at 95% CL.

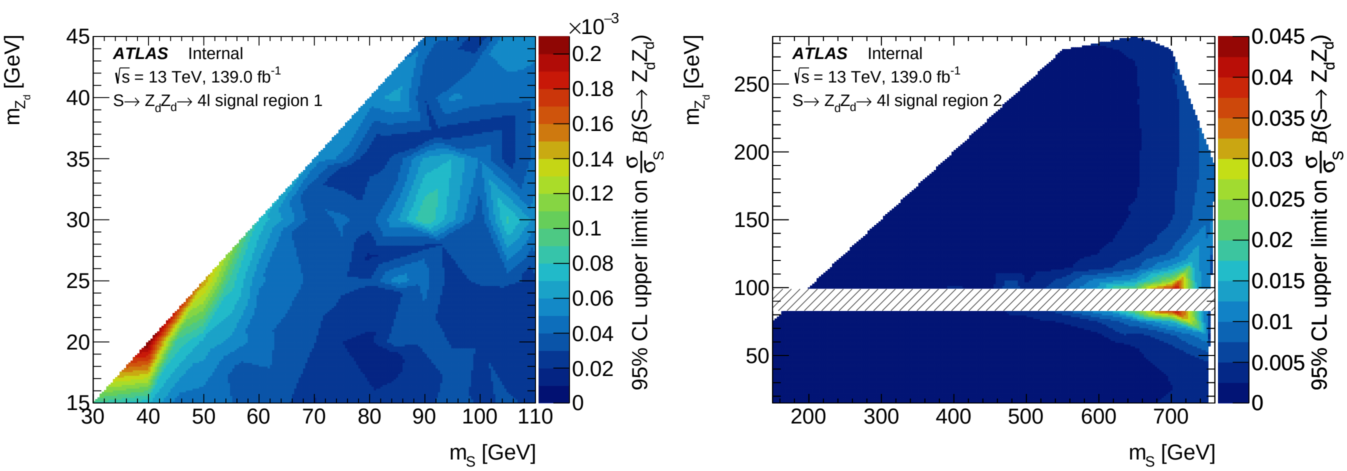

(a) (b)

Figure 7.3: Upper limits at 95% on the model-dependent branching ratio $\mathcal{B}r(S \to Z_d Z_d)$ for SR1 (a) and SR2 (b).

7.3 Local P-value

The local p-values in SR1 and SR2 are computed using the slicing method, where for each panel in $m_{4\ell}$ dimension, a 1D histogram of $< m_{\ell\ell} >$ is constructed to calculate the local p-value using the StandardHypotestInvert tool [117]. Figure 7.4 corresponds to the local p-value in ($m_{4\ell}$,m_{Z_d}) plane in SR1 (7.4a) and SR2 (7.4b).

The smallest p-value, as seen in Figure 7.4a, is observed in the region of ($m_{4\ell}$, m_{Z_d}) =

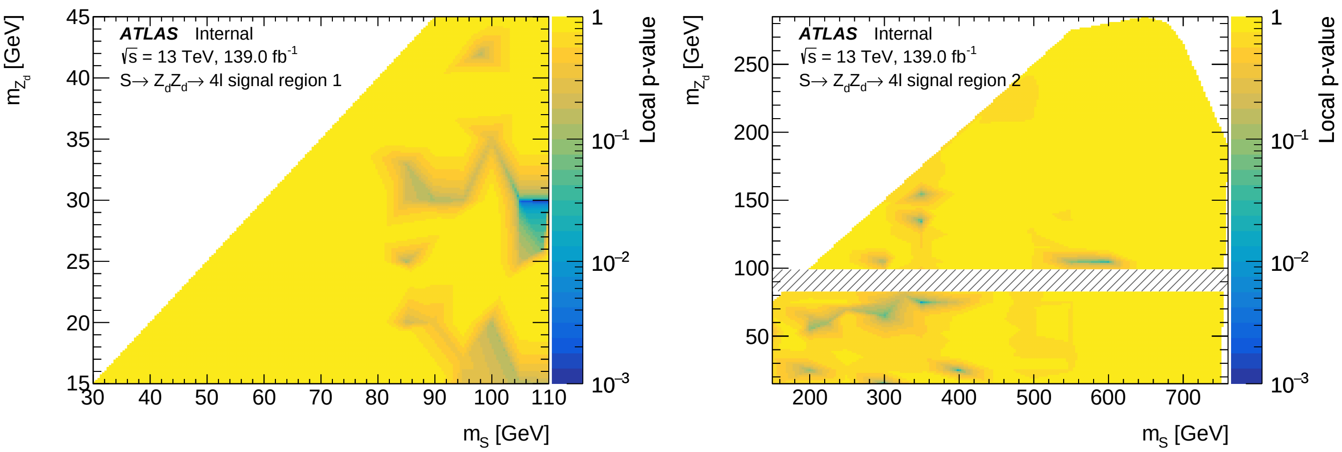

(a) (b)

Figure 7.4: Local p0 in ($m_{4\ell}$, m_{Z_d}) plane for both SR1 (a) and SR2 (b).

(110 GeV, 30 GeV) with a local significance of 3.5σ.

This region is further evaluated using a full 2D scan based on the BumpHunter tool [118, 119], to calculate the bump window, the local p-value, and the global p-value by considering the Look Elsewhere Effect method (LEE) [120]. BumpHunter tool estimates the local and the global p-values using asymptotic and toys, respectively, considering only statistic uncertainties. After feeding the asymptotic-based local p-value to the StandardHypotestInvert tool using toys.

To include the systematic uncertainties, the local and the global p-values are evaluated using the 2D LEE method and converted to their appropriate local and global significances of 4.4σ and 3.4σ, respectively.

Chapter 8

Conclusion

The Standard Model of particle physics has proven highly successful in explaining numerous natural phenomena, yet it falls short in identifying potential candidates for dark matter. In this thesis, the research addresses this gap by exploring a dark sector process within the framework of an extension to the Standard Model, specifically the Hidden Abelian Higgs Model (HAHM), which introduces a $U(1)_d$ gauge group to the $SU(3)_C \otimes SU(2)_L \otimes U(1)_Y$ theory. Utilizing data from the ATLAS detector at the Large Hadron Collider (LHC) collected between 2015 and 2018, corresponding to 139 fb^{-1} of integrated luminosity, the investigation focuses on a Higgs-like dark scalar (S) decaying into two dark matter spin-1 candidates (Z_d), with each Z_d subsequently decaying into a pair of electrons or muons, resulting in four Standard Model (SM) leptons in the final states, denoted as $S \to Z_d Z_d \to 4\ell$.

Chapter 2 delves into the Beyond the Standard Model (BSM) HAHM model considered in this study, while Chapter 3 outlines the LHC and the ATLAS detector as essential components of the experimental apparatus used in the search for Z_d bosons. Chapter 4 contributes to the thesis by presenting a Thermal Performance study of the ATLAS ITk Strip Modules conducted at BNL. This study evaluates the reliability of the ITk staves at low temperatures and monitors humidity to anticipate radiation damage caused by the LHC's upgrade to higher luminosity. Results from the thermal cycling experiment affirm the resilience of the examined ITk stave, demonstrating its ability to withstand temperatures ranging from 23°C to -45°C without significant damage or performance degradation.

Chapter 5 meticulously details the identification and reconstruction of Physics objects, shedding light on the strategic approach employed for identifying leptons compatible with Z_d decay. The analysis of backgrounds in this chapter relies on Monte Carlo (MC) simulations for entities sharing the same signature as the dark sector process, complemented by data-driven methods addressing backgrounds involving jets misidentified or mis-reconstructed as leptons.

In Chapter 6, we delve into a comprehensive elucidation of two methods meticulously employed to enhance the assessment of backgrounds. This chapter further presents the careful selection of analysis objects. Subsequently, Chapter 7 unveils the presentation and interpretation of results in Section 6.5. This interpretive process involves establishing 95% Confidence Level (CL) upper limits on both the total cross section and the $S \to Z_d Z_d$ branching ratio, employing a model-dependent analysis framework. Additionally, we evaluate local and global p-values, revealing a noteworthy peak around $(m_S\ , m_{Z_d}) = (110$ GeV, 30 GeV) with a global (local) significance of 3.4σ (4.4σ). These findings significantly contribute to the broader understanding of particle physics and provide crucial insights into the nature of the studied processes.

While providing valuable insights, the interpretation of these results underscores the need for additional data to gain a deeper understanding of the observed excess. This research contributes significantly to the ongoing exploration of particle physics beyond the Standard Model, addressing both the dark matter mystery and the practical challenges posed by the LHC's upgrade.

References

1. ATLAS Collaboration. Search for short- and long-lived axion-like particles in $H \to aa \to 4\gamma$ decays with the ATLAS experiment at the LHC. arXiv: 2312.03306 [hep-ex] (Dec. 2023) (Cited on page viii).
2. ATLAS Collaboration. Measurement of ZZ production cross-sections in the four-lepton final state in pp collisions at $\sqrt{s} = 13.6$ TeV with the ATLAS experiment. arXiv: 2311.09715 [hep-ex] (Nov. 2023) (Cited on page viii).
3. ATLAS Collaboration. Measurement of the Higgs boson mass in the H→ZZ*→4ℓ decay channel using 139 fb1 of $\sqrt{s}$=13 TeV pp collisions recorded by the ATLAS detector at the LHC. *Physics Letters B* **843,** 137880. ISSN: 0370-2693. https://www.sciencedirect.com/science/article/pii/S0370269323002149 (2023) (Cited on page viii).
4. ATLAS Collaboration. Combination and summary of ATLAS dark matter searches interpreted in a 2HDM with a pseudo-scalar mediator using 139 fb^{-1} of $\sqrt{s} = 13$ TeV pp collision data. arXiv: 2306.00641 [hep-ex] (June 2023) (Cited on page viii).
5. ATLAS Collaboration. Search for Higgs bosons decaying into new spin-0 or spin-1 particles in four-lepton final states with the ATLAS detector with 139 fb1 of pp collision data at $$ \sqrt{s} $$= 13 TeV. *Journal of High Energy Physics* **2022.** https://doi.org/10.1007/JHEP03(2022)041, 41. ISSN: 1029-8479 (Mar. 2022) (Cited on page viii).
6. Soumaimi, Zainab and Boye, Diallo and Fassi, Farida and Assamagan, Ketevi and Connell, Simon and Weber, Christian. Search for Higgs boson Decays to Beyond-the-Standard-Model Light Bosons in Four-Lepton Final States with the ATLAS Detector at the LHC. https://cds.cern.ch/record/2819902 (Apr. 2021) (Cited on page viii).
7. ATLAS Collaboration. Search for new phenomena in events with an energetic jet and missing transverse momentum in pp collisions at $\sqrt{s} = 13$ TeV with the ATLAS detector. *Physical Review D* **103.** http://dx.doi.org/10.1103/PhysRevD.103.112006. ISSN: 2470-0029 (June 2021) (Cited on page viii).
8. ATLAS Collaboration. Search for Higgs boson decays to beyond-the-Standard-Model light bosons in four-lepton events with the ATLAS detector at $$ \sqrt{s}=13 $$ TeV. *Journal of High Energy Physics* **2018.** https://arxiv.org/pdf/1802.03388.pdf (2018) (Cited on page 2).
9. ATLAS Collaboration. Search for Higgs bosons decaying into new spin-0 or spin-1 particles in four-lepton final states with the ATLAS detector with 139 fb^{-1} of pp collision data at $\sqrt{s} = 13$ TeV. *JHEP* **2203.** https://cds.cern.ch/record/2788693/files/2110.13673.pdf, 041. 65 p. arXiv: 2110.13673 (2021) (Cited on pages 2, 20, 24, 95).
10. Gubbels, C. *Searches for Higgs pair production in the 4 b-jet final state with the ATLAS Detector at the LHC* https://cds.cern.ch/record/2815629 (2022) (Cited on page 8).
11. ATLAS Collaboration. Observation of a new particle in the search for the Standard Model Higgs boson with the ATLAS detector at the LHC. *Physics Letters B* **716.** https://arxiv.org/pdf/1207.7214.pdf, 1–29 (2012) (Cited on page 10).
12. Collaboration, C. Observation of a new boson at a mass of 125 GeV with the CMS experiment at the LHC. *Physics Letters B* **716.** https://arxiv.org/pdf/1207.7235.pdf, 30–61 (2012) (Cited on page 10).
13. Collaboration, U. Intermediate-Vector-Boson Properties at the CERN Super Proton Synchrotron Collider. *Europhysics Letters (EPL)* **1.** https://cds.cern.ch/record/179775/files/198511409.pdf, 327–345 (1986) (Cited on page 10).
14. Collaboration, U. An improved determination of the ratio of W and Z masses at the CERN pp collider. *Physics Letters B* **276.** https://www.sciencedirect.com/science/article/pii/037026939290332X, 354–364. ISSN: 0370-2693 (1992) (Cited on page 10).

15. ATLAS Collaboration. Measurement of the W-boson mass in pp collisions at $\sqrt{s} = 7$ TeV with the ATLAS detector. Measurement of the W-boson mass in pp collisions at $\sqrt{s} = 7$ TeV with the ATLAS detector. *Eur. Phys. J. C* **78.** https://cds.cern.ch/record/2242923, 110. 86 p. arXiv: 1701.07240 (2018) (Cited on page 10).
16. *Standard Model Summary Plots February 2022* tech. rep. https://cds.cern.ch/record/2804061 (CERN, Geneva, 2022) (Cited on page 11).
17. Bertone, G., Hooper, D. & Silk, J. Particle dark matter: evidence, candidates and constraints. *Physics Reports* **405,** 279–390. https://doi.org/10.1016%2Fj.physrep.2004.08.031 (2005) (Cited on page 12).
18. *FGST: Fermi Gamma-ray Space Telescope. Stanford.* https://fgst.slac.stanford.edu (Cited on page 12).
19. *The LZ Dark Matter Experiment.* https://lz.lbl.gov/detector/ (Cited on page 12).
20. Bertone, G. & Tait, T. M. P. A new era in the search for dark matter. *Nature* **562.** https://doi.org/10.1038/s41586-018-0542-z, 51–56 (2018) (Cited on page 14).
21. Martin, S. P. A Supersymmetry primer. *Adv. Ser. Direct. High Energy Phys.* **18** (ed Kane, G. L.) https://arxiv.org/pdf/hep-ph/9709356.pdf, 1–98. arXiv: hep-ph/9709356 (1998) (Cited on page 15).
22. Hooper, D. & Profumo, S. Dark matter and collider phenomenology of universal extra dimensions. *Physics Reports* **453.** https://arxiv.org/pdf/hep-ph/0701197.pdf, 29–115 (2007) (Cited on page 15).
23. Schmaltz, M. & Tucker-Smith, D. LITTLE HIGGS THEORIES. *Annual Review of Nuclear and Particle Science* **55.** https://arxiv.org/pdf/hep-ph/0502182.pdf, 229–270 (2005) (Cited on page 15).
24. Kolb, E. *The early universe* (CRC press, 2018) (Cited on page 15).
25. Boyarsky, A., Drewes, M., Lasserre, T., Mertens, S. & Ruchayskiy, O. Sterile neutrino Dark Matter. *Progress in Particle and Nuclear Physics* **104.** https://arxiv.org/pdf/1807.07938.pdf, 1–45 (2019) (Cited on page 15).
26. Curtin, D. *et al.* Exotic decays of the 125 GeV Higgs boson. *Physical Review D* **90.** https://arxiv.org/pdf/1312.4992.pdf (2014) (Cited on pages 16, 17, 19, 21–23, 97).
27. Davoudiasl, H., Lee, H.-S. & Marciano, W. J. "Dark" Z implications for parity violation, rare meson decays, and Higgs physics. *Phys. Rev. D* **85.** https://journals.aps.org/prd/pdf/10.1103/PhysRevD.85.115019, 115019 (11 2012) (Cited on page 16).
28. Curtin, D., Essig, R., Gori, S. & Shelton, J. Illuminating dark photons with high-energy colliders. *Journal of High Energy Physics* **2015.** https://arxiv.org/pdf/1412.0018.pdf (2015) (Cited on page 18).
29. Gunion, J. F., Grzadkowski, B., Haber, H. E. & Kalinowski, J. Limits from LEP Data oniCP/i-Violating Nonminimal Higgs Sectors. *Physical Review Letters* **79.** https://arxiv.org/pdf/hep-ph/9704410.pdf, 982–985 (1997) (Cited on page 21).
30. Bé langer, G., Dumont, B., Ellwanger, U., Gunion, J. F. & Kraml, S. Global fit to Higgs signal strengths and couplings and implications for extended Higgs sectors. *Physical Review D* **88.** https://arxiv.org/pdf/1306.2941.pdf (2013) (Cited on page 21).
31. Vanden Broeck, R. *THE CERN ACCELERATOR COMPLEX.* https://cds.cern.ch/record/2693837. 2019 (Cited on page 27).
32. Collaboration, T. A. *Public luminosity results.* https://twiki.cern.ch/twiki/bin/view/AtlasPublic/LuminosityPublicResultsRun2 (Cited on pages 29, 30).
33. ATLAS Collaboration. The ATLAS Experiment at the CERN Large Hadron Collider. *JINST* **3.** https://cds.cern.ch/record/1129811, S08003. 437 p (2008) (Cited on pages 31, 34–36).
34. ATLAS Collaboration. The ATLAS Inner Detector Trigger performance in *pp* collisions at 13 TeV during LHC Run 2. *Eur. Phys. J. C* **82.** https://cds.cern.ch/record/2774961", 206. 79 p. arXiv: 2107.02485 (2021) (Cited on page 32).
35. Fabjan, C. W. & Gianotti, F. Calorimetry for Particle Physics. *Rev. Mod. Phys.* **75.** https://cds.cern.ch/record/692252/files/ep-2003-075.pdf, 1243–1286 (2003) (Cited on page 33).
36. Barillari, T. The ATLAS liquid argon hadronic end-cap calorimeter: construction and selected beam test results. *Nuclear Physics B - Proceedings Supplements* **150.** https://arxiv.org/pdf/physics/0407026.pdf, 102–105 (2006) (Cited on page 34).
37. Archambault, J. P. *et al.* Performance of the ATLAS liquid argon forward calorimeter in beam tests. *JINST* **8.** https://cds.cern.ch/record/1984169, P05006 (2013) (Cited on page 34).
38. Experiment, A. *ATLAS Fact Sheets* in. https://atlas.cern/Resources/Fact-sheets (2021) (Cited on page 36).
39. Rodriguez Vera, A. M. & Antunes Pequenao, J. *ATLAS Detector Magnet System* https://cds.cern.ch/record/2770604. 2021 (Cited on page 37).

40. *The HL-LHC project.* https://hilumilhc.web.cern.ch/content/hl-lhc-project (Cited on page 39).

41. David, C. *A new strips tracker for the upgraded ATLAS ITk detector* tech. rep. 01. https://cds.cern.ch/record/2286469/files/ATL-UPGRADE-PROC-2017-001.pdf (CERN, Geneva, 2018) (Cited on page 42).

42. *Technical Design Report for the ATLAS Inner Tracker Strip Detector* tech. rep. https://cds.cern.ch/record/2257755/files/ATLAS-TDR-025.pdf (CERN, Geneva, 2017) (Cited on pages 39, 41, 42).

43. *USBTC08 Logger* https://www.picotech.com/data-logger/tc-08/thermocouple-data-logger (Cited on page 44).

44. *SHT85 sensor* https://sensirion.com/products/catalog/SHT85/ (Cited on page 44).

45. *Raspberry Pi4* https://www.raspberrypi.com/products/raspberry-pi-4-model-b/ (Cited on page 44).

46. *Influx DataBase* https://grafana.com/docs/grafana/latest/datasources/influxdb/ (Cited on page 47).

47. *Grafana open-source software* https://grafana.com/ (Cited on page 47).

48. *SparkFun Qwiic Mux Breakout - 8 Channel* https://www.sparkfun.com/products/16784 (Cited on page 48).

49. ATLAS Collaboration. The ATLAS Simulation Infrastructure. *The European Physical Journal C* **70.** https://arxiv.org/pdf/1005.4568.pdf, 823–874 (2010) (Cited on page 49).

50. Gleisberg, T. *et al.* Event generation with SHERPA 1.1. *Journal of High Energy Physics* **2009.** https://iopscience.iop.org/article/10.1088/1126-6708/2009/02/007/pdf, 007 (2009) (Cited on page 50).

51. Andersson, B., Gustafson, G., Ingelman, G. & Sjöstrand, T. Parton fragmentation and string dynamics. *Physics Reports* **97.** https://www.sciencedirect.com/science/article/pii/0370157383900807, 31–145. ISSN: 0370-1573 (1983) (Cited on page 51).

52. Amati, D. & Veneziano, G. Preconfinement as a property of perturbative QCD. *Physics Letters B* **83.** https://www.sciencedirect.com/science/article/pii/0370269379908967, 87–92. ISSN: 0370-2693 (1979) (Cited on page 51).

53. Sjöstrand, T. *et al.* An introduction to PYTHIA 8.2. *Computer Physics Communications* **191.** https://arxiv.org/abs/1410.3012, 159–177 (2015) (Cited on pages 52, 77).

54. Sjöstrand, T., Mrenna, S. & Skands, P. A brief introduction to PYTHIA 8.1. *Computer Physics Communications* **178.** https://arxiv.org/abs/0710.3820, 852–867 (2008) (Cited on pages 52, 77).

55. Gleisberg, T *et al.* Event generation with SHERPA 1.1. *Journal of High Energy Physics* **2009.** https://arxiv.org/abs/0811.4622, 007–007 (2009) (Cited on pages 52, 77).

56. Cascioli, F., Maierhöfer, P. & Pozzorini, S. Scattering Amplitudes with Open Loops. *Physical Review Letters* **108.** https://arxiv.org/abs/1111.5206 (2012) (Cited on pages 52, 77).

57. Gleisberg, T. & Höche, S. Comix, a new matrix element generator. *Journal of High Energy Physics* **2008.** https://arxiv.org/abs/0808.3674, 039–039 (2008) (Cited on pages 52, 77).

58. Bothmann, E. *et al.* Event generation with Sherpa 2.2. *SciPost Physics* **7.** https://arxiv.org/abs/1905.09127 (2019) (Cited on pages 52, 77).

59. Schumann, S & Krauss, F. A parton shower algorithm based on Catani-Seymour dipole factorisation. *Journal of High Energy Physics* **2008.** https://arxiv.org/abs/0709.1027, 038–038 (2008) (Cited on pages 52, 77).

60. Catani, S., Krauss, F., Webber, B. R. & Kuhn, R. QCD Matrix Elements + Parton Showers. *Journal of High Energy Physics* **2001.** https://iopscience.iop.org/article/10.1088/1126-6708/2001/11/063/pdf, 063 (2002) (Cited on page 52).

61. Frixione, S., Nason, P. & Oleari, C. Matching NLO QCD computations with parton shower simulations: the POWHEG method. *Journal of High Energy Physics* **2007.** https://arxiv.org/abs/0709.2092, 070–070 (2007) (Cited on pages 52, 77).

62. Hamilton, K., Nason, P., Re, E. & Zanderighi, G. NNLOPS simulation of Higgs boson production. *Journal of High Energy Physics* **2013.** https://arxiv.org/abs/1309.0017 (2013) (Cited on pages 52, 77).

63. Hamilton, K., Nason, P. & Zanderighi, G. *Finite quark-mass effects in the NNLOPS POWHEG+MiNLO Higgs generator* https://arxiv.org/abs/1501.04637. 2015 (Cited on pages 52, 77).

64. Alioli, S., Nason, P., Oleari, C. & Re, E. A general framework for implementing NLO calculations in shower Monte Carlo programs: the POWHEG BOX. *Journal of High Energy Physics* **2010.** https://arxiv.org/abs/1002.2581 (2010) (Cited on pages 52, 77).

65. Nason, P. A New Method for Combining NLO QCD with Shower Monte Carlo Algorithms. *Journal of High Energy Physics* **2004.** https://arxiv.org/abs/hep-ph/0409146, 040–040 (2004) (Cited on pages 52, 77).

66. Alwall, J. *et al.* The automated computation of tree-level and next-to-leading order differential cross sections, and their matching to parton shower simulations. *Journal of High Energy Physics* **2014.** https://arxiv.org/abs/1405.0301 (2014) (Cited on pages 52, 77).

67. Wiesemann, M. *et al.* Higgs production in association with bottom quarks. *Journal of High Energy Physics* **2015.** https://arxiv.org/abs/1409.5301 (2015) (Cited on pages 52, 77).

68. Cornelissen, T *et al. Concepts, Design and Implementation of the ATLAS New Tracking (NEWT)* tech. rep. https://cds.cern.ch/record/1020106 (CERN, Geneva, 2007) (Cited on page 53).

69. Lacuesta, V. *Track and Vertex Reconstruction in the ATLAS Experiment* tech. rep. https://cds.cern.ch/record/1482119 (CERN, Geneva, 2012) (Cited on page 53).

70. COllaboration, T. A. Electron and photon performance measurements with the ATLAS detector using the 2015–2017 LHC proton-proton collision data. *Journal of Instrumentation* **14.** https://iopscience.iop.org/article/10.1088/1748-0221/14/12/P12006/pdf, P12006 (2019) (Cited on pages 54, 57).

71. *Electron efficiency measurements with the ATLAS detector using the 2015 LHC proton-proton collision data* tech. rep. https://cds.cern.ch/record/2157687 (CERN, Geneva, 2016) (Cited on page 54).

72. *Reconstruction and Identification of Electrons* tech. rep. https://cds.cern.ch/record/1171939 (CERN, Geneva, 2009) (Cited on page 55).

73. ATLAS Collaboration. Electron reconstruction and identification in the ATLAS experiment using the 2015 and 2016 LHC proton–proton collision data at $$\sqrt{s} = 13$$ $$\text {TeV}$$. *The European Physical Journal C* **79.** https://arxiv.org/pdf/1902.04655.pdf (2019) (Cited on pages 56, 57).

74. Hocker, A. *et al. TMVA - Toolkit for Multivariate Data Analysis with ROOT: Users guide. TMVA - Toolkit for Multivariate Data Analysis* tech. rep. https://cds.cern.ch/record/1019880 (CERN, Geneva, 2007) (Cited on page 56).

75. ATLAS Collaboration. Muon reconstruction and identification efficiency in ATLAS using the full Run 2 *pp* collision data set at $\sqrt{s} = 13$ TeV. *Eur. Phys. J., C* **81.** http://cds.cern.ch/record/2746302, 578. 44 p. arXiv: 2012.00578 (2021) (Cited on page 60).

76. Collaboration, T. A. Topological cell clustering in the ATLAS calorimeters and its performance in LHC Run 1. *The European Physical Journal C* **77.** https://arxiv.org/pdf/1603.02934.pdf (2017) (Cited on page 60).

77. Cacciari, M., Salam, G. P. & Soyez, G. The anti-kt jet clustering algorithm. *Journal of High Energy Physics* **2008.** https://iopscience.iop.org/article/10.1088/1126-6708/2008/04/063/pdf, 063 (2008) (Cited on page 61).

78. *Tagging and suppression of pileup jets with the ATLAS detector* tech. rep. https://cds.cern.ch/record/1700870/files/ATLAS-CONF-2014-018.pdf (CERN, Geneva, 2014) (Cited on page 61).

79. Collaboration, T. A. Performance of pile-up mitigation techniques for jets in *pp* collisions at $\sqrt{s} = 8$ TeV using the ATLAS detector. Performance of pile-up mitigation techniques for jets in *pp* collisions at $\sqrt{s} = 8$ TeV using the ATLAS detector. *Eur. Phys. J. C* **76.** https://cds.cern.ch/record/2058295/files/pileup-jetperf-2014-03.pdf, 581. arXiv: 1510.03823 (2016) (Cited on page 61).

80. *Optimisation and performance studies of the ATLAS b-tagging algorithms for the 2017-18 LHC run* tech. rep. https://cds.cern.ch/record/2273281/files/ATL-PHYS-PUB-2017-013.pdf (CERN, Geneva, 2017) (Cited on page 62).

81. *Secondary vertex finding for jet flavour identification with the ATLAS detector* tech. rep. https://cds.cern.ch/record/2270366/files/ATL-PHYS-PUB-2017-011.pdf (CERN, Geneva, 2017) (Cited on page 62).

82. *Topological b-hadron decay reconstruction and identification of b-jets with the JetFitter package in the ATLAS experiment at the LHC* tech. rep. https://cds.cern.ch/record/2645405/files/ATL-PHYS-PUB-2018-025.pdf (CERN, Geneva, 2018) (Cited on page 62).

83. ATLAS Collaboration. Performance of missing transverse momentum reconstruction with the ATLAS detector using proton–proton collisions at $\sqrt{s} = 13TeV$. *The European Physical Journal C* **78.** http://dx.doi.org/10.1140/epjc/s10052-018-6288-9 (Nov. 2018) (Cited on pages 64–69).

84. ATLAS Collaboration. Electron and photon energy calibration with the ATLAS detector using LHC Run 1 data. Electron and photon energy calibration with the ATLAS detector using LHC Run 1 data. *Eur. Phys. J. C* **C74.** https://cds.cern.ch/record/1744017/files/scoap3-fulltext.pdf, 3071. arXiv: 1407.5063 (2014) (Cited on page 64).

85. *Electron efficiency measurements with the ATLAS detector using the 2015 LHC proton-proton collision data* tech. rep. https://cds.cern.ch/record/2157687/files/ATLAS-CONF-2016-024.pdf (CERN, Geneva, 2016) (Cited on page 64).

86. ATLAS Collaboration. Measurement of the photon identification efficiencies with the ATLAS detector using LHC Run-1 data. *The European Physical Journal C* **76.** https://arxiv.org/pdf/1606.01813.pdf. ISSN: 1434-6052 (Dec. 2016) (Cited on page 64).

87. ATLAS Collaboration. Electron and photon energy calibration with the ATLAS detector using LHC Run 1 data. *The European Physical Journal C* **74.** https://doi.org/10.1140/epjc/s10052-014-3071-4, 3071. ISSN: 1434-6052 (Oct. 2014) (Cited on page 64).

88. ATLAS Collaboration. Identification and energy calibration of hadronically decaying tau leptons with the ATLAS experiment in pp collisions at $\sqrt{s} = 8$ TeV. *The European Physical Journal C* **75.** https://arxiv.org/pdf/1412.7086.pdf. ISSN: 1434-6052 (July 2015) (Cited on page 65).

89. Hyneman, R. *et al. Electron, Muon, and Photon Isolation in 2015-2018* tech. rep. https://cds.cern.ch/record/2672803 (CERN, Geneva, 2019) (Cited on page 73).

90. Lampl, W *et al. Calorimeter Clustering Algorithms: Description and Performance* tech. rep. https://cds.cern.ch/record/1099735 (CERN, Geneva, 2008) (Cited on page 74).

91. Boye, D. *The search for a dark vector boson and a new scalar with the ATLAS detector* https://cds.cern.ch/record/2744021 (2020) (Cited on pages 75, 76).

92. Caola, F., Melnikov, K., Röntsch, R. & Tancredi, L. QCD corrections to ZZ production in gluon fusion at the LHC. *Physical Review D* **92.** https://arxiv.org/abs/1509.06734 (2015) (Cited on page 77).

93. Butterworth, J. *et al.* PDF4LHC recommendations for LHC Run II. *Journal of Physics G: Nuclear and Particle Physics* **43.** https://arxiv.org/abs/1510.03865, 023001 (2016) (Cited on page 77).

94. ATLAS Collaboration. Measurement of the Z/ $*bosontransversemomentumdistributioninppcollisionsats = 7$$\sqrt{s}=7 $$ TeV with the ATLAS detector. *Journal of High Energy Physics* **2014.** https://arxiv.org/abs/1406.3660 (2014) (Cited on page 77).

95. Pumplin, J. *et al.* New Generation of Parton Distributions with Uncertainties from Global QCD Analysis. *Journal of High Energy Physics* **2002.** https://arxiv.org/abs/hep-ph/0201195, 012–012 (2002) (Cited on page 77).

96. Anastasiou, C. *et al. High precision determination of the gluon fusion Higgs boson cross-section at the LHC* https://arxiv.org/abs/1602.00695. 2016 (Cited on page 77).

97. *ATLAS Pythia 8 tunes to 7 TeV data* tech. rep. https://cds.cern.ch/record/1966419 (CERN, Geneva, 2014) (Cited on page 77).

98. Ball, R. D. *et al.* Parton distributions with LHC data. *Nuclear Physics B* **867.** https://arxiv.org/abs/1207.1303, 244–289 (2013) (Cited on page 77).

99. Ball, R. D. *et al.* Parton distributions for the LHC run II. *Journal of High Energy Physics* **2015.** https://arxiv.org/abs/1410.8849 (2015) (Cited on page 77).

100. Anastasiou, C., Dixon, L., Melnikov, K. & Petriello, F. High-precision QCD at hadron colliders: Electroweak gauge boson rapidity distributions at next-to-next-to leading order. *Physical Review D* **69.** https://arxiv.org/abs/hep-ph/0312266 (2004) (Cited on page 77).

101. *Multi-Boson Simulation for 13 TeV ATLAS Analyses* tech. rep. https://cds.cern.ch/record/2119986 (CERN, Geneva, 2016) (Cited on page 77).

102. Frixione, S., Hirschi, V., Pagani, D., Shao, H. S. & Zaro, M. *Electroweak and QCD corrections to top-pair hadroproduction in association with heavy bosons* https://arxiv.org/abs/1504.03446. 2015 (Cited on page 77).

103. Lai, H.-L. *et al.* New parton distributions for collider physics. *Physical Review D* **82.** https://arxiv.org/abs/1007.2241 (2010) (Cited on page 77).

104. ATLAS Collaboration. The ATLAS Simulation Infrastructure. *The European Physical Journal C* **70.** https://arxiv.org/abs/1005.4568, 823–874 (2010) (Cited on page 77).

105. Agostinelli, S. *et al.* Geant4—a simulation toolkit. *Nuclear Instruments and Methods in Physics Research Section A: Accelerators, Spectrometers, Detectors and Associated Equipment* **506.** https://www.sciencedirect.com/science/article/pii/S0168900203013688, 250–303. ISSN: 0168-9002 (2003) (Cited on page 77).

106. ATLAS Collaboration. Electron efficiency measurements with the ATLAS detector using 2012 LHC proton–proton collision data. *The European Physical Journal C* **77.** https://arxiv.org/abs/1612.01456 (2017) (Cited on page 77).

107. ATLAS Collaboration. Muon reconstruction performance of the ATLAS detector in proton–proton collision data at $$\sqrt{s}$$ s =13 TeV. *The European Physical Journal C* **76.** https://arxiv.org/abs/1603.05598 (2016) (Cited on page 77).

108. *Electron and photon energy calibration with the ATLAS detector using data collected in 2015 at* $\sqrt{s} = 13$ TeV tech. rep. https://cds.cern.ch/record/2203514 (CERN, Geneva, 2016) (Cited on page 77).

109. Contino, R., Ghezzi, M., Grojean, C., Mühlleitner, M. & Spira, M. eHDECAY: An implementation of the Higgs effective Lagrangian into HDECAY. *Computer Physics Communications* **185.** https://www.sciencedirect.com/science/article/pii/S0010465514002896, 3412–3423. ISSN: 0010-4655 (2014) (Cited on page 78).

110. *Systematic Correction tools* https://gitlab.cern.ch/atlas/athena/-/tree/master/PhysicsAnalysis/Algorithms (Cited on pages 85, 86).

111. *Luminosity For Physics* https://twiki.cern.ch/twiki/bin/viewauth/Atlas/LuminosityForPhysics (Cited on page 86).

112. *Measurement of Differential Cross Sections for Single Diffractive Dissociation in* $\sqrt{s} = 8TeV$ *pp collisions using the ATLAS ALFA Spectrometer* tech. rep. https://cds.cern.ch/record/2670978 (CERN, Geneva, 2019) (Cited on page 86).

113. *BSM Higgs production cross sections at 13 TeV (update in CERN Report4 2016)* https://twiki.cern.ch/twiki/bin/view/LHCPhysics/CERNYellowReportPageBSMAt13TeV (Cited on pages 87, 96).

114. Read, A. L. Presentation of search results: The CL(s) technique. *J. Phys. G* **28** (eds Whalley, M. R. & Lyons, L.) https://www.ippp.dur.ac.uk/Workshops/02/statistics/proceedings/read.pdf, 2693–2704 (2002) (Cited on page 95).

115. Cowan, G., Cranmer, K., Gross, E. & Vitells, O. Asymptotic formulae for likelihood-based tests of new physics. *The European Physical Journal C* **71.** https://arxiv.org/pdf/1007.1727.pdf (2011) (Cited on page 95).

116. Cranmer, K., Lewis, G., Moneta, L., Shibata, A. & Verkerke, W. *HistFactory: A tool for creating statistical models for use with RooFit and RooStats* tech. rep. https://cds.cern.ch/record/1456844/files/CERN-OPEN-2012-016.pdf (New York U., New York, 2012) (Cited on page 95).

117. *RooStats* https://root.cern/doc/master/group__Roostats.html (Cited on page 98).

118. Choudalakis, G. *On hypothesis testing, trials factor, hypertests and the BumpHunter* https://arxiv.org/pdf/1101.0390.pdf. 2011 (Cited on page 98).

119. *pyBumpHunter* https://github.com/scikit-hep/pyBumpHunter/ (Cited on page 98).

120. Vitells, O. & Gross, E. Estimating the significance of a signal in a multi-dimensional search. *Astroparticle Physics* **35.** https://arxiv.org/pdf/1105.4355.pdf, 230–234 (2011) (Cited on page 98).